Developments in
numerical simulations of
the real-life deep drawing process

Timo Meinders

This research project was sponsored by the Dutch Ministry of Economic Affairs, project number IOP-C.94.707.UT.WB, 'Hierarchisch dieptrekmodel' (Hierarchical deep drawing model). The sponsoring is gratefully acknowledged.

De promotiecommissie:

Voorzitter en secretaris:

Prof.dr.ir. H.J. Grootenboer	Universiteit Twente

Promotor:

Prof.dr.ir. J. Huétink	Universiteit Twente

Leden:

Prof. J.-L. Batoz	Université de Technologie de Compiègne
Dr.ir. W.A.M. Brekelmans	Technische Universiteit Eindhoven
Prof.ir. A.W.J. de Gee	Universiteit Twente
Prof.dr.ir. J. Meijer	Universiteit Twente
Prof.dr. C.R. Traas	Universiteit Twente
Dr.Ir. H. Vegter	Corus Group PLC.

Title: Developments in numerical simulations of the real-life deep drawing process
Subject headings:Finite element method
Mixed elastoplastic / rigid plastic material model
Equivalent drawbead model
Adaptive remeshing

ISBN 90-36514002

Printed by Ponsen & Looijen, Wageningen

DEVELOPMENTS IN NUMERICAL SIMULATIONS OF THE REAL-LIFE DEEP DRAWING PROCESS

PROEFSCHRIFT

ter verkrijging van
de graad van doctor aan de Universiteit Twente,
op gezag van de rector magnificus,
prof.dr. F.A. van Vught,
volgens besluit van het College voor Promoties
in het openbaar te verdedigen
op vrijdag 11 februari 2000 te 15.00 uur.

door

Vincent Timo Meinders

geboren op 10 mei 1973
te Hengelo

Dit proefschrift is goedgekeurd door de promotor:

Prof.dr.ir. J. Huétink

If you’re in a valley, with a troubled mind
I’m a mountain, come on and climb
Because you look so good, to be so down
It won’t take much girl, to turn it all around

Come with me, come with me
The feeling’s free, just come with me
Will get on a cloud babe, and ride it high
Say hello sun, as we sail by

I’ll take you where, you’ve never been before
Once we’re there, you’ll cry for more
If it’s dark in your world, come walk in mine
My love’s a light babe, it’s on all the time

Come with me, come with me
The feeling’s free, just come with me
Will get on a cloud girl, and ride it high
Say hello sun, as we sail by

Come with me, come with me
The feeling’s free, just come with me
Will get on a cloud babe, and ride it high
Say hello sun, as we sail by

‘Come with me’ by Waylon Jennings
from cd: Waylon Jennings - Greatest Hits
written by C. Howard

Summary

The deep drawing process is used to manufacture sheet metal products with sometimes complicated shapes and curvatures. The process starts with the clamping of the outer edge of a blank between the blankholder and the die. The blankholder is loaded by a force to prevent wrinkling and to control the material flow into the die cavity. Then the punch moves downwards, simultaneously transferring the specific shape of the tools to the blank. The final product shape after deep drawing is defined by the tools, the blank and the process parameters. Without extensive knowledge of the influences of all these variables on the deep drawing process, it is hardly possible to design the tools adequately and make a proper choice of blank material, lubricant, blankholder force etc. to manufacture a product with the desired shape and performance. A prime tool to study the influence of these variables on the forming process is the finite element method. For an accurate simulation of a real-life deep drawing process an accurate numerical description of the tools, material behavior, contact behavior and other process variables is necessary. Currently, the accuracy and reliability of numerical simulations of the deep drawing process do not yet satisfy the industrial requirements. The limitations of numerical simulations are still the long computational time required for complex deep drawing parts and the lack of detailed knowledge of material physics such as material behavior and contact behavior. The objective of this work is to decrease the computational time of a finite element simulation while maintaining the robustness and accuracy. This thesis presents the development of a mixed elastoplastic / rigid plastic material model, an equivalent drawbead model and an adaptive remeshing procedure for sheet metal forming.

Two widely used numerical material models in sheet metal forming are the elastoplastic material model and the rigid plastic material model. The advantage of the elastoplastic model is that it gives an accurate description of the material behavior. A disadvantage of the elastoplastic material model is that it can give rise to numerical instabilities due to the transition from elastic to plastic behavior. The advantage of the rigid plastic description is that it is a fast and robust algorithm. On the other hand, disadvantages of this material model are that elastic phenomena such as springback cannot be described and that the model becomes inaccurate in dead metal zones. A mixed elastoplastic / rigid plastic material model is developed here to benefit from the advantages of both the elastoplastic and rigid plastic material model, i.e. accuracy and fast convergence over a large range of plastic strain

increments. The mixed material model consists of two parts. For small strain increments, the mixed material model degenerates to the Euler forward elastoplastic material model. For large strain increments, the mixed material model degenerates to the rigid plastic material model. The performance of the mixed material model is investigated for academic and a realistic problem. The mixed material model shows a good performance in case of the academic problems but did not perform well in the case of the realistic problem.

The quality of a sheet metal stamping part is secured by the material flow into the die cavity. A local control mechanism is provided by drawbeads, which are small protrusions in the blankholder-die region. A drawbead consists of two components, the bead itself and a matching groove. The drawbead creates a restraining force by cyclically bending and unbending the sheet as it traverses the drawbead, causing strain changes in the blank. An equivalent drawbead model is developed which replaces the real drawbead geometry in a deep drawing simulation by a line on the tool surface and incorporates the main drawbead characteristics. The input for the equivalent drawbead model is provided by experiments or by a 2D plane strain drawbead model in which the real drawbead geometry is accurately modeled. Experiments are performed to validate the equivalent drawbead model. The good agreement between the experimental data and the simulation results shows that the equivalent drawbead model is a powerful tool to replace the real drawbead in deep drawing simulations, without significant loss of accuracy.

The numerical simulation of real-life deep drawing processes is potentially very expensive. Hence, it is desired to minimize the computational cost while obtaining the desired accuracy. This objective can be achieved by adaptive remeshing. Adaptive remeshing has two major advantages. First, the computational cost can be reduced and second, a highly distorted mesh can be avoided. The adaptive remeshing procedure can be divided into three phases. First, a remeshing criterion is defined based on an error indicator. Next, a new mesh has to be generated which must satisfy specific requirements. Finally, a procedure for the transfer of state variables and boundary conditions from the old mesh to the new mesh is required. In this thesis, two error indicators are presented, i.e. an error indicator based on a thickness error and an error indicator based on a geometrical error. A refinement strategy based on h-adaptivity is developed for 3-node triangular plate elements. Two data transfer procedures are implemented to map the state variables and boundary conditions onto the new mesh. The performance of the adaptive remeshing procedure is demonstrated on the basis of several deep drawing simulations. The adaptive remeshing procedure can successfully be applied to simulations of the real-life deep drawing process, decreasing the necessary computational time for an accurate simulation significantly. Finally, a preliminary study is carried out for the coupling of a wrinkling prediction model to the adaptive remeshing procedure. The results of this study show that this coupling can be very powerful to accurately describe wrinkling behavior while an excessive increase in computational cost is avoided.

Contents

Summary

1. Introduction 5
  1.1 Sheet metal forming 5
  1.2 Numerical simulation 6
  1.3 Previous work and outline of this thesis 8
  1.4 Future research 9
  1.5 References 10

2. Theoretical background to the finite element method 13
  2.1 Introduction 13
  2.2 Kinematics 14
  2.3 Strain definition 17
  2.4 Stress definition 18
  2.5 Constitutive relations 19
  2.6 Weak equilibrium 22
  2.7 Finite element method 23
    2.7.1 Finite element discretization 24
    2.7.2 Iterative Newton-Raphson procedure 25
      2.7.2.1 Determination of the internal force vector 26
      2.7.2.2 Determination of the stiffness matrix 27
  2.8 References 29

3. Mixed elastoplastic / rigid plastic material model for Hill'48 anisotropic material behavior 31
  3.1 Introduction 31
  3.2 Hill'48 planar anisotropic material model 32
  3.3 Time integration of stress-strain relation 33
  3.4 Stress update algorithm 35
    3.4.1 Example: Euler backward stress update 37
  3.5 Consistent stiffness tensor 37
    3.5.1 Elastoplastic consistent stiffness tensor 37

3.5.1.1 Example: consistent stiffness tensor for Euler backward integration 39
3.5.2 Rigid plastic consistent stiffness tensor 39
3.6 Mixed elastoplastic / rigid plastic material model 40
3.6.1 Determination of reference strain increment κ_{ref} 41
3.6.2 Stress update algorithm 42
3.6.3 Consistent stiffness tensor 43
3.7 Degenerated case: initial condition is elastic 44
3.7.1 Consistent stiffness tensor 45
3.8 Applications 47
3.8.1 One-element test 47
3.8.2 Tensile test 48
3.8.3 Rectangular product 49
3.9 Discussion 53
3.10 References 53

4. Equivalent drawbead model 57
4.1 Introduction 57
4.2 2D plane strain drawbead model 59
4.2.1 Convection schemes 60
4.2.2 Analytical verification 63
4.2.2.1 Simple analytical model 63
4.2.2.2 Stoughton model 64
4.2.3 Experimental verification 66
4.2.4 Preparation of the results for the purpose of the equivalent drawbead model 68
4.3 Equivalent drawbead model 69
4.3.1 Implementation of the lift force 70
4.3.2 Implementation of the drawbead restraining force 70
4.3.3 Implementation of the plastic thickness strain 71
4.3.3.1 Stress estimate 71
4.3.3.2 Penalty constraint method 74
4.3.4 Comparison between the two drawbead strain algorithms 76
4.4 Applications 77
4.4.1 Numerical verification 77
4.4.2 Experimental verification 78
4.4.3 Simulation of a fender 81
4.5 Concluding remarks 84
4.6 References 85

5. Adaptive remeshing 89
5.1 Introduction 89
5.2 Remeshing criterion 90
5.2.1 Error indicator based on thickness error 90
5.2.2 Error indicator based on geometrical error 91
5.3 Mesh generation 92
5.3.1 Refinement strategy 93
5.3.2 Degenerated cases 94
5.4 Data transfer 96
5.5 Applications 97

- 5.5.1 Square product simulation: membrane elements 97
- 5.5.2 Square product simulation: Kirchhoff elements 100
- 5.5.3 Simulation of a fender 102

5.6 Prediction of wrinkling in combination with mesh refinement: a preliminary study 105

5.6 Concluding remarks 108

5.7 References 108

6. Conclusions and recommendations 111

List of symbols 113

List of publications 119

Acknowledgment 121

About the author 123

Samenvatting 125

1. Introduction

1.1 Sheet metal forming

In metal forming, a piece of material is plastically deformed between tools to obtain the desired product. A special class of metal forming concerns the case where the thickness of the piece of material is small compared to the other dimensions, i.e. sheet metal forming. Sheet metal forming is a widely used production process: in 1998, 265 million tons of steel sheet and 9 million tons of aluminum sheet was produced worldwide which was approximately 35% of the total steel and aluminum production [Langerak, 1999a]. Sheet metal forming is characterized by a stress state in which the component normal to the sheet plane is generally much smaller than the stresses in the sheet plane. A commonly used sheet metal forming process is the deep drawing process. The principle of deep drawing is schematically represented in Figure 1-1.

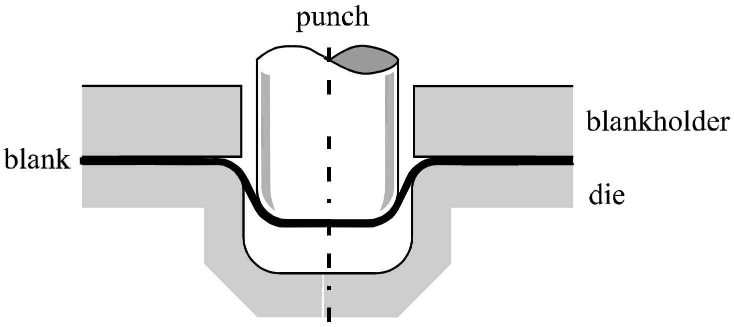

Figure 1-1. Schematic of the deep drawing process

An initially flat or pre-shaped sheet material, the blank, is clamped between the die and the blankholder. The blankholder is loaded by a blankholder force, which is necessary to prevent wrinkling and to control the material flow into the die cavity. Then the punch is pushed into the die cavity, simultaneously transferring the specific shape of the punch and the die to the blank. During the forming stage the material is drawn out of the blankholder-die region, whereas the material is subjected to compressive and tensile stresses during forming. When a very high blankholder force is applied, the deep drawing process becomes a stretching process. In stretch forming the material is fixed under the blankholder, leading to thickness reduction in the remaining part of the blank in which the stresses are tensile in almost all directions. Stretch forming is used mainly to produce large shallow parts that must be subjected to sufficient straining to improve the flex resistance.

As mentioned, the material flow into the die cavity is controlled by the blankholder, a restraining force is created by friction between the tools and the blank. The friction between the tools and the blank is influenced by the blankholder force, lubrication or by coatings on the blank or tools [Haar, 1996], [Carleer, 1997]. However, during the forming stage the blank does not make contact with the entire blankholder. This implies that the material flow can only globally be controlled by the blankholder. A local control mechanism is provided by drawbeads, which are small protrusions in the blankholder-die region. The material is forced to traverse the drawbead when the punch moves into the die cavity, causing a local restraining of the material flow.

The deep drawing process is frequently used in the automotive industry (outer panels, inner panels, stiffeners etc.), the packaging industry (petfood containers, beverage cans etc.) and the household appliances industry (housings etc.) to manufacture products with more complicated shapes and curvatures. Nowadays, the automotive industry tends to favor light construction principles, leading to the usage of light materials (aluminum and sandwich laminates), tailored blanks and the usage of new production processes such as hydroforming [Langerak, 1999b].

A tailored blank consists of several flat sheets that are welded together before forming. A combination of different materials, thickness, and coatings can be welded together to form a blank for stamping car body panels. The main advantage of using tailored blanks is to have specific characteristics at particular parts of the blank in order to reduce weight and costs. Other advantages of using tailored blanks are improvement of shape accuracy, crash durability and reduction in press handling [Meinders, 1999]. There are also disadvantages, however. The welding of the flat sheets is an extra step in the production process with added cost. Moreover, the weld and the Heat Affected Zone can negatively influence the formability of the blank due to the development of martensitic structures [Saunders, 1996].

In the hydroforming process parts are formed using a rigid die and a fluid under high hydrostatic pressure. It is used for the forming of tubular parts and flat sheets. In tube forming a pressure is applied in the interior of the tube and often a mechanical compressive force is exerted in the axial direction. The combination of compressive axial stresses and circumferential tensile stresses facilitates the deformation up to high strains because necking is postponed by the axial compression [Huétink, 1999]. As a result, the hydroforming process offers the ability to manufacture products with very complex shapes which entails a high styling potential for product designers.

1.2 Numerical simulation

The deep drawing process is applied with the intention of manufacturing a product with a desired shape and no failures. The final product shape after deep drawing is defined by the tools, the blank and the process parameters. An incorrect design of the tools and blank shape or an incorrect choice of material and process parameters can yield a product with a deviating shape or with failures. A deviating shape is caused by elastic springback after forming and retracting the tools. The most frequent types of failure are wrinkling, necking (and subsequently tearing), scratching and orange peel. Wrinkling may occur in areas with high compressive strains, necking may occur in areas with high tensile strains, scratching is caused by defects of the tool surface and orange peel may occur after excessive deformations, depending on the grain size of the material. The deformation patterns of the sheet material are influenced by the material properties and the friction conditions. Generally, sheet material behaves anisotropically which means that the material shows a different deformation behavior in different directions because of the rolling process. An example of anisotropy is the development of ‘ears’ in cylindrical cup drawing. The friction conditions during forming depend on the lubricant, the presence of coatings on the blank, surface roughness of the tools and the blank, blankholder pressure and process velocity.

Without extensive knowledge of the influences of all these variables on the deep drawing process, it is hardly possible to design the tools adequately and make a proper choice of blank material and lubricant to manufacture a product with the desired shape and performance. As a result, after the first design of the tools and choice of blank material and lubricant, an extensive and time consuming trial and error process is started to determine the proper tool design and all other variables, leading to the desired product. This trial and error process can yield an unnecessary number of deep drawing strokes, or may even require redesigning the expensive tools. To reduce this waste of time and cost, process modeling for computer simulation can be used to replace the experimental trial and error process by a virtual trial and error process.

The prime objective of an analysis is to assist in the design of a product. To design or select the tools and the equipment, such design essentially consists of:

- predicting the material flow;
- determining whether it is possible to form the part without surface or internal defects;
- predicting the forces and stresses necessary to execute the forming operation.

In the past a number of analyzing methods have been developed and applied to various forming processes. Some of these methods are the slab method, the slip-line field method, the viscoplasticity method, upper and lower bound techniques and Hill's general method. These methods have been useful in qualitatively predicting forming loads, overall geometry changes of the deformed blank and material flow and in determining approximate optimum process conditions. However, a more accurate determination of the effects of various process parameters on the deep drawing process has became possible only recently, when the finite element method was developed for these analyses [Kobayashi, 1989].

Rapid developments in computer hardware make the finite element analysis of complex deformation responses increasingly applicable. The finite element method is used worldwide to simulate the deep drawing process and has become a reliable numerical simulation technology. For an accurate simulation of a real-life deep drawing process an accurate numerical description of the tools is necessary, as well as an accurate description of material behavior, contact behavior and other process variables. The numerical description of the tools is provided by CAD packages which are generally used by tool designers. The description of material behavior, contact behavior and other process variables evolved from rather simple models in the earlier days to more and more sophisticated models nowadays. This evolution is due to the elaborate work of researchers working in the field of metal forming and is shown in authoritative conferences concerning sheet metal forming [Numiform, 1986, 1989, 1992, 1995, 1998], [Numisheet, 1991, 1993, 1996, 1999]. Developments have been made in the field of finite element types, mesh adaptivity, material laws, failure criteria, wrinkling and surface defects, springback, contact algorithms, friction, simulation of new processes (for example hydroforming), optimization and process design.

The conventional finite element codes are based on implicit time integration. This involves repeated solutions of large systems of equations. Furthermore, equilibrium must be fulfilled after each incremental step. As a result, implicit codes are computational time and memory consuming. Hence, a new class of finite element codes based on explicit time integration was developed, resulting in a drastic decrease of computational time. In an explicit code no system of equations needs to be solved and static equilibrium is not checked after each incremental step, as the algorithm assumes an inertia dominated process. The explicit procedure is conditionally stable with a critical time step, which is proportional to the smallest element in the mesh [Mattiasson, 1991]. However, in most sheet metal forming processes inertia effects can be neglected. In order to apply the explicit algorithms in these processes, it is necessary to assume artificially high velocities and accelerations or artificially high mass density, which seems rather unrealistic [Carleer, 1996]. At the present time, the competition between implicit and explicit finite element codes is still in full swing.

Currently, the accuracy and reliability of numerical simulations of sheet metal forming processes do not yet satisfy the industrial requirements. One of the limitations of numerical simulations is still the high computational time for complex deep drawing parts, despite the development of iterative solvers, fast contact algorithms and the ever ongoing progress in computer hardware. Another limitation is the lack of detailed knowledge of material physics such as material behavior at high deformations and contact behavior. Therefore extensive research in the field of sheet metal forming is and will be necessary to decrease the existing gap between the real-life deep drawing process and the predictions obtained from deep drawing simulations.

1.3 Previous work and outline of this thesis

The work as described is this thesis is implemented in the implicit finite element code DiekA. The finite element code DiekA, developed at the University of Twente, is a multi-purpose package which is able to simulate various forming processes such as rolling, deep drawing, extrusion, cutting and slitting. The deep drawing part of this code was developed in close cooperation with Hoogovens Research and Development, a part of the Corus Group PLC since October 6, 1999. The development of the deep drawing part of DiekA was started in 1987. In 1992, Vreede presented deep drawing simulation results of axi-symmetric products, rectangular products and a simple automotive product, making use of a 3-node triangular element based on membrane theory (i.e. only incorporating stretching energy) [Vreede, 1992]. The material behavior was described by rigid plastic constitutive relations and the planar isotropic Hill yield criterion. The contact behavior was described by special contact elements and Coulomb friction. Finally, the tools were numerically described by a collection of measurement points or by elements. Figure 1-2 shows an exploded view of the deep drawing process, where the tools are modeled with elements. In 1992, the work of Vreede was continued by Carleer. The new developments were focused on improving the existing code in order to better satisfy the requirements for industrial application. In the subsequent five years, the following improvements were implemented [Carleer, 1997]: two new 3-node triangular element types, i.e. an element based on Kirchhoff theory (incorporates membrane and bending stresses) and an element based on Mindlin theory (incorporates membrane, bending and shear stresses). The anisotropic behavior of the material was taken into account by implementing the anisotropic Hill'48 yield criterion and the Vegter yield criterion based on multiaxial stress states [Vegter, 1999]. An elastoplastic constitutive relation was implemented in order to predict the springback behavior after deep drawing. The contact description was improved by a fast contact search algorithm and a more sophisticated friction model. Finally, an equivalent drawbead model was developed to efficiently incorporate drawbeads in a finite element simulation.

This thesis presents the research concerning deep drawing simulations of the last four years. The objective of the present research was to improve the robustness and accuracy and to decrease the computation time of real-life finite element simulations. In Chapter 3 a mixed elastoplastic / rigid plastic material model is presented. The objective of this model is that it takes advantage of both the elastoplastic and rigid plastic material models, i.e. accuracy and fast convergence over a large range of plastic strain increments. Chapter 4 presents a sophisticated equivalent drawbead model which incorporates not only the drawbead restraining force but also the effects of sheet thinning and strain changes. This equivalent drawbead model replaces the real drawbead geometry in a deep drawing simulation to avoid a drastic increase in computation time without significant loss of accuracy. Finally, an adaptive remeshing procedure is presented in Chapter 5. The objective of adaptive remeshing is to reduce the computational costs (computation time, data storage and time to prepare the initial mesh) while still retaining the desired accuracy.

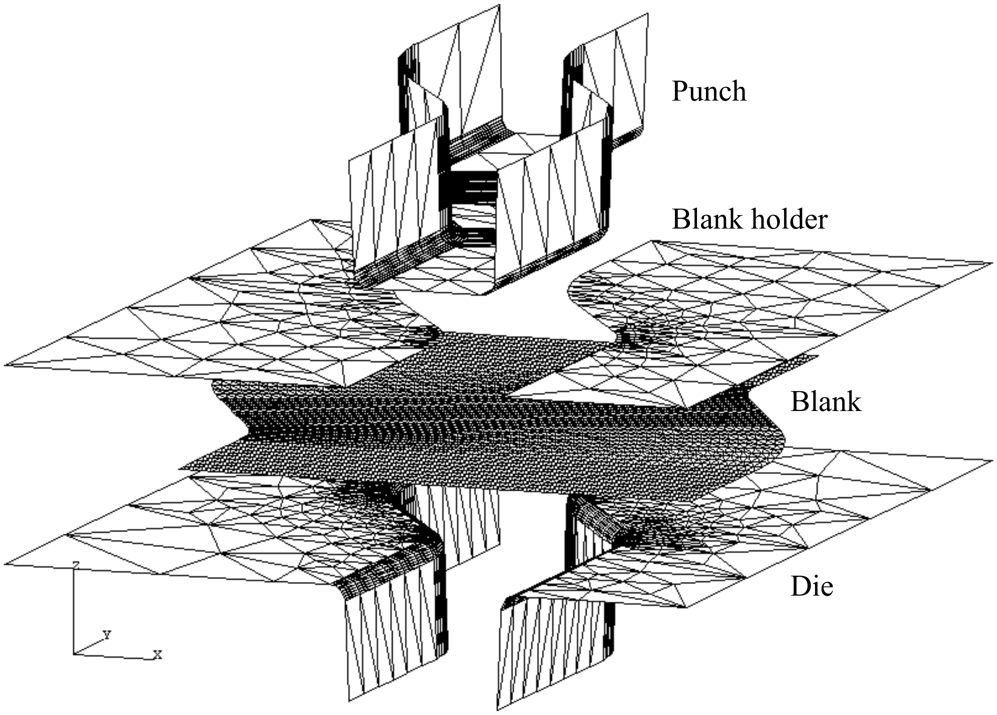

Figure 1-2. Exploded view of the deep drawing simulation of an S-rail [Numisheet, 1996]

1.4 Future research

During the last decades, several commercial and research finite element codes have been developed that are more or less able to simulate real-life deep drawing processes. Most of these codes incorporate sophisticated descriptions of material behavior, fast solvers, element types and mesh adaptivity. Recently, they tend to cater also for simulations of new production processes such as hydroforming. However, the improvements in the description of contact behavior are inferior to the former mentioned points of interest. Since contact should be of major concern in simulations, as contact between the blank and the tools is the driving force in the deep drawing process, this inferiority is unsatisfactory. A second topic that is inferior to the previously mentioned points of interest is the accurate simulation of the whole manufacturing process, comprising deep drawing, trimming, flanging and hemming operations. The final product shape is influenced by all these operations due to springback after each operation. Therefore it is essential for an accurate prediction of the final product shape to accurately describe springback behavior after each operation and take these effects into account in the successive operations. Numerically this means that an accurate coupling must be developed between the simulations of different operations. This is not as obvious as it sounds, since generally deep drawing simulations are performed 3-dimensionally and hemming, trimming and flanging operations are modeled in 2 dimensions. Concluding, the author recommends an increasing research effort concerning these two inferior topics, since a chain is only as strong as its weakest link and it seems that contact behavior and full process modeling are becoming the weaker links.

1.5 References

[Carleer, 1996]
Carleer B.D., J. Huétink, 'Closing the gap between the workshop and numerical simulation in sheet metal forming', Computational Methods in Applied Sciences: Eccomas '96, J.-A. Désidéri et al. (eds.), p. 554-560, 1996

[Carleer, 1997]
Carleer, B.D. 'Finite element analysis of deep drawing', Ph.D. Thesis, University of Twente, Enschede, ISBN 90-90103589, 1997

[Haar, 1996]
Haar R. ter, 'Friction in sheet metal forming: the influence of (local) contact conditions and deformation', Ph.D. Thesis, University of Twente, Enschede, ISBN 90-9009296X, 1996

[Huétink, 1999]
Huétink J., D.G. Roddeman, H.J.M. Geijselaers, A.H. van den Boogaard, 'Mechanics of forming processes', Report WB.99/TM-4049, University of Twente, Enschede, 1999

[Kobayashi, 1989]
Kobayashi S., S.I. Oh, T. Altan, 'Metal forming and the finite element method', Oxford University Press, New York, 1989

[Langerak, 1999a]
Langerak N.A.J., Private communication, 1999

[Langerak, 1999b]
Langerak N.A.J., S.P. Kragtwijk, 'The use of finite element models in the development of a lightweight steel and aluminium car body', Proceedings of the 2nd Esaform Conference on Material Forming, J.A. Covas (ed.), Guimarães, p. 5-10, 1999

[Mattiasson, 1991]
Matiasson K., L. Bernspång, A. Honecker, E. Schedin, T. Hamman, A. Melander, 'On the use of explicit time integration in finite element simulation of industrial sheet metal forming processes', Proceedings of the 1st International Conference on Numerical Simulations of 3-D Sheet Metal Forming Processes, VDI-Berichte 894, VDI Verlag GmbH, Dusseldorf, p. 479-498, 1991

[Meinders, 1999]
Meinders T., A. van den Berg, J. Huétink, 'Deep drawing simulations of tailored blanks and experimental verification', International Sheet Metal Review, Mack Brooks publishing, vol. 1, p. 80-83, 1999

[Numiform, 1986]
Proceedings of the 2nd International Conference on Numerical Methods in Industrial Forming Processes, K. Mattiasson et al. (eds.), Balkema, Rotterdam, ISBN 90-61916593, 1986

[Numiform, 1989]
Proceedings of the 3rd International Conference on Numerical Methods in Industrial Forming Processes, E.G. Thompson et al. (eds.), Balkema, Rotterdam, ISBN 90-61918979, 1989

[Numiform, 1992]
Proceedings of the 4th International Conference on Numerical Methods in Industrial Forming Processes, J.L. Chenot et al. (eds.), Balkema, Rotterdam, ISBN 90-54100877, 1992

[Numiform, 1995]
Proceedings of the 5th International Conference on Numerical Methods in Industrial Forming Processes, S.F. Shen & P. Dawson (eds.), Balkema, Rotterdam, ISBN 90-54105534, 1995

[Numiform, 1998]
Proceedings of the 6th International Conference on Numerical Methods in Industrial Forming Processes, J. Huétink & F.P.T. Baaijens (eds.), Balkema, Rotterdam, ISBN 90-5410970X, 1998

[Numisheet, 1991]
Proceedings of the 1st International Conference on Numerical Simulations of 3-D Sheet Metal Forming Processes, VDI-Berichte 894, VDI Verlag GmbH, Dusseldorf, ISBN 3-180908947, 1991

[Numisheet, 1993]
Proceedings of the 2nd International Conference on Numerical Simulations of 3-D Sheet Metal Forming Processes, A. Makinouchi et al. (eds.), Isehara, 1993

[Numisheet, 1996]
Proceedings of the 3rd International Conference on Numerical Simulations of 3-D Sheet Metal Forming Processes, J.K. Lee et al. (eds.), Dearborn, Michigan, 1996

[Numisheet, 1999]
Proceedings of the 4th International Conference on Numerical Simulations of 3-D Sheet Metal Forming Processes, J.C. Gelin & P. Picard (eds.), Besançon, ISBN 2-844490018, 1999

[Saunders, 1996]
Saunders F.I., Wagoner R.H., 'Forming of tailor-welded blanks', Metallurgical and Materials Transactions A: Physical Metallurgy and Materials Science, vol. 27A, no. 9, p. 2605-2616, 1996

[Vegter, 1999]
Vegter H., Y. An, H.H. Pijlman, J. Huétink, 'Advanced mechanical testing on aluminium alloys and low carbon steels for sheet forming', Proceedings of the 4th International Conference on Numerical Simulations of 3-D Sheet Metal Forming Processes, J.C. Gelin & P. Picard (eds.), Besançon, vol. 1, p. 3-8, 1999

[Vreede, 1992]
Vreede P.T., 'A finite element method for simulations of 3-dimensional sheet metal forming', Ph.D. Thesis, University of Twente, Enschede, ISBN 90-90047549, 1992

2. Theoretical background to the finite element method

2.1 Introduction

Generally, numerical simulations of forming processes incorporate the deformation of a body on a macroscopic scale. The underlying micro-structural changes in the material are incorporated as a global average in a macroscopic approach, i.e. the material is treated as a continuous medium. An appropriate framework to describe the material behavior is therefore continuum mechanics. The basic premise for continuum mechanics is that all thermo-mechanical processes must obey the conservation laws concerning mass, momentum, and energy. In this work, continuum mechanics is restricted to mechanical processes where thermal effects are neglected since they are of minor importance in sheet metal forming. A weak form of mechanical equilibrium can be derived which is more convenient for numerical purposes. The finite element method based on this weak form, discretization and numerical integration is applied to solve the problem.

The kinematics of a deformable body concerns the motion of the material and coordinate system from a reference state to the final state and is treated in Section 2.2. To describe the material behavior it is necessary to have a measure for the amount of deformation (Section 2.3) which is unconditionally accompanied by stresses (Section 2.4). The strains and stresses are related via constitutive equations, which describe the material behavior (Section 2.5). The deformation process must obey the conservation law concerning momentum. Section 2.6 describes the derivation of the weak form of mechanical equilibrium. This weak form consists of a weighted integral formulation of equilibrium and boundary conditions. The finite element method is applied to find an approximate solution of the formulated weak mechanical equilibrium where use is made of the iterative Newton-Raphson procedure (Section 2.7).

This chapter is to a large extent based on the work of [Mooi, 1996], [Rietman, 1999] and [Huétink, 1999], where the work of Mooi and Rietman is largely based on the elaborate work of [Malvern, 1969], [Betten, 1991] and [Simo, 1998]. The following tensor notation is used in the present chapter and the subsequent chapters. A first order tensor (vector) is denoted by a bold character, a second order tensor is denoted by an underlined character, a third order tensor is denoted by an underlined bold character and finally a fourth order tensor is denoted by a double underlined character.

2.2 Kinematics

The kinematics of a deformable body concerns the motion of a material and coordinate system from an initial state (reference state) to the final situation. In the reference configuration a material particle is located at position $\boldsymbol{X}$, and the current (spatial) position of the material particle is defined as $\boldsymbol{x}$. Several definitions of motion can be used. In the reference description the only independent variables are the initial position $\boldsymbol{X}$ of a material particle in an arbitrary reference configuration and time t. In this definition the observer can be thought of as moving with the material particle. A special case is the Langrangian description in which the reference configuration is chosen to be the initial configuration at time $t = 0$. Another description of motion is the Eulerian description. Here the only independent variables are the current location $\boldsymbol{x}$ of a material particle and time *t*. In this definition the observer is located at a fixed point in space.

The motion of a continuum body is a one-parameter family of configurations indexed by time [Simo, 1998]. Explicitly, let $[0,T] \subset \Re^+$ be the time interval of interest. Then, for each $t \in [0,T]$, the mapping φ_t is defined as:

$$\varphi_t : \mathsf{B} \rightarrow \mathsf{S}_t \subset \Re^3 \tag{2-1}$$

which maps the reference configuration B onto the configuration $\mathsf{S} \subset \Re^3$ at time *t*, graphically represented in Figure 2-3.

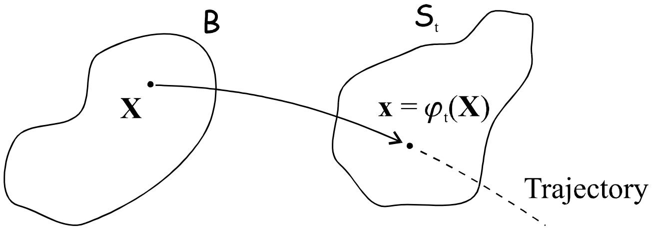

Figure 2-3. Motion of material point

Hence, the spatial position $\boldsymbol{x}$ for the position of $\boldsymbol{X} \in \mathsf{B}$ at time *t* becomes:

$$\boldsymbol{x} = \varphi_t(\boldsymbol{X}) = \varphi(\boldsymbol{X}, t) \tag{2-2}$$

From now on, the formulation is restricted to situations in which the spatial configuration initially equals the reference state ($\varphi(\boldsymbol{X}, t = 0) = \boldsymbol{X}$). The displacement of a material particle is written as:

$$\boldsymbol{u} = \boldsymbol{x} - \boldsymbol{X} = \varphi(\boldsymbol{X}, t) - \boldsymbol{X} \tag{2-3}$$

Application of the concept of motion in evolving processes necessitates the introduction of time derivatives of field and state variables. The material time derivative of a certain field or state variable Θ in the Lagrangian description is defined for a material particle as:

$$\dot{\Theta}(\boldsymbol{X}, t) = \frac{\partial \Theta(\boldsymbol{X}, t)}{\partial t} \tag{2-4}$$

In this Lagrangian or material description the independent variable is the reference position $\boldsymbol{X}$. In the Eulerian or spatial description the only independent variable is the fixed position in space. The material time derivative for a material particle at spatial position $\boldsymbol{x}$ is derived to be:

$$\dot{\Theta}(\boldsymbol{X}, t) = \frac{\partial}{\partial t}\Theta(\boldsymbol{X}, t) = \frac{d}{dt}\theta(\boldsymbol{x}, t) = \frac{\partial \theta(\boldsymbol{x}, t)}{\partial t} + \frac{\partial \theta(\boldsymbol{x}, t)}{\partial \boldsymbol{x}} \cdot \frac{\partial \boldsymbol{x}}{\partial t} = \frac{\partial \theta(\boldsymbol{x}, t)}{\partial t} + \boldsymbol{v} \cdot \vec{\nabla} \theta(\boldsymbol{x}, t) \tag{2-5}$$

where θ is a certain field or state variable in the Eulerian description, $\vec{\nabla}$ is the pre-gradient and $\boldsymbol{v}$ is the spatial velocity. The material time derivative is split into two parts. The first part of the right hand side of equation (2-5) is the spatial time derivative which is viewed by an observer in a fixed position. The second term is the convective part; the value of θ at position $\boldsymbol{x}$ changes because another particle with a different value of θ passes by. The split into a spatial part and a convective part is necessary if θ is only known in Eulerian coordinates.

The deformation gradient $\underline{F}$ relates the spatial configuration to the reference configuration for a material particle:

$$\underline{F}(\boldsymbol{X},t)=\frac{\partial \boldsymbol{x}}{\partial \boldsymbol{X}}=\boldsymbol{x}\bar{\nabla}_0 \tag{2-6}$$

where $\bar{\nabla}_0$ is the post-gradient with respect to the initial coordinates. Taking the time derivative of $\underline{F}$ gives:

$$\dot{\underline{F}}=\frac{d}{dt}\frac{\partial \boldsymbol{x}}{\partial \boldsymbol{X}}=\frac{\partial \boldsymbol{v}}{\partial \boldsymbol{X}}=\frac{\partial \boldsymbol{v}}{\partial \boldsymbol{x}}\cdot\frac{\partial \boldsymbol{x}}{\partial \boldsymbol{X}}=\boldsymbol{v}\bar{\nabla}\cdot\underline{F} \tag{2-7}$$

The spatial velocity gradient $\underline{L}$ is defined by:

$$\underline{L}=\boldsymbol{v}\bar{\nabla}=\dot{\underline{F}}\cdot\underline{F}^{-1} \tag{2-8}$$

Generally, a 2nd order tensor can be decomposed into a symmetric part and a skew-symmetric part:

$$\underline{L}=\underline{D}+\underline{W} \tag{2-9}$$

where $\underline{D}$ is the symmetric spatial rate of deformation:

$$\underline{D}=\tfrac{1}{2}\left(\underline{L}+\underline{L}^{T}\right) \tag{2-10}$$

and $\underline{W}$ is the skew-symmetric spin tensor:

$$\underline{W}=\tfrac{1}{2}\left(\underline{L}-\underline{L}^{T}\right) \tag{2-11}$$

Another commonly adopted decomposition is the polar decomposition. The deformation gradient is multiplicatively decomposed into an orthogonal rotation tensor $\underline{R}^{*}$ and a symmetric positive definite stretch tensor $\underline{U}$ (right-) or $\underline{V}$ (left-), see equation (2-12). The polar decomposition can be interpreted as a rigid rotation after deformation or vice versa.

$$\underline{F}=\underline{R}^{*}\cdot\underline{U}=\underline{V}\cdot\underline{R}^{*} \tag{2-12}$$

The right stretch tensor $\underline{U}$ is invariant and the left stretch tensor $\underline{V}$ is objective. A tensor is invariant if it does not change as a result of rigid body motion. Objectivity means that an observer, wherever he may be located, always observes the same strain in a given body. In other words, when a rigid body rotation $\underline{Q}$ is added to the motion of a body, then objective tensors are modified by multiplying by $\underline{Q}$. In mathematical notation, a vector $\boldsymbol{v}$ and a second order tensor $\underline{T}$ transform with:

$$\begin{aligned}\boldsymbol{v}^{*}&=\underline{Q}\cdot\boldsymbol{v}\\ \underline{T}^{*}&=\underline{Q}\cdot\underline{T}\cdot\underline{Q}^{T}\end{aligned} \tag{2-13}$$

where $\underline{Q}$ is an orthogonal second order tensor and the asterisk denotes the transformed state.

For elastoplastic material behavior, the deformation has to be subdivided into an elastic part and a plastic part:

$$\underline{U}=\underline{U}^{e}\cdot\underline{U}^{p} \tag{2-14}$$

Generally, this multiplicative decomposition does not result into two symmetric tensors. Consequently, a polar decomposition of the deformation gradient into a symmetric part and a rotation part is not convenient in the case of elastoplasticity. Therefore a weaker (not unique) decomposition is introduced:

$$\underline{F} = \underline{R} \cdot \underline{G} \tag{2-15}$$

Here the orthogonal rotation tensor $\underline{R}$ contains rigid body rotations, and the deformation tensor $\underline{G}$ contains the symmetric part of the deformation and the rotation of the material orientation (development of texture during forming). Note that this deformation tensor $\underline{G}$ is not necessarily symmetric. The tensors $\underline{R}$ and $\underline{G}$ relate to the spin tensor $\underline{W}$ and the rate of deformation tensor $\underline{D}$ as follows. The spatial velocity gradient $\underline{L}$ can be written as:

$$\underline{L} = \underline{\dot{F}} \cdot \underline{F}^{-1} = \left(\underline{\dot{R}} \cdot \underline{G} + \underline{R} \cdot \underline{\dot{G}}\right) \cdot \underline{G}^{-1} \cdot \underline{R}^{T} = \underline{\dot{R}} \cdot \underline{R}^{T} + \underline{R} \cdot \underline{\dot{G}} \cdot \underline{G}^{-1} \cdot \underline{R}^{T} \tag{2-16}$$

Next, it is defined that the orthogonal rotation tensor $\underline{R}$ relates to the spin tensor $\underline{W}$ through:

$$\underline{\dot{R}} \cdot \underline{R}^{T} = \underline{W} \tag{2-17}$$

Consequently, see equation (2-9), the deformation tensor $\underline{G}$ relates to the rate of deformation tensor $\underline{D}$ through:

$$\underline{D} = \underline{R} \cdot \underline{\dot{G}} \cdot \underline{G}^{-1} \cdot \underline{R}^{T} \tag{2-18}$$

Since $\underline{D}$ is symmetric, it can be concluded that $\underline{\dot{G}} \cdot \underline{G}^{-1}$ is also symmetric (equations (2-9) and (2-17)). The invariant rate of deformation tensor $\underline{D}^{*}$ equals:

$$\underline{D}^{*} = \underline{\dot{G}} \cdot \underline{G}^{-1} \tag{2-19}$$

The deformation tensor $\underline{G}$ can be decomposed into a reversible (elastic) part $\underline{G}^{e}$ and an irreversible (plastic) part $\underline{G}^{p}$:

$$\underline{G} = \underline{G}^{e} \cdot \underline{G}^{p} \tag{2-20}$$

The deformation gradient can also be decomposed into a reversible part $\underline{F}^{e}$ and an irreversible part $\underline{F}^{p}$:

$$\underline{F} = \underline{F}^{e} \cdot \underline{F}^{p} \tag{2-21}$$

Since decomposition into a reversible part and an irreversible part is not unique, the deformation tensor $\underline{G}$ can also be written as:

$$\underline{G} = \underline{G}^{e} \cdot \underline{Q} \cdot \underline{Q}^{T} \cdot \underline{G}^{p} \tag{2-22}$$

where $\underline{Q}$ is an orthogonal tensor that satisfies the requirement that $\underline{G}^{e} \cdot \underline{Q}$ is symmetric. Next define:

$$\underline{U}^{e} = \underline{G}^{e} \cdot \underline{Q} \tag{2-23}$$

$$\underline{F}^{p} = \underline{Q}^{T} \cdot \underline{G}^{p}$$

Note that $\underline{Q}^{T} \cdot \underline{G}^{p}$ is generally not symmetric. The deformation tensor $\underline{G}$ can now be written as:

$$\underline{G} = \underline{U}^{e} \cdot \underline{F}^{p} \tag{2-24}$$

Substituting equations (2-24) and (2-21) into equation (2-15) gives the relation between $\underline{F}^{e}$ and $\underline{U}^{e}$:

$$\underline{F}^{e} = \underline{R} \cdot \underline{U}^{e} \tag{2-25}$$

Note that when the total deformation is elastic, equation (2-25) does not degenerate to the polar decomposition (equation (2-12)). In that case, $\underline{G}^p$ is the unit tensor and $\underline{F}^p = \underline{Q}^T$, see equation (2-23).

2.3 Strain definition

For the description of material behavior it is necessary to have a measure for the amount of deformation. The definition of the deformation gradient is utilized for this purpose, defining the right and the left Cauchy-Green tensors respectively:

$$\underline{C} = \underline{F}^T \cdot \underline{F} \qquad (2\text{-}26)$$

$$\underline{B} = \underline{F} \cdot \underline{F}^T$$

The Cauchy-Green tensors are called metric tensors because they describe the deformed metric of a body. The right Cauchy-Green tensor $\underline{C}$, also called the Cauchy tensor, is invariant. The left Cauchy-Green tensor $\underline{B}$, also called the Finger tensor, is objective.

The right and left Cauchy-Green tensors are indeed a measure for the strain since they map the length of an infinitesimal vector in the initial configuration onto the length of the same infinitesimal vector in the current state. The length of a current infinitesimal vector $\boldsymbol{dx}$ in the Lagrangian coordinates is defined by:

$$ds^2 = \boldsymbol{dx} \cdot \boldsymbol{dx} = \left(\underline{F} \cdot \boldsymbol{dX}\right) \cdot \left(\underline{F} \cdot \boldsymbol{dX}\right) = \left(\underline{F}^T \cdot \underline{F}\right) : \boldsymbol{dXdX} = \underline{C} : \boldsymbol{dXdX} \qquad (2\text{-}27)$$

Likewise, the length of the initial vector $\boldsymbol{dX}$ can be obtained in Eulerian coordinates:

$$ds_0^2 = \boldsymbol{dX} \cdot \boldsymbol{dX} = \left(\underline{F}^{-1} \cdot \boldsymbol{dx}\right) \cdot \left(\underline{F}^{-1} \cdot \boldsymbol{dx}\right) = \left(\underline{F} \cdot \underline{F}^T\right)^{-1} : \boldsymbol{dxdx} = \underline{B}^{-1} : \boldsymbol{dxdx} \qquad (2\text{-}28)$$

If there is no deformation both Cauchy-Green tensors equal the unit tensor. From an engineering point of view it is much more convenient to work with a strain measure which vanishes in the case of zero deformation. This is obtained when considering the length difference before and after deformation:

$$ds^2 - ds_0^2 = \boldsymbol{dx} \cdot \boldsymbol{dx} - \boldsymbol{dX} \cdot \boldsymbol{dX} \qquad (2\text{-}29)$$

$$= (\underline{C} - \underline{I}) : \boldsymbol{dXdX} = 2\underline{E} : \boldsymbol{dXdX} \qquad (2\text{-}30)$$

$$= (\underline{I} - \underline{B}^{-1}) : \boldsymbol{dxdx} = 2\underline{e} : \boldsymbol{dxdx} \qquad (2\text{-}31)$$

where $\underline{E}$ is the Lagrangian or Green-Lagrange strain tensor, $\underline{e}$ is the Eulerian or Euler-Almansi strain tensor and $\underline{I}$ is the second order unit tensor. Both strain tensors can be written in terms of displacements. First note that the gradient of the displacement $\boldsymbol{u}$ reads, in Lagrangian and Eulerian coordinates, respectively:

$$\boldsymbol{u}\overleftarrow{\nabla}_0 = \frac{\partial \boldsymbol{u}}{\partial \boldsymbol{X}} = \frac{\partial(\boldsymbol{x} - \boldsymbol{X})}{\partial \boldsymbol{X}} = \frac{\partial \boldsymbol{x}}{\partial \boldsymbol{X}} - \underline{I} = \underline{F} - \underline{I} \qquad (2\text{-}32)$$

$$\boldsymbol{u}\overleftarrow{\nabla} = \frac{\partial \boldsymbol{u}}{\partial \boldsymbol{x}} = \frac{\partial(\boldsymbol{x} - \boldsymbol{X})}{\partial \boldsymbol{x}} = \underline{I} - \frac{\partial \boldsymbol{X}}{\partial \boldsymbol{x}} = \underline{I} - \underline{F}^{-1}$$

Then, the Green-Lagrange strain tensor and the Euler-Almansi strain tensors can be written in terms of displacements:

$$\underline{E} = \tfrac{1}{2}\left(\boldsymbol{u}\overleftarrow{\nabla}_0 + \overrightarrow{\nabla}_0\boldsymbol{u} + \overrightarrow{\nabla}_0\boldsymbol{u}\cdot\boldsymbol{u}\overleftarrow{\nabla}_0\right) \tag{2-33}$$

$$\underline{e} = \tfrac{1}{2}\left(\boldsymbol{u}\overleftarrow{\nabla} + \overrightarrow{\nabla}\boldsymbol{u} - \overrightarrow{\nabla}\boldsymbol{u}\cdot\boldsymbol{u}\overleftarrow{\nabla}\right)$$

Both strain tensors are frequently used in engineering mechanics. The rate of deformation tensor relates to the Euler-Almansi tensor via:

$$\underline{D} = \dot{\underline{e}} + \underline{e}\cdot\underline{L} + \underline{L}^T\cdot\underline{e} \tag{2-34}$$

which is also known as the Cottler-Rivlin derivative of $\underline{e}$. This relation is obtained by combining the time derivatives of the right hand side of equations (2-29) and (2-31). The rate of deformation tensor relates to the Green-Lagrange tensor via the time derivatives of equations (2-29) and (2-30):

$$\dot{\underline{E}} = \underline{F}^T\cdot\underline{D}\cdot\underline{F} \tag{2-35}$$

The nonlinear terms in equation (2-33) can be neglected for small displacements. Also the current state nearly equals the reference state for small displacements so that the Green-Lagrange strain tensor and the Euler-Almansi tensor approach the classical linear strain tensor $\underline{\varepsilon}$:

$$\underline{\varepsilon} = \tfrac{1}{2}\left(\boldsymbol{u}\overleftarrow{\nabla} + \overrightarrow{\nabla}\boldsymbol{u}\right) \approx \underline{E} \approx \underline{e} \tag{2-36}$$

For small displacements, the Cauchy-Green tensors and the classical linear strain tensor are related through:

$$\underline{C} \approx \underline{B} \approx \underline{I} + 2\underline{\varepsilon}, \qquad \underline{C}^{-1} \approx \underline{B}^{-1} \approx \underline{I} - 2\underline{\varepsilon} \tag{2-37}$$

2.4 Stress definition

Stresses are the response to a certain deformation of a body. The stress is historically defined as force per unit area. The Eulerian stress or Cauchy stress tensor $\underline{\sigma}$ is defined as follows by demanding equilibrium in the current configuration:

$$d\boldsymbol{P} = \boldsymbol{n}\cdot\underline{\sigma}dS \tag{2-38}$$

where dS is an infinitesimal surface on which a force $d\boldsymbol{P}$ acts. The Cauchy stress is also known as the true stress since the actual surface is used for its definition. The Cauchy stress is objective by definition in order to fulfill the physical consideration that the stress may not depend on the motion of the observer. By considering the equilibrium of moments in an infinitesimal volume it follows that:

$$\underline{\sigma} = \underline{\sigma}^T \tag{2-39}$$

which is known as the second law of Cauchy. However, the material time derivative of the Cauchy stress is not an objective stress rate [Malvern, 1969]. To overcome this problem, modified time derivatives may be constructed to preserve objectivity. A commonly used objective rate is the corotational stress rate which is frequently referred to as the Jaumann stress rate:

$$\overset{\circ}{\underline{\sigma}} = \dot{\underline{\sigma}} - \underline{W}\cdot\underline{\sigma} + \underline{\sigma}\cdot\underline{W} \tag{2-40}$$

According to Green and Naghdi, also an invariant Cauchy stress tensor $\underline{\sigma}^*$ can be defined:

$$\underline{\sigma}^* = \underline{R}^T \cdot \underline{\sigma} \cdot \underline{R} \tag{2-41}$$

where $\underline{R}$ is defined through equations (2-15) and (2-17). Note that the components of $\underline{\sigma}$, which refer to a global basis $\boldsymbol{e}_i$, are equal to the components of $\underline{\sigma}^*$, when referred to a local basis $\boldsymbol{b}_i = \underline{R}^T \cdot \boldsymbol{e}_i$:

$$\underline{\sigma} = \boldsymbol{e}_i \sigma_{ij} \boldsymbol{e}_j \tag{2-42}$$

$$\underline{\sigma}^* = \boldsymbol{b}_i \sigma_{ij} \boldsymbol{b}_j$$

As for strains, a Lagrangian definition for stresses can also be constructed. The 2nd Piola-Kirchhoff stress tensor $\underline{S}$ is defined in the reference configuration and can be obtained from the Cauchy stress by:

$$\underline{S} = J \underline{F}^{-T} \cdot \underline{\sigma} \cdot \underline{F}^{-1} \tag{2-43}$$

where the Jacobian J is the determinant of the deformation gradient $\underline{F}$ and is a measure for volumetric deformation. The 2nd Piola-Kirchhoff stress tensor is symmetric and is also invariant since it is completely defined with respect to the unchanging Lagrangian coordinates.

2.5 Constitutive relations

The strains and conjugate stresses derived within the framework of continuum mechanics are related through constitutive equations. The constitutive equations can be considered as the response of a material to an applied load. Since different types of material behave in different ways, the constitutive equations must include characteristic material responses.

The uniaxial tensile test is commonly adopted to study the plastic deformation of metallic materials. The uniaxial true stress and the true, logarithmic or natural strain are defined as follows:

$$\sigma = \frac{F}{A}, \qquad \varepsilon = \ln \frac{l}{l_0} \tag{2-44}$$

where F is the applied load, A is the current cross-sectional area, l is the current length of the test specimen and l_0 is the initial length of the test specimen. The true stress may be interpreted as the Cauchy stress in one dimension. Generally the true stress versus the true strain curve shows the characteristics as given in Figure 2-4.

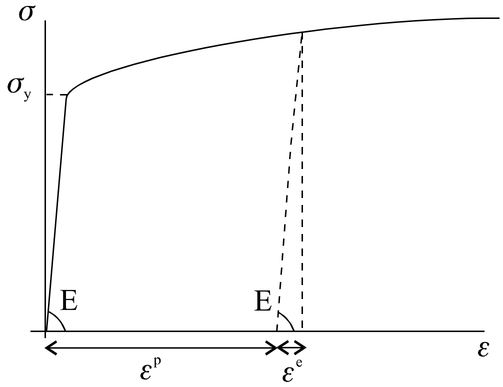

Figure 2-4. Stress-strain curve

Generally, the deformation of a metallic material can be subdivided into two stages. The first stage is the elastic deformation and is characterized by a linear dependence between the stress and the strain. It is covered by the well known Hooke's law for elasticity $\sigma = E\varepsilon^e$, where E is the elasticity or Young's modulus. The second stage is plastic deformation concerning work hardening. The stress increases with increasing strain with a ratio much smaller than Young's modulus. After unloading, a residual strain remains which is the plastic part of the deformation ε^p. The slope of the stress-strain curve during unloading is assumed to be constant. As a consequence, the total strain can be decomposed into an elastic strain and a plastic strain.

However, in forming processes the deformation is multiaxial rather than uniaxial. Therefore a multiaxial formulation must be introduced. The starting point of this formulation uses Hooke's law in tensor form, where the rate form of the invariant Cauchy stress $\underline{\sigma}^*$ is related to an invariant strain measure through a constant tensor $\underline{\underline{E}}^{/}$:

$$\underline{\sigma}^* = \underline{\underline{E}}^{/} : (\underline{C}^e - \underline{I}) \tag{2-45}$$

where $\underline{C}^e$ is the elastic right Cauchy-Green tensor. Hence, the rate of the invariant Cauchy stress can be written as:

$$\dot{\underline{\sigma}}^* = \underline{\underline{E}}^{/} : \dot{\underline{C}}^e \tag{2-46}$$

The rate of the elastic right Cauchy-Green tensor can be expressed in terms of the rate of deformation tensor:

$$\dot{\underline{C}}^e = \frac{d}{dt}(\underline{F}^{e^T} \cdot \underline{F}^e) = \dot{\underline{F}}^{e^T} \cdot \underline{F}^e + \underline{F}^{e^T} \cdot \dot{\underline{F}}^e = \underline{F}^{e^T} \cdot (\underline{L}^e + \underline{L}^{e^T})\underline{F}^e = 2\underline{F}^{e^T} \cdot \underline{D}^e \cdot \underline{F}^e \tag{2-47}$$

or, when using the decomposition of the deformation gradient as given in equation (2-25):

$$\dot{\underline{C}}^e = 2\underline{U}^e \cdot \underline{R}^T \cdot \underline{D}^e \cdot \underline{R} \cdot \underline{U}^e \tag{2-48}$$

Generally, the elastic part of deformation is very small in metal forming processes and consequently $\underline{U}^e$ can be approximated by the second order unit tensor. Hence, equation (2-48) can be written as:

$$\dot{\underline{C}}^e = 2\underline{R}^T \cdot \underline{D}^e \cdot \underline{R} = 2\underline{D}^{e*} \tag{2-49}$$

where the invariant rate of elastic deformation is defined by $\underline{D}^{e*}$. Substituting equation (2-49) into equation (2-46) gives an expression for the rate of the invariant Cauchy stress:

$$\dot{\underline{\sigma}}^* = \underline{\underline{E}} : \underline{D}^{e*} \tag{2-50}$$

where $\underline{\underline{E}}$ is the experimentally determined fourth order elasticity tensor.

In order to extend this constitutive rate equation to plastic deformation, the total strain rate is decomposed into an elastic part and a plastic part:

$$\underline{D}^* = \underline{D}^{e*} + \underline{D}^{p*} \tag{2-51}$$

Plastic deformation is defined to occur when the multiaxial stress state reaches the yield surface ϕ, represented in a six-dimensional stress space by:

$$\phi = \phi(\underline{\sigma}^*, \underline{\beta}) = 0 \tag{2-52}$$

where the tensor $\underline{\beta}$ represents the hardening. In case of isotropic hardening this tensor $\underline{\beta}$ can be written as $\underline{I}\kappa$, where κ is the equivalent plastic strain. The deformation is elastic when $\phi < 0$ or $\phi = 0 \wedge \dot{\phi} < 0$. Plastic deformation occurs when $\phi = 0 \wedge \dot{\phi} = 0$. Furthermore, the plastic deformation rate is related to the gradient of a plastic potential according to the normality or flow rule. Associated flow is assumed, which means that the plastic potential and the yield function coincide. Consequently, the plastic deformation rate is orthogonal to the yield surface:

$$\underline{D}^{p*} = \dot{\lambda}\frac{\partial \phi}{\partial \underline{\sigma}^*} \tag{2-53}$$

where $\dot{\lambda}$ is the plastic multiplier, a scaling constant. Substituting the relations for the plastic strain, equations (2-51) and (2-53), into the constitutive rate equation (2-50), gives:

$$\dot{\underline{\sigma}}^* = \underline{\underline{E}} : \left(\underline{D}^* - \dot{\lambda}\frac{\partial \phi}{\partial \underline{\sigma}^*} \right) \tag{2-54}$$

Assuming a given description of the yield function, the only unknown to be determined is the plastic multiplier $\dot{\lambda}$. As stated before, for plastic deformation the stress must lie on the yield surface and it must also remain on the yield surface, so that:

$$\dot{\phi} = \frac{\partial \phi}{\partial \underline{\sigma}^*} : \dot{\underline{\sigma}}^* + \frac{\partial \phi}{\partial \underline{\beta}} : \dot{\underline{\beta}} = 0 \tag{2-55}$$

The second term in equation (2-55) represents the hardening and is proportional to the plastic multiplier. Therefore this second term is a regular function of the plastic multiplier which vanishes if the plastic multiplier vanishes. Without loss of generality, equation (2-55) can be written as:

$$\dot{\phi} = \frac{\partial \phi}{\partial \underline{\sigma}^*} : \dot{\underline{\sigma}}^* + f\dot{\lambda} = 0 \tag{2-56}$$

where *f* is a scalar function which depends on the yield function used. Substituting equation (2-54) into (2-56) gives an expression for the plastic multiplier:

$$\frac{\partial \phi}{\partial \underline{\sigma}^*} : \underline{\underline{E}} : \left(\underline{D}^* - \dot{\lambda}\frac{\partial \phi}{\partial \underline{\sigma}^*} \right) + f\dot{\lambda} = 0 \quad \Leftrightarrow \tag{2-57}$$

$$\dot{\lambda} = \frac{\dfrac{\partial \phi}{\partial \underline{\sigma}^*} : \underline{\underline{E}} : \underline{D}^*}{\dfrac{\partial \phi}{\partial \underline{\sigma}^*} : \underline{\underline{E}} : \dfrac{\partial \phi}{\partial \underline{\sigma}^*} - f}$$

Substituting this expression for the plastic multiplier into the constitutive rate equation (2-54), gives the following constitutive rate equation:

$$\dot{\underline{\sigma}}^* = \left(\underline{\underline{E}} - (1-h)\underline{\underline{Y}} \right) : \underline{D}^* \tag{2-58}$$

where:

$$h = \frac{f}{f - \frac{\partial \phi}{\partial \underline{\sigma}^*} : \underline{\underline{E}} : \frac{\partial \phi}{\partial \underline{\sigma}^*}} \tag{2-59}$$

and:

$$\underline{\underline{Y}} = \frac{\underline{\underline{E}} : \frac{\partial \phi}{\partial \underline{\sigma}^*} \frac{\partial \phi}{\partial \underline{\sigma}^*} : \underline{\underline{E}}}{\frac{\partial \phi}{\partial \underline{\sigma}^*} : \underline{\underline{E}} : \frac{\partial \phi}{\partial \underline{\sigma}^*}} \tag{2-60}$$

2.6 Weak equilibrium

All thermo-mechanical processes must obey the conservation laws concerning mass, momentum, and energy. In this work, the attention is restricted to mechanical processes where thermal effects are neglected since they are only of minor importance in sheet metal forming. In other words, an arbitrary body must be in mechanical equilibrium, i.e. it obeys the conservation law of momentum:

$$\underline{\sigma} \cdot \bar{\nabla} + \rho \boldsymbol{f} = \rho \dot{\boldsymbol{v}} \tag{2-61}$$

where $\boldsymbol{f}$ represents body forces. For many forming processes the inertia forces ($\rho \dot{\boldsymbol{v}}$) can be neglected since these processes are relatively slow. The strong formulation of the mechanical problem is to find a solution $\boldsymbol{u}$, so that mechanical equilibrium within the domain V and the boundary conditions on surface S are fulfilled:

$$\begin{aligned} &\underline{\sigma} \cdot \bar{\nabla} + \rho \boldsymbol{f} = 0 && \text{in } V \\ &\boldsymbol{u} = \boldsymbol{u}_0 && \text{on } S_u \\ &\underline{\sigma} \cdot \boldsymbol{n} = \boldsymbol{t} && \text{on } S_t \end{aligned} \tag{2-62}$$

where $\boldsymbol{n}$ is the outward normal with respect to the boundary, $\boldsymbol{t}$ is the surface traction and $\boldsymbol{u}_0$ are the prescribed displacements. However, the strong form of equilibrium is stringent. It demands that the gradient of the stress exist, which means that the stress distribution within the domain must be continuous. However, for numerical purposes it is more convenient to derive a weak formulation of equilibrium. This can be achieved by weighting the equilibrium conditions with arbitrary weight functions $\delta \boldsymbol{v}$ in an integral formulation, such that the solution is less constrained by differentiability demands:

$$\int_V \delta \boldsymbol{v} \cdot (\underline{\sigma} \cdot \bar{\nabla}) dV + \int_V \rho \delta \boldsymbol{v} \cdot \boldsymbol{f} dV - \int_S \delta \boldsymbol{v} \cdot (\underline{\sigma} \cdot \boldsymbol{n} - \boldsymbol{t}) dS = 0 \tag{2-63}$$

The only requirement the weight functions have to fulfill is that they are piecewise differentiable. Applying the following chain rule:

$$\delta \boldsymbol{v} \cdot (\underline{\sigma} \cdot \bar{\nabla}) = (\delta \boldsymbol{v} \cdot \underline{\sigma}) \cdot \bar{\nabla} - \delta \boldsymbol{v} \bar{\nabla} : \underline{\sigma} \tag{2-64}$$

as well as the Gauss divergence theorem:

$$\int_V \boldsymbol{g} \cdot \bar{\nabla} dV = \int_S \boldsymbol{g} \cdot \boldsymbol{n} dS \tag{2-65}$$

to equation (2-63), yields the following expression for the weak mechanical equilibrium:

$$\int_V \delta\boldsymbol{v}\overleftarrow{\nabla}:\underline{\sigma}dV = \int_V \rho\delta\boldsymbol{v}\cdot\boldsymbol{f}dV + \int_S \delta\boldsymbol{v}\cdot\boldsymbol{t}dS \tag{2-66}$$

Note that only the stress and not the gradient of the stress must be known in this weak formulation. This implies that the stress needs not be continuous, but can for example be piecewise linear, which is an ideal starting point for a finite element procedure.

2.7 Finite element method

A spatial discretization can be used to find an approximate solution of the previously formulated weak mechanical equilibrium equations. Historically, the most common way to discretize domains for structural and plasticity problems is a finite element discretization, which will be treated in Section 2.7.1 [Zienkiewicz, 1991].

The expressions in the weak mechanical equilibrium are generally non-linear and therefore an incremental-iterative procedure is applied to solve the problem. The weak equilibrium equations are evaluated at a number of discrete points in the time domain. Considering one such time increment, the field and state variables are known at the start of the time increment $t^{(n)}$, whereas they are unknown at the end of the time increment $t^{(n+1)}$. In a standard implicit manner the problem can be written as:

$$\begin{aligned}
\boldsymbol{x}^{(n+1)} &= \boldsymbol{x}^{(n)} + \Delta\boldsymbol{u} \\
\underline{\varepsilon}^{(n+1)} &= \underline{\varepsilon}^{(n)} + \Delta\underline{\varepsilon} \\
\underline{\sigma}^{(n+1)} &= f(\underline{\varepsilon}^{(n+1)})
\end{aligned} \tag{2-67}$$

where use is made of $\boldsymbol{u} = \boldsymbol{v}\Delta t$ and $\Delta\underline{\varepsilon} = \underline{D}\Delta t = ½(\Delta\boldsymbol{u}\overleftarrow{\nabla}+\overrightarrow{\nabla}\Delta\boldsymbol{u})$. The stress state at the end of the time increment is determined with a stress update algorithm, see Chapter 3. In order to obtain global equilibrium values at the end of the time increment, an iterative algorithm must be applied. In this work the well-known Newton-Raphson iterative procedure is used and is described in Section 2.7.2. When the equilibrium values are determined, the current configuration is used as the initial configuration for the next increment: $\mathsf{B}^{(n+1)} := \mathsf{S}^{(n)}$.

2.7.1 Finite element discretization

The finite element discretization of a domain V consists of the definition of subdomains with a finite size V_e, the elements, and the respective interpolation functions. Evaluation of integrals is performed over these elements. Later, the contribution of each element is assembled into a large system representing the whole domain, yielding an approximate solution for the whole domain.

An element is defined by means of pre-defined points, the nodes. Within the element, use is made of natural coordinates which are only valid in one element. The interpolation functions have to provide continuous functions for the interpolated field and state variables within an element. The interpolation functions relate quantities at any point in the interior of the element to the nodal point values. For isoparametric elements the same interpolation is applied for both the geometry and the independent field variables ξ:

$$\boldsymbol{x} = \sum_{\alpha=1}^{n} N^{\alpha} \boldsymbol{x}^{\alpha} \tag{2-68}$$

$$\xi = \sum_{\alpha=1}^{n} N^{\alpha} \xi^{\alpha}$$

where N^{α} is the time independent interpolation function for node α of the element and n is the number of nodes per element. The summation operator will be omitted from now on, since the summation convention applies. Integrals over the element are determined using numerical integration. Accurate higher order integration is obtained by Gaussian quadrature [Bathe, 1982], [Segerlind, 1984]. The Gauss points are often referred to as integration points.

To discretize the weak mechanical equilibrium, all continuous field variables and their gradients are determined by the interpolation functions and the nodal values, leading to:

$$\boldsymbol{v} = N^{\alpha} \boldsymbol{v}^{\alpha} \qquad \delta\boldsymbol{v} = N^{\alpha} \delta\boldsymbol{v}^{\alpha} \tag{2-69}$$

$$\boldsymbol{v}\overleftarrow{\nabla} = \underline{L} = \boldsymbol{v}^{\alpha}\overleftarrow{\nabla}N^{\alpha} \qquad \delta\boldsymbol{v}\overleftarrow{\nabla} = \delta\boldsymbol{v}^{\alpha}\overleftarrow{\nabla}N^{\alpha}$$

The rate of deformation is written as:

$$\underline{D} = \tfrac{1}{2}(v_{i,j} + v_{j,i}) = \tfrac{1}{2}(N^{\alpha}_{,j}\delta_{ik} + N^{\alpha}_{,i}\delta_{jk})v^{\alpha}_{k} = B^{\alpha}_{ijk}v^{\alpha}_{k} = \underline{\boldsymbol{B}}^{\alpha} \cdot \boldsymbol{v}^{\alpha} = \boldsymbol{v}^{\alpha} \cdot \underline{\boldsymbol{B}}^{t\alpha} \tag{2-70}$$

where $\underline{\boldsymbol{B}}^{\alpha}$ and $\underline{\boldsymbol{B}}^{t\alpha}$ are third order tensors that relate the deformation rate tensor to the nodal velocity vector. These tensors read in tensor notation:

$$\underline{\boldsymbol{B}}^{\alpha} = \tfrac{1}{2}(\overleftarrow{\nabla}N^{\alpha}\underline{I} + \underline{\underline{T}}:\overleftarrow{\nabla}N^{\alpha}\underline{I}) \tag{2-71}$$

$$\underline{\boldsymbol{B}}^{t\alpha} = \tfrac{1}{2}(\underline{I}\overleftarrow{\nabla}N^{\alpha} + \underline{I}\overleftarrow{\nabla}N^{\alpha}:\underline{\underline{T}})$$

where $\underline{\underline{T}}$ is a fourth order index permutation tensor which reads in index notation $T_{ijkl} = \delta_{il}\delta_{jk}$. When $\underline{\boldsymbol{B}}^{t\alpha}$ is double contracted with a symmetric second order tensor $\underline{\varphi}$, the product degenerates to:

$$\underline{\boldsymbol{B}}^{t\alpha}:\underline{\varphi} = \underline{I}\overleftarrow{\nabla}N^{\alpha}:\underline{\varphi} \tag{2-72}$$

Using equation (2-69) in equation (2-66) gives the discretized form of the weak mechanical equilibrium:

$$\int_{V_e} \delta\boldsymbol{v}^{\alpha}\overleftarrow{\nabla}N^{\alpha}:\underline{\sigma}dV = \int_{V_e} \rho N^{\alpha}\delta\boldsymbol{v}^{\alpha} \cdot \boldsymbol{f}dV + \int_{S_e} N^{\alpha}\delta\boldsymbol{v}^{\alpha} \cdot \boldsymbol{t}dS \tag{2-73}$$

Or, after rewriting and substituting equation (2-72):

$$\delta\boldsymbol{v}^{\alpha} \cdot \int_{V_e} \underline{\boldsymbol{B}}^{t\alpha}:\underline{\sigma}dV = \delta\boldsymbol{v}^{\alpha} \cdot \int_{V_e} \rho N^{\alpha}\boldsymbol{f}dV + \delta\boldsymbol{v}^{\alpha} \cdot \int_{S_e} N^{\alpha}\boldsymbol{t}dS \qquad \Leftrightarrow \tag{2-74}$$

$$\delta\boldsymbol{v}^{\alpha} \cdot \boldsymbol{F}^{\alpha}_{int} = \delta\boldsymbol{v}^{\alpha} \cdot \boldsymbol{F}^{\alpha}_{ext}$$

where $\boldsymbol{F}^{\alpha}_{int}$ is the internal reaction force vector and $\boldsymbol{F}^{\alpha}_{ext}$ the external force vector. Since equation (2-74) must hold for all virtual velocity fields, the following equality is obtained for the internal and external force vector:

$$\boldsymbol{F}^{\alpha}_{int} = \boldsymbol{F}^{\alpha}_{ext} \tag{2-75}$$

2.7.2 Iterative Newton-Raphson procedure

The discrete equilibrium equation (2-75) is generally non-linear and can therefore be solved with the iterative Newton-Raphson procedure. A Newton-Raphson iteration consists of two stages which are referred to as the predictor step and the corrector step, respectively. In the predictor step an estimate of the solution is obtained based on linearization in the current iteration. The corrector step provides the resulting reaction force for this iteration.

The starting point of the Newton-Raphson procedure is the assumption that the displacement vector $\boldsymbol{u}_0$ is a good approximation to solve the equality equation. It is assumed that $\hat{\boldsymbol{u}}$ is the exact unknown solution of this non-linear equation and hence, define $\Delta\boldsymbol{u} = \hat{\boldsymbol{u}} - \boldsymbol{u}_0$. Consequently, the equality equation can be written as:

$$\boldsymbol{F}_{int}(\hat{\boldsymbol{u}}) = \boldsymbol{F}_{int}(\boldsymbol{u}_0 + \Delta\boldsymbol{u}) = \boldsymbol{F}_{ext} \tag{2-76}$$

Note that the superscript α, indicating the nodes, is omitted in this section to facilitate readability. Applying a Taylor series expansion to this equation yields:

$$\boldsymbol{F}_{int}(\hat{\boldsymbol{u}}) = \boldsymbol{F}_{int}(\boldsymbol{u}_0) + \left.\frac{d\boldsymbol{F}_{int}}{d\boldsymbol{u}}\right|_{\boldsymbol{u}_0} \cdot \Delta\boldsymbol{u} + O(\Delta\boldsymbol{u}^2) = \boldsymbol{F}_{ext} \tag{2-77}$$

Neglecting the higher order terms $O(\Delta\boldsymbol{u}^2)$ and rearranging gives:

$$\underline{K}_0 \cdot \Delta\boldsymbol{u}_1 = \boldsymbol{F}_{ext} - \boldsymbol{F}_{int}(\boldsymbol{u}_0) = \boldsymbol{R}_0 \qquad \text{with} \qquad \underline{K}_0 = \left.\frac{d\boldsymbol{F}_{int}}{d\boldsymbol{u}}\right|_{\boldsymbol{u}_0} \tag{2-78}$$

where $\underline{K}_0$ is the tangent stiffness matrix and $\boldsymbol{R}_0$ is the residual force vector which vanishes when the exact solution is found. The unknown displacement increment $\Delta\boldsymbol{u}_1$ can be solved using equation (2-78). However, $\boldsymbol{u}_0 + \Delta\boldsymbol{u}_1$ is no longer equal to the exact solution $\hat{\boldsymbol{u}}$, since the higher order terms are omitted. It is likely that the new approximation of the displacement vector, $\boldsymbol{u}_1 = \boldsymbol{u}_0 + \Delta\boldsymbol{u}_1$, is a better approximation for the exact solution than the old approximation $\boldsymbol{u}_0$. The procedure is repeated again using $\boldsymbol{u}_1$ as the initial approximation. With the new approximation $\boldsymbol{u}_1$, a new stiffness matrix $\underline{K}_1$ and internal force vector $\boldsymbol{F}_{int}(\boldsymbol{u}_1)$ are determined. Subsequently, $\Delta\boldsymbol{u}_2$ is calculated using equation (2-78) and the new displacement vector is set to $\boldsymbol{u}_2 = \boldsymbol{u}_1 + \Delta\boldsymbol{u}_2$. This procedure is repeated until a user-defined accuracy is reached, see equation (2-79).

```
$\boldsymbol{u}_0 = \boldsymbol{0}$ , $\boldsymbol{R}_0 = \boldsymbol{F}_{ext} - \boldsymbol{F}_{int}(\boldsymbol{u}_0)$ , $k = 0$
while $(\|\boldsymbol{R}_k\| > error)$ do
    determine $\underline{K}_k$
    $\underline{K}_k \cdot \Delta\boldsymbol{u}_{k+1} = \boldsymbol{F}_{ext} - \boldsymbol{F}_{int}(\boldsymbol{u}_k) = \boldsymbol{R}_k$
    $\boldsymbol{u}_{k+1} = \boldsymbol{u}_k + \Delta\boldsymbol{u}_{k+1}$
    determine $\boldsymbol{F}_{int}(\boldsymbol{u}_k)$
    $k := k + 1$
end while
```

(2-79)

In the above algorithm, it is assumed that $\boldsymbol{F}_{ext}$ does not depend on $\Delta\boldsymbol{u}$. However, if $\boldsymbol{F}_{ext}$ depends on $\Delta\boldsymbol{u}$ (e.g. in pressure loads), this can easily be incorporated in the algorithm.

In one dimension, the iterative Newton-Raphson process can be graphically represented as shown in Figure 2-5:

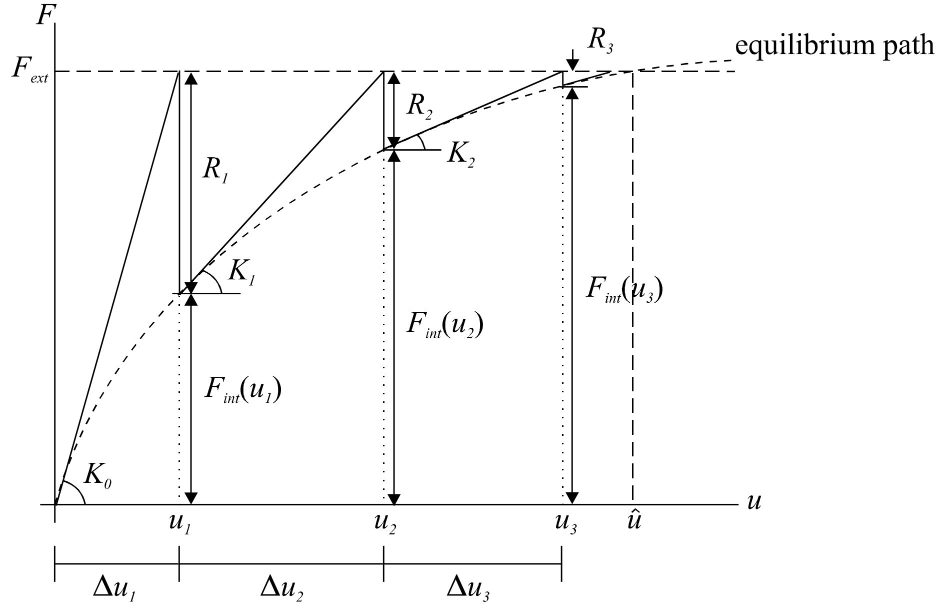

Figure 2-5. Newton-Raphson iteration scheme

The expressions for the internal force vector $\boldsymbol{F}_{int}(\boldsymbol{u}_k)$ and the stiffness matrix $\underline{K}_k$ must be determined in order to reach equilibrium using the iterative Newton-Raphson procedure.

2.7.2.1 Determination of the internal force vector

Within a numerical time increment, the total displacement is only determined at the start and the end of the time increment. The stress at the end of the time increment must be calculated. This is done by a stress update algorithm, see Chapter 3. In the in-house code DiekA this stress update algorithm is performed in a local coordinate system. The definition for the internal force vector is given in equation (2-74). However, this force vector is defined in terms of the Cauchy stress which is defined in the global coordinate system. Therefore the local invariant Cauchy stress $\underline{\sigma}^*$ has to be transformed to the Cauchy stress through equation (2-41). Consequently, the following expression for the internal force vector is obtained:

$$\boldsymbol{F}^{\alpha}_{int} = \int_{V_e} \underline{\boldsymbol{B}}^{t\alpha} : (\underline{R}\cdot\underline{\sigma}^{*}\cdot\underline{R}^{T})dV \tag{2-80}$$

2.7.2.2 Determination of the stiffness matrix

The starting point for the derivation of the stiffness matrix is the time derivative of the internal force vector:

$$\dot{\boldsymbol{F}}^{\alpha}_{int} = \frac{d\boldsymbol{F}^{\alpha}_{int}}{dt} = \frac{d\boldsymbol{F}^{\alpha}_{int}}{d\boldsymbol{u}^{\beta}}\cdot\frac{d\boldsymbol{u}^{\beta}}{dt} = \underline{K}^{\alpha\beta}\cdot\dot{\boldsymbol{u}}^{\beta} \tag{2-81}$$

Since the internal force vector is defined in the current configuration which changes in time, it will be difficult to derive the material time derivative of the internal force vector. Therefore the internal force vector is transformed into an integral with respect to the initial configuration. Then, the material time derivative of the integral only consists of the material time derivatives of the terms within the integral. After determining the material time derivative in the initial configuration, the integral is transformed to the current configuration. The transformation of the internal force vector from the current configuration to the initial configuration reads:

$$\boldsymbol{F}_{int}^{\alpha} = \int_{V_e} \underline{I}\vec{\nabla} N^{\alpha} : \underline{\sigma} dV = \int_{V_e} I_{ij} \frac{\partial N^{\alpha}}{\partial X_l} \frac{\partial X_l}{\partial x_k} \sigma_{jk} dV = \int_{V_{0,e}} \underline{I}\vec{\nabla}_0 N^{\alpha} : \left(\underline{\sigma} \cdot \underline{F}^{-T} \right) J dV_0 \tag{2-82}$$

where J is the Jacobian (determinant of the deformation gradient $\underline{F}$). The time derivative of the internal force vector becomes:

$$\dot{\boldsymbol{F}}_{int}^{\alpha} = \int_{V_{0,e}} \underline{I}\vec{\nabla}_0 N^{\alpha} : \left(\dot{\underline{\sigma}} \cdot \underline{F}^{-T} \right) J dV_0 + \int_{V_{0,e}} \underline{I}\vec{\nabla}_0 N^{\alpha} : \left(\underline{\sigma} \cdot \dot{\underline{F}}^{-T} \right) J dV_0 \tag{2-83}$$

where the time derivative of J is neglected since the volume changes are only elastic and very small. Note that when the time derivative of the density is incorporated in the constitutive equations, the time derivative of J cancels out with the extra term concerning the density, see [Mooi, 1996].

An expression must be found for the time derivative of the transposed form of the inverse of the deformation gradient $\underline{F}$:

$$\begin{aligned} &(\underline{F} \cdot \underline{F}^{-1})^{\dot{}} = \dot{\underline{F}} \cdot \underline{F}^{-1} + \underline{F} \cdot \dot{\underline{F}}^{-1} \quad \Leftrightarrow \\ &\dot{\underline{F}}^{-1} = -\underline{F}^{-1} \cdot \dot{\underline{F}} \cdot \underline{F}^{-1} = -\underline{F}^{-1} \cdot \underline{L} \cdot \underline{F} \cdot \underline{F}^{-1} = -\underline{F}^{-1} \cdot \underline{L} \quad \Rightarrow \\ &\dot{\underline{F}}^{-T} = -\underline{L}^{T} \cdot \underline{F}^{-T} \end{aligned} \tag{2-84}$$

Substitution of equation (2-84) in equation (2-83) gives:

$$\dot{\boldsymbol{F}}_{int}^{\alpha} = \int_{V_{0,e}} \underline{I}\vec{\nabla}_0 N^{\alpha} : \left(\dot{\underline{\sigma}} \cdot \underline{F}^{-T} \right) J dV_0 + \int_{V_{0,e}} \underline{I}\vec{\nabla}_0 N^{\alpha} : \left(\underline{\sigma} \cdot \underline{L}^{T} \cdot \underline{F}^{-T} \right) J dV_0 \tag{2-85}$$

The transformation of the time derivative of the internal force vector from the current to the initial configuration is obtained through equation (2-82):

$$\dot{\boldsymbol{F}}_{int}^{\alpha} = \int_{V_e} \underline{I}\vec{\nabla} N^{\alpha} : \dot{\underline{\sigma}} dV + \int_{V_e} \underline{I}\vec{\nabla} N^{\alpha} : \left(\underline{\sigma} \cdot \underline{L}^{T} \right) dV \tag{2-86}$$

This equation must be rewritten in terms of $\dot{\boldsymbol{u}}^{\beta}$. The time derivative of the Cauchy stress reads, see equation (2-41):

$$\dot{\underline{\sigma}} = \dot{\underline{R}} \cdot \underline{\sigma}^{*} \cdot \underline{R}^{T} + \underline{R} \cdot \dot{\underline{\sigma}}^{*} \cdot \underline{R}^{T} + \underline{R} \cdot \underline{\sigma}^{*} \cdot \dot{\underline{R}}^{T} \tag{2-87}$$

Now, the first term of the right hand side of equation (2-86) can be rewritten as:

$$\int_{V_e} \underline{I\vec{\nabla}}N^{\alpha} : (\dot{\underline{R}} \cdot \underline{\sigma}^{*} \cdot \underline{R}^{T} + \underline{R} \cdot \dot{\underline{\sigma}}^{*} \cdot \underline{R}^{T} + \underline{R} \cdot \underline{\sigma}^{*} \cdot \dot{\underline{R}}^{T}) dV = \tag{2-88}$$

$$\int_{V_e} \underline{I\vec{\nabla}}N^{\alpha} : (\dot{\underline{R}} \cdot \underline{R}^{-1} \cdot \underline{R} \cdot \underline{\sigma}^{*} \cdot \underline{R}^{T} + \underline{R} \cdot \dot{\underline{\sigma}}^{*} \cdot \underline{R}^{T} + \underline{R} \cdot \underline{\sigma}^{*} \cdot \underline{R}^{T} \cdot \underline{R}^{-T} \cdot \dot{\underline{R}}^{T}) dV =$$

$$\int_{V_e} \underline{I\vec{\nabla}}N^{\alpha} : (\dot{\underline{R}} \cdot \underline{R}^{T} \cdot \underline{\sigma} + \underline{R} \cdot \dot{\underline{\sigma}}^{*} \cdot \underline{R}^{T} + \underline{\sigma} \cdot \underline{R} \cdot \dot{\underline{R}}^{T}) dV$$

The following multiplication rule applies for permutation of products of tensors [Huétink, 1986]:

$$\underline{A} \cdot \underline{B} \cdot \underline{C} = (\underline{A} \cdot \underline{\underline{H}} \cdot \underline{C}^{T}) : \underline{B} \tag{2-89}$$

where $\underline{A}$, $\underline{B}$ and $\underline{C}$ are arbitrary second order tensors and $\underline{\underline{H}}$ is the fourth order unit tensor. Making use of equations (2-70) and (2-89), the second part of equation (2-88) reads:

$$\int_{V_e} \underline{I\vec{\nabla}}N^{\alpha} : \left(\underline{R} \cdot \dot{\underline{\sigma}}^{*} \cdot \underline{R}^{T}\right) dV = \int_{V_e} \underline{I\vec{\nabla}}N^{\alpha} : \left(\underline{R} \cdot \underline{\underline{H}} \cdot \underline{R}\right) : \dot{\underline{\sigma}}^{*} dV = \tag{2-90}$$

$$\int_{V_e} \underline{I\vec{\nabla}}N^{\alpha} : (\underline{R} \cdot \underline{\underline{H}} \cdot \underline{R}) : \underline{\underline{L}}^{y} : \underline{D}^{*} dV =$$

$$\int_{V_e} \underline{I\vec{\nabla}}N^{\alpha} : (\underline{R} \cdot \underline{\underline{H}} \cdot \underline{R}) : \underline{\underline{L}}^{y} : (\underline{R}^{T} \cdot \underline{\underline{H}} \cdot \underline{R}^{T}) : \underline{D} dV =$$

$$\int_{V_e} \underline{I\vec{\nabla}}N^{\alpha} : (\underline{R} \cdot \underline{\underline{H}} \cdot \underline{R}) : \underline{\underline{L}}^{y} : (\underline{R}^{T} \cdot \underline{\underline{H}} \cdot \underline{R}^{T}) : \boldsymbol{B}^{\beta} \cdot \dot{\boldsymbol{u}}^{\beta} dV$$

where the invariant rate of deformation tensor $\underline{D}^{*}$ relates to the rate of deformation tensor $\underline{D}$ through:

$$\underline{D}^{*} = \underline{R}^{T} \cdot \underline{D} \cdot \underline{R} \tag{2-91}$$

The fourth order tensor $\underline{\underline{L}}^{y}$ denotes the material tensor, which for example could be the continuum material tensor as given in equation (2-58).
Next, the first and third term of equation (2-88) have to be rewritten. It is derived that:

$$\dot{\underline{R}} \cdot \underline{R}^{T} = -\underline{R} \cdot \dot{\underline{R}}^{T} \tag{2-92}$$

making use of $(\underline{R} \cdot \underline{R}^{T}) = \underline{I}$. The deformation tensor $\underline{F}$ is decomposed as defined in equation (2-15) and subsequently it is defined that $\dot{\underline{R}} \cdot \underline{R}^{T}$ is equal to the spin tensor $\underline{W}$, see equation (2-17).
The first and third term of equation (2-88) can now be rewritten as:

$$\int_{V_e} \underline{I\vec{\nabla}}N^{\alpha} : \left(\dot{\underline{R}} \cdot \underline{R}^{T} \cdot \underline{\sigma} + \underline{\sigma} \cdot \underline{R} \cdot \dot{\underline{R}}^{T}\right) dV = \int_{V_e} \underline{I\vec{\nabla}}N^{\alpha} : (\underline{W} \cdot \underline{\sigma} - \underline{\sigma} \cdot \underline{W}) dV \tag{2-93}$$

Combining equation (2-93) with the second term of equation (2-86) gives:

$$\begin{aligned}&\int_{V_e} \underline{I}\vec{\nabla}N^{\alpha}:\left(\underline{W}\cdot\underline{\sigma}-\underline{\sigma}\cdot\underline{W}-\underline{\sigma}\cdot\underline{L}^{T}\right)dV = \\ &\int_{V_e} \underline{I}\vec{\nabla}N^{\alpha}:\left((\underline{L}-\underline{D})\cdot\underline{\sigma}-\underline{\sigma}\cdot\underline{W}-\underline{\sigma}\cdot(\underline{D}-\underline{W})\right)dV = \\ &\int_{V_e} \underline{I}\vec{\nabla}N^{\alpha}:\left(\underline{L}\cdot\underline{\sigma}\right)dV - \int_{V_e} \underline{I}\vec{\nabla}N^{\alpha}:\left(\left(\underline{\underline{H}}\cdot\underline{\sigma}+\underline{\sigma}\cdot\underline{\underline{H}}\right):\underline{D}\right)dV\end{aligned} \tag{2-94}$$

With equations (2-69) and (2-70) this expression becomes:

$$\int_{V_e} \underline{I}\vec{\nabla}N^{\alpha}\cdot\underline{\sigma}\cdot\vec{\nabla}N^{\beta}\cdot\dot{\boldsymbol{u}}^{\beta}dV - \int_{V_e} \underline{I}\vec{\nabla}N^{\alpha}:\left(\underline{\underline{H}}\cdot\underline{\sigma}+\underline{\sigma}\cdot\underline{\underline{H}}\right):\underline{\boldsymbol{B}}^{\beta}\cdot\dot{\boldsymbol{u}}^{\beta}dV \tag{2-95}$$

The time derivative of the internal force vector (equation (2-86)) is obtained by combining equations (2-90) and (2-95):

$$\begin{aligned}\dot{\boldsymbol{F}}^{\alpha}_{int} = &\int_{V_e} \underline{\boldsymbol{B}}^{t\alpha}:\begin{pmatrix}\left(\underline{R}\cdot\underline{\underline{H}}\cdot\underline{R}\right):\underline{\underline{L}}^{y}:(\underline{R}^{T}\cdot\underline{\underline{H}}\cdot\underline{R}^{T})- \\ \underline{\underline{H}}\cdot\underline{R}\cdot\underline{\sigma}^{*}\cdot\underline{R}^{T}-\underline{R}\cdot\underline{\sigma}^{*}\cdot\underline{R}^{T}\cdot\underline{\underline{H}}\end{pmatrix}:\underline{\boldsymbol{B}}^{\beta}\cdot\dot{\boldsymbol{u}}^{\beta}dV + \\ &\int_{V_e} \underline{I}\vec{\nabla}N^{\alpha}\cdot\underline{R}\cdot\underline{\sigma}^{*}\cdot\underline{R}^{T}\cdot\vec{\nabla}N^{\beta}\cdot\dot{\boldsymbol{u}}^{\beta}dV\end{aligned} \tag{2-96}$$

Finally, the stiffness matrix $\underline{K}$, as defined in equation (2-81), becomes:

$$\begin{aligned}\underline{K}^{\alpha\beta} = &\int_{V_e} \underline{\boldsymbol{B}}^{t\alpha}:\begin{pmatrix}(\underline{R}\cdot\underline{\underline{H}}\cdot\underline{R}):\underline{\underline{L}}^{y}:(\underline{R}^{T}\cdot\underline{\underline{H}}\cdot\underline{R}^{T})- \\ \underline{\underline{H}}\cdot\underline{R}\cdot\underline{\sigma}^{*}\cdot\underline{R}^{T}-\underline{R}\cdot\underline{\sigma}^{*}\cdot\underline{R}^{T}\cdot\underline{\underline{H}}\end{pmatrix}:\underline{\boldsymbol{B}}^{\beta}dV + \\ &\int_{V_e} \underline{I}\vec{\nabla}N^{\alpha}\cdot\underline{R}\cdot\underline{\sigma}^{*}\cdot\underline{R}^{T}\cdot\vec{\nabla}N^{\beta}dV\end{aligned} \tag{2-97}$$

2.8 References

[Bathe, 1982]
Bathe K.J., ‘Finite element procedures in engineering analysis’, Prentice Hall, Englewood Cliffs, New York, 1982

[Betten, 1991]
Betten J., ‘Kontinuumsmechanik- Elasto-, Plasto- und Kriechmechanik’, Springer-Verlag, Berlin, 1991

[Huétink, 1986]
Huétink J., ‘On the numerical simulations of thermo-mechanical forming processes’, Ph.D. Thesis, University of Twente, Enschede, 1986

[Huétink, 1999]
Huétink J., D.G. Roddeman, H.J.M. Geijselaers, A.H. van den Boogaard, ‘Mechanics of forming processes’, Report WB.99/TM-4049, University of Twente, Enschede, 1999

[Malvern, 1969]
Malvern M.E., ‘Introduction to the mechanics of a continuous medium’, Prentice Hall, 1969

[Mooi, 1996]
Mooi H.G., ‘Finite element simulations of aluminium extrusion’, Ph.D. Thesis, University of Twente, Enschede, ISBN 90-90099956, 1996

[Rietman, 1999]
Rietman A.D., ‘Numerical analysis of inhomogeneous deformation in plane strain compression’, Ph.D. Thesis, University of Twente, Enschede, ISBN 90-36513626, 1999

[Segerlind, 1984]
Segerlind L.J., ‘Applied finite element analysis’, 2nd edition, J. Wiley & Sons Inc, New York, 1984

[Simo, 1998]
Simo J.C., T.J.R. Hughes, ‘Computational inelasticity’, Springer-Verlag, New York, 1998

[Zienkiewicz, 1991]
Zienkiewicz O.C., R.L. Taylor, ‘The finite element method’, 4th edition, McGraw-Hill Book Company (UK), 1991

3. Mixed elastoplastic / rigid plastic material model for Hill’48 anisotropic material behavior

3.1 Introduction

The plastic deformation of the material is described by constitutive relations which are usually based on rate equations. A yield function defines the stress states at which a material starts to deform plastically. Drucker [Drucker, 1949] postulated that for metal plasticity the direction of the plastic flow rate is perpendicular to the yield surface. The magnitude of the plastic flow rate is determined by a consistency relation to keep the current stress state on the yield surface and this consistency relation equivalently fulfills the Kuhn-Tucker complementary conditions [Simo, 1998].

For use in an incremental procedure the plastic strain rate must be integrated to yield a plastic strain increment. Many of these algorithms are based on an elastic predictor / plastic corrector scheme [Rice, 1971], [Wilkins, 1964]. The direction of the plastic flow can be interpolated between the directions calculated at the start and at the end of a strain increment [Nikishkov, 1993], [Ortiz, 1985]. As mentioned, the magnitude of the plastic flow is determined by a consistency relation, i.e. the stress state remains on the yield surface.

The advantage of these elastoplastic algorithms is that they give an accurate description of the material behavior and that they incorporate elastic effects such as springback. However, elastoplastic algorithms can give rise to numerical instabilities due to the transition from elastic to plastic behavior which is incorporated in these models. When the strain increments are large, the elastic part of the strain can be neglected without a serious loss of accuracy. In that case the plastic strain equals the total strain which is better known as rigid plastic material behavior.

In deep drawing simulations, the rigid plastic material model is widely used because of its fast and numerically robust behavior. The model yields accurate results for large strain increments compared to the elastic limit strain. However, the rigid plastic material model becomes unstable or inaccurate in cases where the strain increments are small, for example in dead metal zones. Another drawback of the rigid plastic approach is that elastic phenomena such as springback cannot be described. Therefore, the use of the elastoplastic material model is favored despite of its drawbacks (potential to numerical instability and high computation time) compared to the rigid plastic material model.

Huétink et al. developed a new integration algorithm for large plastic deformations in combination with Von Mises material behavior [Huétink, 1999]. The algorithm degenerates to the Euler forward elastoplastic material model for small strain increments and to the rigid plastic material model for large strain increments. This new model benefits from the advantages of both the elastoplastic and rigid plastic material model: accuracy and fast convergence over a large range of plastic strain increments.

In this chapter a new integration algorithm is derived for large plastic deformations in combination with the Hill’48 yield criterion [Hill, 1950] similar to the approach of Huétink using Von Mises material behavior. Note that in this chapter stresses and strains are regarded as invariant tensors, as introduced in Chapter 2. The asterisks, denoting the invariant form, will be dropped for convenience.

3.2 Hill’48 planar anisotropic material model

A yield function that can capture orthotropy has been proposed by Hill [Hill, 1950] as an extension of the Von Mises criterion. In its most general form, the Hill’48 yield criterion can be written as:

$$\begin{aligned}\phi = F(\sigma_y-\sigma_z)^2+G(\sigma_z-\sigma_x)^2+H(\sigma_x-\sigma_y)^2+2L{\sigma_{yz}}^2+2M{\sigma_{zx}}^2+2N{\sigma_{xy}}^2\\ -\tfrac{2}{3}(F+G+H){\sigma_y}^2=0\end{aligned} \tag{3-98}$$

where σ_y is the yield stress. The material x-, y- and z-directions coincide with the axes of orthotropy. The parameters F, G, H, L, M and N describe the anisotropy of the material and can be defined as functions of the planar anisotropy parameters R_0, R_{45} and R_{90} [Carleer, 1997].

Introducing the fourth order tensor $\underline{\underline{P}}$ [Borst, 1990], here written as a matrix:

$$\underline{\underline{P}}=\begin{bmatrix} G+H & -H & -G & 0 & 0 & 0\\ -H & F+H & -F & 0 & 0 & 0\\ -G & -F & F+G & 0 & 0 & 0\\ 0 & 0 & 0 & 2N & 0 & 0\\ 0 & 0 & 0 & 0 & 2M & 0\\ 0 & 0 & 0 & 0 & 0 & 2L \end{bmatrix} \quad \text{with} \quad \boldsymbol{\sigma}=\begin{bmatrix}\sigma_x\\ \sigma_y\\ \sigma_z\\ \sigma_{xy}\\ \sigma_{xz}\\ \sigma_{yz}\end{bmatrix} \tag{3-99}$$

the expression for the Hill yield criterion can be simplified to:

$$\phi=\sqrt{\underline{\sigma}^T:\underline{\underline{P}}:\underline{\sigma}}-\sqrt{\tfrac{2}{3}\left(F+G+H\right)}\sigma_y=\sqrt{\underline{\sigma}^T:\underline{\underline{P}}:\underline{\sigma}}-\sqrt{\xi}\sigma_y=0 \tag{3-100}$$

Since the Cauchy stress tensor is symmetric ($\underline{\sigma}=\underline{\sigma}^T$), the superscript ^{T} denoting the transposed form will be dropped for convenience. The derivative of ϕ to $\underline{\sigma}$ is:

$$\frac{\partial\phi}{\partial\underline{\sigma}}=\frac{\underline{\underline{P}}:\underline{\sigma}}{\sqrt{\underline{\sigma}:\underline{\underline{P}}:\underline{\sigma}}} \tag{3-101}$$

The plastic strain rate obeys the associative flow rule according to Drucker:

$$\underline{\dot{\varepsilon}}^p=\dot{\lambda}\frac{\partial\phi}{\partial\underline{\sigma}}=\dot{\lambda}\frac{\underline{\underline{P}}:\underline{\sigma}}{\sqrt{\underline{\sigma}:\underline{\underline{P}}:\underline{\sigma}}}=\frac{\dot{\lambda}}{\sqrt{\xi}\sigma_y}\underline{\underline{P}}:\underline{\sigma} \tag{3-102}$$

The definition of the equivalent plastic strain rate $\dot{\kappa}$ follows from the plastic deformation energy and equations (3-100) and (3-102):

$$\sigma_y\cdot\dot{\kappa}=\underline{\dot{\varepsilon}}^p:\underline{\sigma}=\frac{\sqrt{\xi}\sigma_y}{\dot{\lambda}}\underline{\dot{\varepsilon}}^p:\underline{\underline{P}}^{-1}:\underline{\dot{\varepsilon}}^p=\frac{\xi\sigma_y}{\dot{\kappa}}\underline{\dot{\varepsilon}}^p:\underline{\underline{P}}^{-1}:\underline{\dot{\varepsilon}}^p \qquad \Rightarrow \quad \dot{\kappa}=\sqrt{\xi\underline{\dot{\varepsilon}}^p:\underline{\underline{P}}^{-1}:\underline{\dot{\varepsilon}}^p} \tag{3-103}$$

Note that the matrix $\underline{\underline{P}}$, given in the form of equation (3-99), is singular and thus not invertible since the Hill’48 yield criterion is insensitive to hydrostatic pressure. Consequently, the equivalent plastic strain rate cannot be determined. This problem can be solved by allowing a small amount of compressibility [Koenis, 1994]. However, in simulations of sheet metal forming, a plane stress is generally assumed ($\sigma_z=\sigma_{xz}=\sigma_{yz}=0$). Applying the plane stress state, the matrix $\underline{\underline{P}}$ degenerates to a 3*3 matrix which is invertible, without the necessity to allow compressibility.

The relation between the equivalent plastic strain rate $\dot{\kappa}$ and the plastic multiplier $\dot{\lambda}$ is also derived from the plastic deformation energy and equations (3-100) and (3-102):

$$\sigma_y \cdot \dot{\kappa} = \underline{\sigma}:\dot{\underline{\varepsilon}}^p = \frac{\dot{\lambda}}{\sqrt{\xi}\sigma_y}\underline{\sigma}:\underline{\underline{P}}:\underline{\sigma} = \frac{\dot{\lambda}}{\sqrt{\xi}\sigma_y}\xi\sigma_y^2 = \dot{\lambda}\sqrt{\xi}\sigma_y \qquad \Rightarrow \qquad \dot{\kappa} = \sqrt{\xi}\dot{\lambda} \tag{3-104}$$

The hardening parameter f can be determined for isotropic hardening, starting with equations (2-55) and (2-56). In this case the hardening tensor $\underline{\beta}$ is defined as a second order unit tensor with a magnitude of the equivalent plastic strain rate $\dot{\kappa}$ [Vreede, 1992].

$$f\dot{\lambda} = \frac{\partial\phi}{\partial\underline{\beta}}:\dot{\underline{\beta}} = \frac{\partial\phi}{\partial\underline{\beta}}:\underline{I}\dot{\kappa} = \frac{\partial\phi}{\partial\kappa}\frac{\partial\kappa}{\partial\underline{\beta}}:\underline{I}\dot{\kappa} = \frac{\partial\phi}{\partial\kappa}\frac{\partial(\frac{1}{3}tr\underline{\beta})}{\partial\underline{\beta}}:\underline{I}\dot{\kappa} = \frac{\partial\phi}{\partial\kappa}\frac{1}{3}\underline{I}:\underline{I}\dot{\kappa} = \frac{\partial\phi}{\partial\kappa}\dot{\kappa} \tag{3-105}$$

With the hardening modulus $h = \frac{d\sigma_y}{d\kappa}$ one can define the hardening parameter f as:

$$f = \frac{\partial\phi}{\partial\kappa}\frac{\dot{\kappa}}{\dot{\lambda}} = \frac{\partial\phi}{\partial\kappa}\sqrt{\xi} = \frac{\partial(\sqrt{\underline{\sigma}:\underline{\underline{P}}:\underline{\sigma}} - \sqrt{\xi}\sigma_y)}{\partial\kappa}\sqrt{\xi} = -\xi \cdot h \tag{3-106}$$

3.3 Time integration of stress-strain relation

The relations from the previous section are in rate formulation and hence not readily applicable in a finite element analysis. To solve these equations numerically they have to be discretized in time. The assumptions used in the numerical integration algorithm are decisive for the accuracy and the stability of the method [Ortiz, 1985]. In rate independent plasticity the time discretization can be seen as a chronology of events rather than its physical equivalent. In a finite element context the loading history is then divided into a number of load steps or displacement increments. The resulting equations are solved in an iterative way.

For elastoplastic material behavior, the elastic strain tensor is related to the Cauchy stress tensor via the elasticity tensor $\underline{\underline{E}}$. When the total strain is decomposed into a plastic part and an elastic part, the elastic stress-strain relation in incremental form yields:

$$\Delta\underline{\sigma} = \underline{\underline{E}}:(\Delta\underline{\varepsilon} - \Delta\underline{\varepsilon}^p) \tag{3-107}$$

The plastic strain rate is integrated by a generalized trapezoidal rule, yielding the following expression for the incremental plastic strain $\Delta\underline{\varepsilon}^p$:

$$\Delta\underline{\varepsilon}^p = \int_{t_0}^{t_1}\dot{\underline{\varepsilon}}^p dt \approx (\underline{\underline{H}} - \underline{\underline{\alpha}}):\dot{\underline{\varepsilon}}_0^p\Delta t + \underline{\underline{\alpha}}:\dot{\underline{\varepsilon}}_1^p\Delta t \tag{3-108}$$

where t_0 and t_1 bound a time increment and $\underline{\underline{H}}$ is the fourth order unit tensor. The direction of the incremental plastic strain is determined by interpolating the plastic strain rate directions at the start and end of the time increment with the interpolation tensor $\underline{\underline{\alpha}}$. The plastic strain rate at time $t = t_0$ and $t = t_1$ is, see equation (3-102):

$$t = t_0: \qquad \dot{\underline{\varepsilon}}_0^p = \frac{\dot{\lambda}_0}{\sqrt{\xi}\sigma_{y,0}} \underline{\underline{P}}:\underline{\sigma}_0 \tag{3-109}$$

$$t = t_1: \qquad \dot{\underline{\varepsilon}}_1^p = \frac{\dot{\lambda}_1}{\sqrt{\xi}\sigma_{y,1}} \underline{\underline{P}}:\underline{\sigma}_1$$

Suppose $\dot{\lambda}_0 / \sigma_{y,0} = \dot{\lambda}_1 / \sigma_{y,1}$ to simplify the integration. Physically this means that a linear relation between the stress and strain rate is assumed within the time increment. Then, with $\dot{\kappa} = \sqrt{\xi}\dot{\lambda}$, the incremental plastic strain becomes:

$$\Delta\underline{\varepsilon}^p = \frac{\Delta\kappa}{\xi\sigma_y}\left((\underline{\underline{H}} - \underline{\underline{\alpha}}):\underline{\underline{P}}:\underline{\sigma}_0 + \underline{\underline{\alpha}}:\underline{\underline{P}}:\underline{\sigma}_1\right) \tag{3-110}$$

Substitution of equation (3-110) in (3-107) yields the expression for the stress state:

$$\begin{aligned}
\underline{\sigma}_1 &= \underline{\sigma}_0 + \underline{\underline{E}}:\left(\Delta\underline{\varepsilon} - \frac{\Delta\kappa}{\xi\sigma_y}\left((\underline{\underline{H}} - \underline{\underline{\alpha}}):\underline{\underline{P}}:\underline{\sigma}_0 + \underline{\underline{\alpha}}:\underline{\underline{P}}:\underline{\sigma}_1\right)\right) \\
&= \left(\underline{\underline{H}} - \frac{\Delta\kappa}{\xi\sigma_y}\underline{\underline{E}}:(\underline{\underline{H}} - \underline{\underline{\alpha}}):\underline{\underline{P}}\right):\underline{\sigma}_0 + \underline{\underline{E}}:\Delta\underline{\varepsilon} - \frac{\Delta\kappa}{\xi\sigma_y}\underline{\underline{E}}:\underline{\underline{\alpha}}:\underline{\underline{P}}:\underline{\sigma}_1
\end{aligned} \tag{3-111}$$

or in explicit form:

$$\left(\underline{\underline{H}} + \frac{\Delta\kappa}{\xi\sigma_y}\underline{\underline{E}}:\underline{\underline{\alpha}}:\underline{\underline{P}}\right):\underline{\sigma}_1 = \left(\underline{\underline{H}} - \frac{\Delta\kappa}{\xi\sigma_y}\underline{\underline{E}}:(\underline{\underline{H}} - \underline{\underline{\alpha}}):\underline{\underline{P}}\right):\underline{\sigma}_0 + \underline{\underline{E}}:\Delta\underline{\varepsilon} \tag{3-112}$$

Several well known integration techniques are related to a fixed value of the interpolation tensor $\underline{\underline{\alpha}}$. For convenience, the interpolation tensor $\underline{\underline{\alpha}}$ will be defined as $\beta\underline{\underline{H}}$ in this part of the section. Taking $\beta = 0$ will lead to the *Euler forward* method which is based on values at the start of the step only. This algorithm is an explicit algorithm since the strain or stress of the current step has no influence on the integration algorithm. Taking $\beta = 1$ will lead to the *Euler backward* method which is based only on values at the end of the step and thus is a fully implicit method. In the case of associated plasticity the Euler backward method degenerates to *closest point projection*. The *generalized trapezoidal rule* ($0 < \beta < 1$) is unconditionally stable for $\beta > ½$ in the case of the Von Mises yield criterion; for the Hill yield criterion it is unconditionally stable for $\beta > \beta_{\min}$ where $\beta_{\min}$ depends on the maximum curvature of the yield surface [Atzema, 1994]. The generalized trapezoidal rule degenerates to the *generalized midpoint rule* in case of Von Mises yielding. Also other return mapping algorithms are available in where the elastic predictor is returned iteratively to the yield surface, such as the well known *tangent cutting plane* [Simo, 1985a], [Ortiz, 1986], [Hughes, 1998].

For rigid plastic material behavior, also referred to as the flow formulation, the elastic deformations are totally ignored, i.e. the calculated strain increment equals the plastic strain increment. Hence the total strain rate can be expressed as, see equation (3-102):

$$\dot{\underline{\varepsilon}} = \frac{\dot{\lambda}}{\sqrt{\xi}\sigma_y}\underline{\underline{P}}:\underline{\sigma} \tag{3-113}$$

Rearranging the above equation and writing it in incremental form yields an expression for the rigid plastic stress state:

$$\underline{\sigma}_1 = \frac{\sqrt{\xi}\sigma_y}{\dot{\lambda}} \underline{\underline{P}}^{-1} : \underline{\dot{\varepsilon}} = \frac{\xi \sigma_y}{\Delta\kappa} \underline{\underline{P}}^{-1} : \Delta\underline{\varepsilon} \tag{3-114}$$

3.4 Stress update algorithm

Within a numerical time increment, the total strain is only determined at the start and at the end of the time increment. The stress at the end of the time increment must be calculated. The task of the stress integration is only to calculate the stress for a prescribed strain increment. If the calculated stress does not match the weighted equilibrium at a global level, a new strain increment has to be calculated.

The new stress state $\underline{\sigma}_1$ is determined using an elastic predictor / plastic corrector method. The basic idea is to treat the total strain increment as elastic, calculate the corresponding stress, and then project this calculated stress onto the yield surface. The elastic predictor defines a trial stress state $\underline{\sigma}_t$:

$$\underline{\sigma}_t = \underline{\sigma}_0 + \underline{\underline{E}} : \Delta\underline{\varepsilon} \tag{3-115}$$

where $\underline{\sigma}_0$ is the stress state at time t_0.

If the trial stress state lies outside the yield surface then $\phi(\underline{\sigma}_t,\kappa) > 0$. Since the yield function can never be larger than 0, a plastic corrector has to be used to determine a new stress state $\underline{\sigma}_1$ which lies on the yield surface ($\phi(\underline{\sigma}_1,\kappa) = 0$). The new stress state $\underline{\sigma}_1$ can be determined by writing equation (3-112) as a function of the trial stress state:

$$\left(\underline{\underline{H}} + \frac{\Delta\kappa}{\xi\sigma_y} \underline{\underline{E}} : \underline{\underline{\alpha}} : \underline{\underline{P}} \right) : \underline{\sigma}_1 = \underline{\sigma}_t - \frac{\Delta\kappa}{\xi\sigma_y} \underline{\underline{E}} : (\underline{\underline{H}} - \underline{\underline{\alpha}}) : \underline{\underline{P}} : \underline{\sigma}_0 \tag{3-116}$$

Define the fourth order tensor $\underline{\underline{A}}$:

$$\underline{\underline{A}} = \left(\underline{\underline{H}} + \frac{\Delta\kappa}{\xi\sigma_y} \underline{\underline{E}} : \underline{\underline{\alpha}} : \underline{\underline{P}} \right) \tag{3-117}$$

Note that the tensor $\underline{\underline{A}}$ is symmetric for Hill'48 anisotropic yielding ($A_{ijkl} = A_{klij}$), which means that the transposed form of $\underline{\underline{A}}$ is identical to $\underline{\underline{A}}$. Hence, equation (3-111) can be simplified to:

$$\underline{\sigma}_1 = \underline{\underline{A}}^{-1} : \underline{\sigma}_t - \frac{\Delta\kappa}{\xi\sigma_y} \underline{\underline{A}}^{-1} : \underline{\underline{E}} : (\underline{\underline{H}} - \underline{\underline{\alpha}}) : \underline{\underline{P}} : \underline{\sigma}_0 \tag{3-118}$$

The equivalent plastic strain increment $\Delta\kappa$ must be known in order to calculate the new stress state $\underline{\sigma}_1$. The value of $\Delta\kappa$ is derived from the consistency relation $\phi(\underline{\sigma},\kappa) = 0$ as follows. The yield function depends on $\Delta\kappa$:

$$\begin{aligned} \phi(\Delta\kappa) &= \left(\underline{\sigma}_1 : P : \underline{\sigma}_1 \right)^{\frac{1}{2}} - \sqrt{\xi}\sigma_y \\ &= \left(\left(\underline{\sigma}_t : \underline{\underline{A}}^{-1} - \frac{\Delta\kappa}{\xi\sigma_y} \underline{\sigma}_0 : \underline{\underline{P}} : (\underline{\underline{H}} - \underline{\underline{\alpha}}) : \underline{\underline{E}} : \underline{\underline{A}}^{-1} \right) : \underline{\underline{P}} : \left(\underline{\underline{A}}^{-1} : \underline{\sigma}_t - \frac{\Delta\kappa}{\xi\sigma_y} \underline{\underline{A}}^{-1} : \underline{\underline{E}} : (\underline{\underline{H}} - \underline{\underline{\alpha}}) : \underline{\underline{P}} : \underline{\sigma}_0 \right) \right)^{\frac{1}{2}} \\ &\quad - \sqrt{\xi}\sigma_y \end{aligned} \tag{3-119}$$

Here σ_y and the tensor $\underline{\underline{A}}$ are functions of the equivalent plastic strain increment $\Delta\kappa$. Therefore equation (3-119) is a non-linear relation that must be solved by an iterative procedure, e.g. by a Newton-Raphson method:

$$\Delta\kappa_{k+1} = \Delta\kappa_k - \left(\frac{d\phi}{d\kappa}\right)^{-1} \phi(\Delta\kappa) \tag{3-120}$$

Assume that the fourth order tensor $\underline{\underline{\alpha}}$ depends on $\Delta\kappa$:

$$\frac{d\underline{\underline{\alpha}}}{d\kappa} = \underline{\underline{\psi}} \tag{3-121}$$

then the general expression for $\left(\frac{d\phi}{d\kappa}\right)$ yields, with the hardening modulus $h = \frac{d\sigma_y}{d\kappa}$:

$$\begin{aligned}\left(\frac{d\phi}{d\kappa}\right) = {} & \frac{1}{\left(\phi(\Delta\kappa) + \sqrt{\xi}\sigma_y\right)}\left(\underline{\sigma}_t : \underline{\underline{A}}^{-1} - \frac{\Delta\kappa}{\xi\sigma_y}\underline{\sigma}_0 : \underline{\underline{P}} : (\underline{\underline{H}} - \underline{\underline{\alpha}}) : \underline{\underline{E}} : \underline{\underline{A}}^{-1}\right) : \underline{\underline{P}} : \\ & \left(\frac{d\underline{\underline{A}}^{-1}}{d\kappa} : \underline{\sigma}_t - \left(\begin{array}{l} \frac{1}{\xi\sigma_y}\left(1 - \frac{h\Delta\kappa}{\sigma_y}\right)\underline{\underline{A}}^{-1} : \underline{\underline{E}} : (\underline{\underline{H}} - \underline{\underline{\alpha}}) : \underline{\underline{P}} + \frac{\Delta\kappa}{\xi\sigma_y}\frac{d\underline{\underline{A}}^{-1}}{d\kappa} : \underline{\underline{E}} : (\underline{\underline{H}} - \underline{\underline{\alpha}}) : \underline{\underline{P}} - \\ \frac{\Delta\kappa}{\xi\sigma_y}\underline{\underline{A}}^{-1} : \underline{\underline{E}} : \underline{\underline{\psi}} : \underline{\underline{P}} \end{array} \right) : \underline{\sigma}_0 \right) \\ & - \sqrt{\xi}h \end{aligned} \tag{3-122}$$

where:

$$\frac{d\underline{\underline{A}}^{-1}}{d\kappa} = -\underline{\underline{A}}^{-2} : \left(\frac{1}{\xi\sigma_y}\underline{\underline{E}} : \underline{\underline{\alpha}} : \underline{\underline{P}} - \frac{h\Delta\kappa}{\xi\sigma_y^2}\underline{\underline{E}} : \underline{\underline{\alpha}} : \underline{\underline{P}} + \frac{\Delta\kappa}{\xi\sigma_y}\underline{\underline{E}} : \underline{\underline{\psi}} : \underline{\underline{P}} \right) \tag{3-123}$$

Now, one is able to iteratively determine the incremental equivalent plastic strain $\Delta\kappa$:

```
$\Delta\kappa_0 = 0$   ;   $k = 0$
while ($||\phi(\Delta\kappa_k)|| > error$) do
    $k := k+1$
    determine $\left(\frac{d\phi}{d\kappa}\right)$
    $\Delta\kappa_{k+1} = \Delta\kappa_k - \left(\frac{d\phi}{d\kappa}\right)^{-1} \phi(\Delta\kappa)$
end while
```

(3-124)

3.4.1 Example: Euler backward stress update

For Euler backward integration, the interpolation tensor $\underline{\underline{\alpha}}$ equals the unit tensor. Subsequently the plastic strain tensor can be written as, see equation (3-108):

$$\Delta\underline{\varepsilon}^{p} = \int_{t_0}^{t_1} \underline{\dot{\varepsilon}}^{p}\, dt = \underline{\dot{\varepsilon}}_1^{p}\,\Delta t \tag{3-125}$$

The stress update depends on the state at the end of the step only, and the direction of the plastic strain rate is perpendicular to the yield surface at the end of the step. The new stress state is written as, see equation (3-118):

$$\underline{\sigma}_1 = \underline{\underline{A}}^{-1}\!:\underline{\sigma}_t \tag{3-126}$$

where:

$$\underline{\underline{A}} = \left(\underline{\underline{H}} + \frac{\Delta\kappa}{\xi\sigma_y}\underline{\underline{E}}:\underline{\underline{P}} \right) \tag{3-127}$$

Since $\underline{\underline{\alpha}} = \underline{\underline{H}}$, one can write:

$$\underline{\underline{\psi}} = \underline{\underline{0}} \tag{3-128}$$

Thus, the expression for the derivative of the fourth tensor $\underline{\underline{A}}$ (equation (3-123)) yields:

$$\frac{d\underline{\underline{A}}^{-1}}{d\Delta\kappa} = -\frac{1}{\xi\sigma_y}\left(1 - \frac{h\Delta\kappa}{\sigma_y}\right)\underline{\underline{A}}^{-2}\!:\underline{\underline{E}}:\underline{\underline{P}} \tag{3-129}$$

which gives, in combination with equation (3-122), the expression for $\left(d\phi/d\kappa\right)$ in the case of Euler backward integration:

$$\left(\frac{d\phi}{d\kappa}\right) = \frac{-1}{\xi\sigma_y}\left(1 - \frac{h(\Delta\kappa)^2}{\sigma_y}\right)\frac{1}{\left(\phi(\Delta\kappa) + \sqrt{\xi}\sigma_y\right)}\underline{\sigma}_t:\underline{\underline{A}}^{-1}\!:\underline{\underline{P}}:\underline{\underline{A}}^{-2}\!:\underline{\underline{E}}:\underline{\underline{P}}:\underline{\sigma}_t - \sqrt{\xi}h \tag{3-130}$$

3.5 Consistent stiffness tensor

To preserve fast convergence of the global weak equilibrium, the stiffness tensor must be set up consistent with the integration algorithm [Simo, 1985b]. Hence, this stiffness tensor used in the predictor step should be consistent with the incremental constitutive relations, not the continuum constitutive relations [Atzema, 1992]. In this section the consistent stiffness tensor is derived for both the elastoplastic material behavior and the rigid plastic material behavior.

3.5.1 Elastoplastic consistent stiffness tensor

To obtain the consistent stiffness tensor for elastoplastic material behavior, equation (3-112) must be written in differential form:

$$\underline{\underline{A}}:d\underline{\sigma}_1 + d\underline{\underline{A}}:\underline{\sigma}_1 = -\frac{1}{\xi\sigma_y}\left(1 - \frac{h\Delta\kappa}{\sigma_y}\right)\underline{\underline{E}}:(\underline{\underline{H}} - \underline{\underline{\alpha}}):\underline{\underline{P}}:\underline{\sigma}_0 d\kappa + \frac{\Delta\kappa}{\xi\sigma_y}\underline{\underline{E}}:\underline{\underline{\psi}}:\underline{\underline{P}}:\underline{\sigma}_0 d\kappa + \underline{\underline{E}}:d\underline{\varepsilon} \tag{3-131}$$

in which $\underline{\underline{\psi}} = \frac{d\underline{\underline{\alpha}}}{d\kappa}$ is a fourth order tensor yet to be specified and $d\underline{\underline{A}}$ is given by, see equation (3-117):

$$d\underline{\underline{A}} = \left(\frac{1}{\xi\sigma_y}\left(1 - \frac{h\Delta\kappa}{\sigma_y}\right)\underline{\underline{E}}:\underline{\underline{\alpha}}:\underline{\underline{P}} + \frac{\Delta\kappa}{\xi\sigma_y}\underline{\underline{E}}:\underline{\underline{\psi}}:\underline{\underline{P}} \right) d\kappa \qquad \text{(3-132)}$$

Combining equations (3-131) and (3-132) gives:

$$\begin{aligned} d\underline{\sigma}_1 &= \underline{\underline{A}}^{-1}:\left(\underline{\underline{E}}:d\underline{\varepsilon} - d\underline{\underline{A}}:\underline{\sigma}_1 - \left(\frac{1}{\xi\sigma_y}\left(1-\frac{h\Delta\kappa}{\sigma_y}\right)\underline{\underline{E}}:(\underline{\underline{H}}-\underline{\underline{\alpha}}):\underline{\underline{P}}:\underline{\sigma}_0 - \frac{\Delta\kappa}{\xi\sigma_y}\underline{\underline{E}}:\underline{\underline{\psi}}:\underline{\underline{P}}:\underline{\sigma}_0 \right) d\kappa \right) \qquad \text{(3-133)} \\ &= \underline{\underline{A}}^{-1}:\left(\underline{\underline{E}}:d\underline{\varepsilon} - \left(\begin{matrix} \left(\frac{1}{\xi\sigma_y}\left(1-\frac{h\Delta\kappa}{\sigma_y}\right)\underline{\underline{E}}:\underline{\underline{\alpha}}:\underline{\underline{P}} + \frac{\Delta\kappa}{\xi\sigma_y}\underline{\underline{E}}:\underline{\underline{\psi}}:\underline{\underline{P}} \right):\underline{\sigma}_1 + \\ \left(\frac{1}{\xi\sigma_y}\left(1-\frac{h\Delta\kappa}{\sigma_y}\right)\underline{\underline{E}}:(\underline{\underline{H}}-\underline{\underline{\alpha}}):\underline{\underline{P}} - \frac{\Delta\kappa}{\xi\sigma_y}\underline{\underline{E}}:\underline{\underline{\psi}}:\underline{\underline{P}} \right):\underline{\sigma}_0 \end{matrix} \right) d\kappa \right) \\ &= \underline{\underline{A}}^{-1}:\left(\underline{\underline{E}}:d\underline{\varepsilon} - \underline{U}d\kappa \right) \end{aligned}$$

with the second order tensor $\underline{U}$:

$$\begin{aligned} \underline{U} = {} & \left(\frac{1}{\xi\sigma_y}\left(1-\frac{h\Delta\kappa}{\sigma_y}\right)\underline{\underline{E}}:\underline{\underline{\alpha}}:\underline{\underline{P}} + \frac{\Delta\kappa}{\xi\sigma_y}\underline{\underline{E}}:\underline{\underline{\psi}}:\underline{\underline{P}} \right):\underline{\sigma}_1 + \qquad \text{(3-134)} \\ & \left(\frac{1}{\xi\sigma_y}\left(1-\frac{h\Delta\kappa}{\sigma_y}\right)\underline{\underline{E}}:(\underline{\underline{H}}-\underline{\underline{\alpha}}):\underline{\underline{P}} - \frac{\Delta\kappa}{\xi\sigma_y}\underline{\underline{E}}:\underline{\underline{\psi}}:\underline{\underline{P}} \right):\underline{\sigma}_0 \end{aligned}$$

The expression for $d\kappa$ as a function of $d\underline{\varepsilon}$ is defined by the consistency condition:

$$\begin{aligned} & d\phi = \tfrac{1}{2}(\underline{\sigma}_1:\underline{\underline{P}}:\underline{\sigma}_1)^{-\frac{1}{2}}2\underline{\sigma}_1:\underline{\underline{P}}:d\underline{\sigma}_1 - \sqrt{\xi}d\sigma_y = \frac{1}{\sqrt{\xi}\sigma_y}\underline{\sigma}_1:\underline{\underline{P}}:d\underline{\sigma}_1 - h\sqrt{\xi}d\kappa = 0 \Rightarrow \qquad \text{(3-135)} \\ & \underline{\sigma}_1:\underline{\underline{P}}:d\underline{\sigma}_1 = h\xi\sigma_y d\kappa \end{aligned}$$

This gives, together with equation (3-133), an expression for $d\kappa$:

$$d\kappa = \frac{\underline{\sigma}_1:\underline{\underline{P}}:\underline{\underline{A}}^{-1}:\underline{\underline{E}}}{h\xi\sigma_y + \underline{\sigma}_1:\underline{\underline{P}}:\underline{\underline{A}}^{-1}:\underline{U}}:d\underline{\varepsilon} \qquad \text{(3-136)}$$

Finally, substituting equation (3-136) in equation (3-133) yields the consistent stiffness tensor for elastoplastic material behavior:

$$d\underline{\sigma}_1 = \left(\underline{\underline{A}}^{-1}:\underline{\underline{E}} - \frac{\left(\underline{\underline{A}}^{-1}:\underline{U}\right)\left(\underline{\sigma}_1:\underline{\underline{P}}:\underline{\underline{A}}^{-1}:\underline{\underline{E}}\right)}{h\xi\sigma_y + \underline{\sigma}_1:\underline{\underline{P}}:\underline{\underline{A}}^{-1}:\underline{U}} \right):d\underline{\varepsilon} \qquad \text{(3-137)}$$

3.5.1.1 Example: consistent stiffness tensor for Euler backward integration

As mentioned, the interpolation tensor $\underline{\alpha}$ equals the unit tensor for Euler backward integration. Hence, with equation (3-128) the second order tensor $\underline{U}$ holds, see equation (3-134):

$$\underline{U} = \frac{1}{\xi\sigma_y}\left(1-\frac{h\Delta\kappa}{\sigma_y}\right)\underline{\underline{E}}:\underline{\underline{P}}:\underline{\sigma}_1 \tag{3-138}$$

yielding the consistent stiffness tensor for Euler backward integration:

$$d\underline{\sigma}_1 = \left(\underline{\underline{A}}^{-1}:\underline{\underline{E}} - \frac{\left(\underline{\underline{A}}^{-1}:\underline{\underline{E}}:\underline{\underline{P}}:\underline{\sigma}_1\right)\left(\underline{\sigma}_1:\underline{\underline{P}}:\underline{\underline{A}}^{-1}:\underline{\underline{E}}\right)}{\dfrac{h\xi^2\sigma_y{}^3}{(\sigma_y - h\Delta\kappa)} + \underline{\sigma}_1:\underline{\underline{P}}:\underline{\underline{A}}^{-1}:\underline{\underline{E}}:\underline{\underline{P}}:\underline{\sigma}_1}\right):d\underline{\varepsilon} \tag{3-139}$$

Note that equation (3-139) differs from the stiffness tensor based on the continuum relations. Only for $\Delta\kappa = 0$ are both tensors equal.

3.5.2 Rigid plastic consistent stiffness tensor

In order to obtain the consistent stiffness tensor for rigid plastic material behavior, equation (3-114) must be written in differential form:

$$d\underline{\sigma}_1 = \frac{\xi\sigma_y}{\Delta\kappa}\underline{\underline{P}}^{-1}:d\underline{\varepsilon} + \frac{\xi}{\Delta\kappa}\underline{\underline{P}}^{-1}:\Delta\underline{\varepsilon}d\sigma_y - \frac{\xi\sigma_y}{(\Delta\kappa)^2}\underline{\underline{P}}^{-1}:\Delta\underline{\varepsilon}d\kappa \tag{3-140}$$

Using the hardening modulus *h* one can write:

$$d\underline{\sigma}_1 = \frac{\xi\sigma_y}{\Delta\kappa}\underline{\underline{P}}^{-1}:d\underline{\varepsilon} + \frac{\xi}{\Delta\kappa}\underline{\underline{P}}^{-1}:\Delta\underline{\varepsilon}\left(h-\frac{\sigma_y}{\Delta\kappa}\right)d\kappa \tag{3-141}$$

Determine an expression for $d\kappa$ as a function of $d\underline{\varepsilon}$:

$$\begin{gathered}\Delta\kappa = \dot{\kappa}\Delta t = \sqrt{\xi\dot{\underline{\varepsilon}}:\underline{\underline{P}}^{-1}:\dot{\underline{\varepsilon}}}\Delta t = \sqrt{\xi\Delta\underline{\varepsilon}:\underline{\underline{P}}^{-1}:\Delta\underline{\varepsilon}} \Rightarrow \\ d\kappa = d\Delta\kappa = \tfrac{1}{2}\left(\xi\Delta\underline{\varepsilon}:\underline{\underline{P}}^{-1}:\Delta\underline{\varepsilon}\right)^{-\frac{1}{2}}2\xi\Delta\underline{\varepsilon}:\underline{\underline{P}}^{-1}:d\underline{\varepsilon} = \frac{\xi}{\Delta\kappa}\Delta\underline{\varepsilon}:\underline{\underline{P}}^{-1}:d\underline{\varepsilon}\end{gathered} \tag{3-142}$$

Combining equations (3-141) and (3-142) gives:

$$d\underline{\sigma}_1 = \left(\frac{\xi\sigma_y}{\Delta\kappa}\underline{\underline{P}}^{-1} + \frac{\xi^2}{(\Delta\kappa)^2}\left(h-\frac{\sigma_y}{\Delta\kappa}\right)\left(\underline{\underline{P}}^{-1}:\Delta\underline{\varepsilon}\right)\left(\Delta\underline{\varepsilon}:\underline{\underline{P}}^{-1}\right)\right):d\underline{\varepsilon} \tag{3-143}$$

and with equation (3-114) the consistent stiffness tensor for rigid plastic material behavior is found:

$$d\underline{\sigma}_1 = \left(\frac{\xi\sigma_y}{\Delta\kappa}\underline{\underline{P}}^{-1} + \left(h-\frac{\sigma_y}{\Delta\kappa}\right)\frac{\underline{\sigma}_1\underline{\sigma}_1}{\sigma_y^2}\right):d\underline{\varepsilon} \tag{3-144}$$

3.6 Mixed elastoplastic / rigid plastic material model

The purpose of the mixed elastoplastic / rigid plastic material model is to combine the accuracy of the elastoplastic material model and the robustness of the rigid plastic material model over a large range of strain increments. The starting point of the mixed material model is equation (3-112). The value of the interpolation tensor $\underline{\underline{\alpha}}$ is not fixed beforehand, but depends on the equivalent plastic strain increment $\Delta\kappa$ [Huétink, 1999], [Meinders, 1999]. It is expected that for large strain increments the conditions at the start of the incremental step do not affect the calculated stress state at the end of the step significantly. Therefore, in the mixed material model, it is demanded that the influence of the initial stress $\underline{\sigma}_0$ vanish for large strain increments:

$$\lim_{\Delta\kappa\to\infty}\left(\underline{\underline{H}}-\frac{\Delta\kappa}{\xi\sigma_y}\underline{\underline{E}}:(\underline{\underline{H}}-\underline{\underline{\alpha}}):\underline{\underline{P}}\right)=\underline{\underline{0}} \tag{3-145}$$

which gives a definition for the interpolation tensor $\underline{\underline{\alpha}}$:

$$\underline{\underline{\alpha}}=\left(\underline{\underline{H}}-\frac{\xi\sigma_y}{\Delta\kappa}\underline{\underline{E}}^{-1}:\underline{\underline{P}}^{-1}\right) \tag{3-146}$$

A reference strain increment κ_{ref} is introduced which corresponds to an elastic stress increment from zero to the current yield stress. The following holds for κ_{ref}:

$$\begin{aligned}\Delta\kappa\le\kappa_{ref}:&\qquad \underline{\underline{\alpha}}=\underline{\underline{0}}\\ \Delta\kappa>\kappa_{ref}:&\qquad \underline{\underline{\alpha}}=\left(\underline{\underline{H}}-\frac{\xi\sigma_y}{\Delta\kappa}\underline{\underline{E}}^{-1}:\underline{\underline{P}}^{-1}\right)\end{aligned} \tag{3-147}$$

Note that for $\Delta\kappa\le\kappa_{ref}$, Euler forward integration is used for the stress update.
Also, the stress state yields, equation (3-112):

$$\underline{\sigma}_1=\left(\underline{\underline{H}}-\frac{\Delta\kappa}{\xi\sigma_y}\underline{\underline{E}}:\underline{\underline{P}}\right):\underline{\sigma}_0+\underline{\underline{E}}:\Delta\underline{\varepsilon} \tag{3-148}$$

For $\Delta\kappa>\kappa_{ref}$ the stress state yields, equation (3-112):

$$\begin{aligned}&\left(\underline{\underline{H}}+\frac{\Delta\kappa}{\xi\sigma_y}\underline{\underline{E}}:\left(\underline{\underline{H}}-\frac{\xi\sigma_y}{\Delta\kappa}\underline{\underline{E}}^{-1}:\underline{\underline{P}}^{-1}\right):\underline{\underline{P}}\right):\underline{\sigma}_1=\\ &\qquad\left(\underline{\underline{H}}-\frac{\Delta\kappa}{\xi\sigma_y}\underline{\underline{E}}:\left(\underline{\underline{H}}-\left(\underline{\underline{H}}-\frac{\xi\sigma_y}{\Delta\kappa}\underline{\underline{E}}^{-1}:\underline{\underline{P}}^{-1}\right)\right):\underline{\underline{P}}\right):\underline{\sigma}_0+\underline{\underline{E}}:\Delta\underline{\varepsilon}\Rightarrow\\ &\left(\underline{\underline{H}}+\frac{\Delta\kappa}{\xi\sigma_y}\left(\underline{\underline{E}}:\underline{\underline{P}}-\frac{\xi\sigma_y}{\Delta\kappa}\underline{\underline{E}}:\underline{\underline{E}}^{-1}:\underline{\underline{P}}^{-1}:\underline{\underline{P}}\right)\right):\underline{\sigma}_1=\left(\underline{\underline{H}}-\frac{\Delta\kappa}{\xi\sigma_y}\frac{\xi\sigma_y}{\Delta\kappa}\underline{\underline{E}}:\underline{\underline{E}}^{-1}:\underline{\underline{P}}^{-1}:\underline{\underline{P}}\right):\underline{\sigma}_0+\underline{\underline{E}}:\Delta\underline{\varepsilon}\Rightarrow\\ &\left(\underline{\underline{H}}+\frac{\Delta\kappa}{\xi\sigma_y}\underline{\underline{E}}:\underline{\underline{P}}-\underline{\underline{H}}\right):\underline{\sigma}_1=\left(\underline{\underline{H}}-\underline{\underline{H}}\right):\underline{\sigma}_0+\underline{\underline{E}}:\Delta\underline{\varepsilon}\Rightarrow\\ &\underline{\sigma}_1=\frac{\xi\sigma_y}{\Delta\kappa}\underline{\underline{P}}^{-1}:\Delta\underline{\varepsilon}\end{aligned} \tag{3-149}$$

Note that for $\Delta\kappa>\kappa_{ref}$ the elastoplastic material description degenerates to the rigid plastic material description, see equation (3-114).

3.6.1 Determination of reference strain increment κ_{ref}

To preserve continuity in the mixed elastoplastic / rigid plastic material model, both equations (3-148) and (3-149) must join each other in case $\Delta\kappa = \kappa_{ref}$. This means that $\underline{\sigma}_0$ in equation (3-148) must vanish for $\Delta\kappa = \kappa_{ref}$, and hence an expression is found for κ_{ref}:

$$\left(\underline{\underline{H}} - \frac{\kappa_{ref}}{\xi\sigma_y}\underline{\underline{E}}:\underline{\underline{P}}\right):\underline{\sigma}_0 = \underline{0} \Rightarrow \kappa_{ref} \overset{?}{=} \xi\sigma_y\underline{\underline{P}}^{-1}:\underline{\underline{E}}^{-1} \tag{3-150}$$

However, the expression found for κ_{ref} is not suitable since it must be a scalar value and in equation (3-150) κ_{ref} is defined as being a fourth order tensor. Therefore, another expression must be found for κ_{ref}. Assume an incremental strain state $\Delta\underline{\varepsilon}_{ref}$ with an accompanying equivalent plastic strain κ_{ref}. In order to obtain an expression for κ_{ref}, a weaker restriction is applied, i.e. it is only demanded that the accompanying stress state for $\Delta\underline{\varepsilon}_{ref}$ must lie on the yield surface, see equation (3-151). This means that the yield stress corresponding with the stress state calculated from the elastoplastic part of the formulation, must equal the yield stress corresponding with the stress state calculated from the rigid plastic part of the formulation. Consequently the directions of both stress states do not have to coincide for the Hill yield criterion, this in contrast to the formulation for Von Mises yielding where it is demanded that both the yield stress and the direction of the stress state coincide for κ_{ref} [Huétink, 1999].

$$\phi = \sqrt{\underline{\sigma}:\underline{\underline{P}}:\underline{\sigma}} - \sqrt{\xi}\sigma_y = \sqrt{\Delta\underline{\varepsilon}_{ref}:\underline{\underline{E}}:\underline{\underline{P}}:\underline{\underline{E}}:\Delta\underline{\varepsilon}_{ref}} - \sqrt{\xi}\sigma_y = 0 \tag{3-151}$$

Substituting equation (3-114) in the above equation gives the scalar expression for κ_{ref}:

$$\phi = \sqrt{\frac{\kappa_{ref}}{\xi\sigma_y}\underline{\sigma}:\underline{\underline{P}}:\underline{\underline{E}}:\underline{\underline{P}}:\underline{\underline{E}}:\frac{\kappa_{ref}}{\xi\sigma_y}\underline{\underline{P}}:\underline{\sigma}} - \sqrt{\xi}\sigma_y = 0 \Rightarrow \kappa_{ref} = \frac{\xi\sqrt{\xi}\sigma_y^2}{\sqrt{\underline{\sigma}:\underline{\underline{P}}:\underline{\underline{E}}:\underline{\underline{P}}:\underline{\underline{E}}:\underline{\underline{P}}:\underline{\sigma}}} \tag{3-152}$$

κ_{ref} can be calculated if $\underline{\sigma}$ is chosen as the stress state at the start of each iteration.

However, κ_{ref} cannot be calculated if the initial stress state equals zero. In this special case, κ_{ref} is calculated assuming Von Mises yielding. In matrix form, the symmetric elasticity tensor $\underline{\underline{E}}$ and the Hill tensor $\underline{\underline{P}}$ are, in the case of Von Mises yielding:

$$\underline{\underline{E}} = \begin{bmatrix} 2G + \frac{2G\nu}{1-2\nu} & \frac{2G\nu}{1-2\nu} & \frac{2G\nu}{1-2\nu} & 0 & 0 & 0 \\ & 2G + \frac{2G\nu}{1-2\nu} & \frac{2G\nu}{1-2\nu} & 0 & 0 & 0 \\ & & 2G + \frac{2G\nu}{1-2\nu} & 0 & 0 & 0 \\ & & & G & 0 & 0 \\ & & & & G & 0 \\ & & & & & G \end{bmatrix} \qquad \underline{\underline{P}} = \begin{bmatrix} 2 & -1 & -1 & 0 & 0 & 0 \\ & 2 & -1 & 0 & 0 & 0 \\ & & 2 & 0 & 0 & 0 \\ & & & 6 & 0 & 0 \\ & & & & 6 & 0 \\ & & & & & 6 \end{bmatrix} \tag{3-153}$$

where G is the shear modulus and ν is Poisson's ratio. After some manipulation, the expression $\underline{\sigma}:\underline{\underline{P}}:\underline{\underline{E}}:\underline{\underline{P}}:\underline{\underline{E}}:\underline{\underline{P}}:\underline{\sigma}$ can be written as:

$$\underline{\sigma}:\underline{\underline{P}}:\underline{\underline{E}}:\underline{\underline{P}}:\underline{\underline{E}}:\underline{\underline{P}}:\underline{\sigma} = 36G^2\begin{pmatrix} \sigma_{xx}\left(2\sigma_{xx}-\sigma_{yy}-\sigma_{zz}\right)+\sigma_{yy}\left(-\sigma_{xx}+2\sigma_{yy}-\sigma_{zz}\right)+ \\ \sigma_{zz}\left(-\sigma_{xx}-\sigma_{yy}+2\sigma_{zz}\right)+6\sigma_{xy}^2+6\sigma_{yz}^2+6\sigma_{xz}^2 \end{pmatrix} \qquad (3\text{-}154)$$

The expression $\underline{\sigma}:\underline{\underline{P}}:\underline{\sigma}$ holds:

$$\underline{\sigma}:\underline{\underline{P}}:\underline{\sigma} = \begin{pmatrix} \sigma_{xx}\left(2\sigma_{xx}-\sigma_{yy}-\sigma_{zz}\right)+\sigma_{yy}\left(-\sigma_{xx}+2\sigma_{yy}-\sigma_{zz}\right)+ \\ \sigma_{zz}\left(-\sigma_{xx}-\sigma_{yy}+2\sigma_{zz}\right)+6\sigma_{xy}^2+6\sigma_{yz}^2+6\sigma_{xz}^2 \end{pmatrix} \qquad (3\text{-}155)$$

Combining equations (3-154), (3-155) and (3-100) yields:

$$\underline{\sigma}:\underline{\underline{P}}:\underline{\underline{E}}:\underline{\underline{P}}:\underline{\underline{E}}:\underline{\underline{P}}:\underline{\sigma} = 36G^2\,\underline{\sigma}:\underline{\underline{P}}:\underline{\sigma} = 36G^2\xi\sigma_y^2 = 72G^2\sigma_y^2 \qquad (3\text{-}156)$$

Now, κ_{ref} can be calculated when the initial stress state is zero:

$$\kappa_{ref} = \frac{\xi\sqrt{\xi\sigma_y^2}}{\sqrt{\underline{\sigma}:\underline{\underline{P}}:\underline{\underline{E}}:\underline{\underline{P}}:\underline{\underline{E}}:\underline{\underline{P}}:\underline{\sigma}}} = \frac{2\sqrt{2\sigma_y^2}}{\sqrt{72G^2\sigma_y^2}} = \frac{\sigma_y}{3G} \qquad (3\text{-}157)$$

3.6.2 Stress update algorithm

The stress update algorithm for the elastoplastic part of the mixed material model is based on Euler forward integration. Subsequently, when the interpolation tensor $\underline{\underline{\alpha}}$ equals zero, the plastic strain can be written as, see equation (3-108):

$$\Delta\underline{\varepsilon}^p = \underline{\dot{\varepsilon}}_0^p\Delta t \qquad (3\text{-}158)$$

The stress state reads:

$$\underline{\sigma}_1 = \left(\underline{\underline{H}} - \frac{\Delta\kappa}{\xi\sigma_y}\underline{\underline{E}}:\underline{\underline{P}}\right):\underline{\sigma}_0 + \underline{\underline{E}}:\Delta\underline{\varepsilon} \qquad (3\text{-}159)$$

The equivalent plastic strain increment $\Delta\kappa$ must be determined to calculate the new stress state. Since $\underline{\underline{\alpha}} = \underline{\underline{0}}$, equations (3-117), (3-121) and (3-123) become:

$$\underline{\underline{A}} = \underline{\underline{H}} \qquad (3\text{-}160)$$

$$\underline{\underline{\psi}} = \underline{\underline{0}}$$

$$\frac{d\underline{\underline{A}}^{-1}}{d\kappa} = \underline{\underline{0}}$$

The expression for $(d\phi / d\kappa)$ yields, in the case of Euler forward integration (see equation (3-122)):

$$\left(\frac{d\phi}{d\kappa}\right) = \frac{-1}{\xi\sigma_y}\left(1-\frac{h\Delta\kappa}{\sigma_y}\right)\frac{1}{\left(\phi(\Delta\kappa)+\sqrt{\xi}\sigma_y\right)}\left(\underline{\sigma}_t - \frac{\Delta\kappa}{\xi\sigma_y}\underline{\sigma}_0:\underline{\underline{P}}:\underline{\underline{E}}\right):P:\left(\underline{\underline{E}}:\underline{\underline{P}}:\underline{\sigma}_0\right)-\sqrt{\xi}h \qquad (3\text{-}161)$$

Hence, the equivalent plastic strain increment $\Delta\kappa$ can be determined according to equation (3-124).

3.6.3 Consistent stiffness tensor

The consistent stiffness tensor has to be derived for both parts of the mixed material model. Firstly, the consistent stiffness tensor for Euler forward integration is derived. Since the interpolation tensor $\underline{\underline{\alpha}} = \underline{\underline{0}}$, equation (3-134) degenerates to:

$$\underline{U} = \frac{1}{\xi\sigma_y}\left(1 - \frac{h\Delta\kappa}{\sigma_y}\right)\underline{\underline{E}}:\underline{\underline{P}}:\underline{\sigma}_0 \tag{3-162}$$

With equations (3-160) and (3-162), the consistent stiffness tensor for Euler forward integration becomes, see equation (3-137):

$$d\underline{\sigma}_1 = \left(\underline{\underline{E}} - \frac{\left(\underline{\underline{E}}:\underline{\underline{P}}:\underline{\sigma}_0\right)\left(\underline{\sigma}_1:\underline{\underline{P}}:\underline{\underline{E}}\right)}{\dfrac{h\xi^2\sigma_y^3}{(\sigma_y - h\Delta\kappa)} + \underline{\sigma}_1:\underline{\underline{P}}:\underline{\underline{E}}:\underline{\underline{P}}:\underline{\sigma}_0}\right):d\underline{\varepsilon} \tag{3-163}$$

Secondly, the consistent stiffness tensor is derived for the rigid plastic part of the mixed material model ($\Delta\kappa > \kappa_{ref}$). With equation (3-147), the fourth order tensors $\underline{\underline{A}}$ (equation (3-117)) and $\underline{\underline{\psi}}$ (equation (3-121)) can be written as:

$$\underline{\underline{A}} = \frac{\Delta\kappa}{\xi\sigma_y}\underline{\underline{E}}:\underline{\underline{P}} \tag{3-164}$$

$$\underline{\underline{\psi}} = \frac{\xi}{\Delta\kappa}\left(\frac{\sigma_y}{\Delta\kappa} - h\right)\underline{\underline{E}}^{-1}:\underline{\underline{P}}^{-1}$$

The second order tensor $\underline{U}$ can be simplified to, see equation (3-134):

$$\begin{aligned}\underline{U} = {} & \left(\frac{1}{\xi\sigma_y}\left(1 - \frac{h\Delta\kappa}{\sigma_y}\right)\underline{\underline{E}}:\left(\underline{\underline{H}} - \frac{\xi\sigma_y}{\Delta\kappa}\underline{\underline{E}}^{-1}:\underline{\underline{P}}^{-1}\right):\underline{\underline{P}} + \frac{\Delta\kappa}{\xi\sigma_y}\underline{\underline{E}}:\left(\frac{\xi}{\Delta\kappa}\left(\frac{\sigma_y}{\Delta\kappa} - h\right)\underline{\underline{E}}^{-1}:\underline{\underline{P}}^{-1}\right):\underline{\underline{P}}\right):\underline{\sigma}_1 + \\ & \left(\frac{1}{\xi\sigma_y}\left(1 - \frac{h\Delta\kappa}{\sigma_y}\right)\underline{\underline{E}}:\left(\frac{\xi\sigma_y}{\Delta\kappa}\underline{\underline{E}}^{-1}:\underline{\underline{P}}^{-1}\right):\underline{\underline{P}} - \frac{\Delta\kappa}{\xi\sigma_y}\underline{\underline{E}}:\left(\frac{\xi}{\Delta\kappa}\left(\frac{\sigma_y}{\Delta\kappa} - h\right)\underline{\underline{E}}^{-1}:\underline{\underline{P}}^{-1}\right):\underline{\underline{P}}\right):\underline{\sigma}_0 \\ = {} & \frac{1}{\xi\sigma_y}\left(1 - \frac{h\Delta\kappa}{\sigma_y}\right)\underline{\underline{E}}:\underline{\underline{P}}:\underline{\sigma}_1\end{aligned} \tag{3-165}$$

With equations (3-164) and (3-165) the consistent stiffness tensor for the second part of the mixed material model can be derived, using equation (3-137):

$$d\underline{\sigma}_1 = \left(\left(\frac{\xi\sigma_y}{\Delta\kappa} \underline{\underline{P}}^{-1} : \underline{\underline{E}}^{-1} \right) : \underline{\underline{E}} - \frac{\left(\left(\frac{\xi\sigma_y}{\Delta\kappa} \underline{\underline{P}}^{-1} : \underline{\underline{E}}^{-1} \right) : \left(\frac{1}{\xi\sigma_y} \left(1 - \frac{h\Delta\kappa}{\sigma_y} \right) \underline{\underline{E}} : \underline{\underline{P}} : \underline{\sigma}_1 \right) \right) \left(\underline{\sigma}_1 : \underline{\underline{P}} : \left(\frac{\xi\sigma_y}{\Delta\kappa} \underline{\underline{P}}^{-1} : \underline{\underline{E}}^{-1} \right) : \underline{\underline{E}} \right)}{h\xi\sigma_y + \underline{\sigma}_1 : \underline{\underline{P}} : \left(\frac{\xi\sigma_y}{\Delta\kappa} \underline{\underline{P}}^{-1} : \underline{\underline{E}}^{-1} \right) : \left(\frac{1}{\xi\sigma_y} \left(1 - \frac{h\Delta\kappa}{\sigma_y} \right) \underline{\underline{E}} : \underline{\underline{P}} : \underline{\sigma}_1 \right)} \right) : d\underline{\varepsilon} \tag{3-166}$$

$$= \left(\frac{\xi\sigma_y}{\Delta\kappa} \underline{\underline{P}}^{-1} - \left(\frac{\sigma_y}{\Delta\kappa} - h \right) \frac{\underline{\sigma}_1 \underline{\sigma}_1}{\sigma_y^2} \right) : d\underline{\varepsilon}$$

Comparing this consistent stiffness tensor with equation (3-144) it is obvious that the second part of the mixed material model equals the rigid plastic material model.

3.7 Degenerated case: initial condition is elastic

The formulation for the mixed elastoplastic / rigid plastic material model as given in Section 3.6 applies only when the initial stress state is on the yield surface. When the stress state is not a part of the yield surface, the mixed material model must be modified in order to account for these situations. A distinction is made between two situations:

1. The stress state $\underline{\sigma}_0$ is elastic; the final stress state $\underline{\sigma}_n$ stays elastic
2. The stress state $\underline{\sigma}_0$ is elastic; the final stress state $\underline{\sigma}_n$ becomes plastic

In the first situation the stress state at the end of the step stays elastic, the consistent stiffness tensor equals the elastic stiffness tensor and the final stress state $\underline{\sigma}_n$ equals the trial stress state $\underline{\sigma}_t$. The second situation requires a more complex treatment. In the case of an initial elastic situation and a final plastic situation, the intersection point with the yield surface has to be calculated first. The algorithms presented in Section 3.6 will act on the remaining strain increment outside the yield surface. In this section two different ways to map the initial elastic stress state onto the yield surface are treated, both illustrated in Figure 3-6.

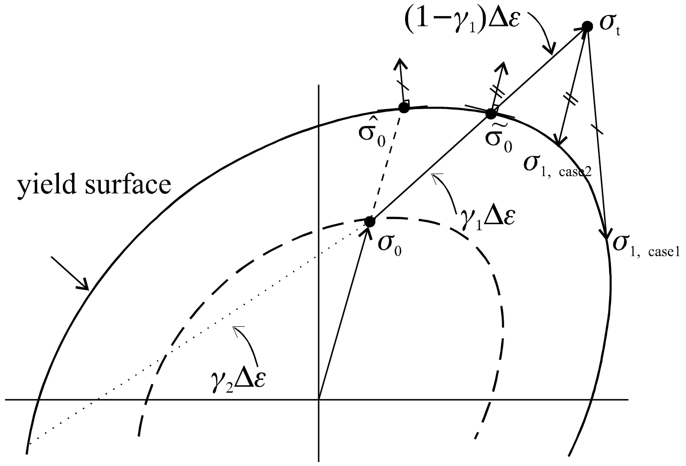

Figure 3-6. Initial elastic condition

In the first case, represented by $\hat{\underline{\sigma}}_0$, the initial stress state $\underline{\sigma}_0$ is scaled to the yield surface while keeping the same direction. In the second case, represented by $\tilde{\underline{\sigma}}_0$, the initial stress state $\underline{\sigma}_0$ is mapped onto the yield surface in the direction of the elastically predicted stress increment. The $\underline{\tilde{\sigma}}_0$ -method is favored to determine the final stress state $\underline{\sigma}_1$ since it is expected to represent more closely the direction of the plastic strain at the end of the step, see equation (3-167).

$$\underline{\sigma}_1 = \underline{\sigma}_t - \frac{\Delta\kappa}{\xi\sigma_y}\underline{\underline{E}}:\underline{\underline{P}}:\underline{\tilde{\sigma}}_0 \tag{3-167}$$

The mapping of the stress state $\underline{\sigma}_0$ onto the stress state $\underline{\tilde{\sigma}}_0$ is done as follows. The strain increment is decomposed in an elastic part and a plastic part:

$$\Delta\underline{\varepsilon} = \gamma\Delta\underline{\varepsilon} + (1-\gamma)\Delta\underline{\varepsilon} \tag{3-168}$$

in which the scalar γ indicates the elastic part of the strain increment. The new initial stress state can now be written as:

$$\underline{\tilde{\sigma}}_0 = \underline{\sigma}_0 + \gamma\underline{\underline{E}}:\Delta\underline{\varepsilon} \tag{3-169}$$

The value of γ is calculated using the yield function description:

$$\underline{\tilde{\sigma}}_0:\underline{\underline{P}}:\underline{\tilde{\sigma}}_0 = \xi\sigma_y^2 \tag{3-170}$$

Replacing $\underline{\tilde{\sigma}}_0$ with expression (3-169) yields:

$$\begin{aligned}&\xi\sigma_y^2 = \left(\underline{\sigma}_0 + \gamma\Delta\underline{\varepsilon}:\underline{\underline{E}}\right):\underline{\underline{P}}:\left(\underline{\sigma}_0 + \gamma\underline{\underline{E}}:\Delta\underline{\varepsilon}\right) \Leftrightarrow \\ &\left(\Delta\underline{\varepsilon}:\underline{\underline{E}}:\underline{\underline{P}}:\underline{\underline{E}}:\Delta\underline{\varepsilon}\right)\gamma^2 + \left(2\Delta\underline{\varepsilon}:\underline{\underline{E}}:\underline{\underline{P}}:\underline{\sigma}_0\right)\gamma + \left(\underline{\sigma}_0:\underline{\underline{P}}:\underline{\sigma}_0 - \xi\sigma_y^2\right) = 0\end{aligned} \tag{3-171}$$

and hence:

$$\gamma_{1,2} = \frac{-\left(2\Delta\underline{\varepsilon}:\underline{\underline{E}}:\underline{\underline{P}}:\underline{\sigma}_0\right) \pm \sqrt{\left(2\Delta\underline{\varepsilon}:\underline{\underline{E}}:\underline{\underline{P}}:\underline{\sigma}_0\right)^2 - 4\left(\Delta\underline{\varepsilon}:\underline{\underline{E}}:\underline{\underline{P}}:\underline{\underline{E}}:\Delta\underline{\varepsilon}\right)\left(\underline{\sigma}_0:\underline{\underline{P}}:\underline{\sigma}_0 - \xi\sigma_y^2\right)}}{2\left(\Delta\underline{\varepsilon}:\underline{\underline{E}}:\underline{\underline{P}}:\underline{\underline{E}}:\Delta\underline{\varepsilon}\right)} \tag{3-172}$$

The positive value of γ, γ_1, gives a $\underline{\tilde{\sigma}}_0$ which lies between the initial stress state $\underline{\sigma}_0$ and the trial stress state $\underline{\sigma}_t$; the negative value of γ, γ_2, yields a $\underline{\tilde{\sigma}}_0$ at the opposite of the yield surface, see Figure 3-6. The new initial stress state $\underline{\tilde{\sigma}}_0$ is calculated with γ_1.

3.7.1 Consistent stiffness tensor

Since the new initial stress state $\underline{\tilde{\sigma}}_0$ depends on the predicted strain rate, it will contribute to the consistent stiffness tensor and hence a different expression for the consistent stiffness tensor has to be derived in case the stress state jumps from the elastic state to the plastic state. The starting point of the consistent stiffness derivation is equation (3-148):

$$\underline{\sigma}_1 = \underline{\sigma}_0 + \underline{\underline{E}}:\Delta\underline{\varepsilon} - \frac{\Delta\kappa}{\xi\sigma_y}\underline{\underline{E}}:\underline{\underline{P}}:\underline{\tilde{\sigma}}_0 \tag{3-173}$$

With equation (3-169) the above equation reads in differential form:

$$d\underline{\sigma}_1 = -\frac{1}{\xi\sigma_y}\left(1-\frac{h\Delta\kappa}{\sigma_y}\right)\underline{\underline{E}}:\underline{\underline{P}}:\tilde{\underline{\sigma}}_0 d\kappa - \frac{\Delta\kappa}{\xi\sigma_y}\underline{\underline{E}}:\underline{\underline{P}}:\left(\gamma\,\underline{\underline{E}}:d\underline{\varepsilon}+\underline{\underline{E}}:\Delta\underline{\varepsilon}d\gamma\right)+\underline{\underline{E}}:d\underline{\varepsilon} \tag{3-174}$$

For a neat consistent stiffness tensor also the derivative of γ must be taken into account. The expression for γ can be rewritten as follows, see equation (3-172):

$$\begin{aligned}\gamma_{1,2} &= \frac{1}{2}\left(\Delta\underline{\varepsilon}:\underline{\underline{E}}:\underline{\underline{P}}:\underline{\underline{E}}:\Delta\underline{\varepsilon}\right)^{-1}\left(-\left(2\Delta\underline{\varepsilon}:\underline{\underline{E}}:\underline{\underline{P}}:\underline{\sigma}_0\right)\pm\sqrt{\begin{array}{l}\left(2\Delta\underline{\varepsilon}:\underline{\underline{E}}:\underline{\underline{P}}:\underline{\sigma}_0\right)^2 - \\ 4\left(\Delta\underline{\varepsilon}:\underline{\underline{E}}:\underline{\underline{P}}:\underline{\underline{E}}:\Delta\underline{\varepsilon}\right)\left(\underline{\sigma}_0:\underline{\underline{P}}:\underline{\sigma}_0-\xi\sigma_y^2\right)\end{array}}\right) \\ &= \frac{1}{2}\left(\Delta\underline{\varepsilon}:\underline{\underline{E}}:\underline{\underline{P}}:\underline{\underline{E}}:\Delta\underline{\varepsilon}\right)^{-1}\left(-\left(2\Delta\underline{\varepsilon}:\underline{\underline{E}}:\underline{\underline{P}}:\underline{\sigma}_0\right)\pm\sqrt{D}\right)\end{aligned} \tag{3-175}$$

The derivative of γ reads:

$$\begin{aligned}d\gamma_{1,2} = &-\frac{1}{2}\left(\Delta\underline{\varepsilon}:\underline{\underline{E}}:\underline{\underline{P}}:\underline{\underline{E}}:\Delta\underline{\varepsilon}\right)^{-2}\left(2\Delta\underline{\varepsilon}:\underline{\underline{E}}:\underline{\underline{P}}:\underline{\underline{E}}:d\underline{\varepsilon}\right)\left(-\left(2\Delta\underline{\varepsilon}:\underline{\underline{E}}:\underline{\underline{P}}:\underline{\sigma}_0\right)\pm\sqrt{D}\right)+ \\ &\frac{1}{2}\left(\Delta\underline{\varepsilon}:\underline{\underline{E}}:\underline{\underline{P}}:\underline{\underline{E}}:\Delta\underline{\varepsilon}\right)^{-1}\left(\begin{array}{l}-\left(2\underline{\sigma}_0:\underline{\underline{P}}:\underline{\underline{E}}:d\underline{\varepsilon}\right)\pm \\ \dfrac{1}{2}\dfrac{1}{\sqrt{D}}\left(\begin{array}{l}8\left(\Delta\underline{\varepsilon}:\underline{\underline{E}}:\underline{\underline{P}}:\underline{\sigma}_0\right)\left(\underline{\sigma}_0:\underline{\underline{P}}:\underline{\underline{E}}:d\underline{\varepsilon}\right)- \\ 8\left(\underline{\sigma}_0:\underline{\underline{P}}:\underline{\sigma}_0-\xi\sigma_y^2\right)\left(\Delta\underline{\varepsilon}:\underline{\underline{E}}:\underline{\underline{P}}:\underline{\underline{E}}:d\underline{\varepsilon}\right)\end{array}\right)\end{array}\right)\end{aligned} \tag{3-176}$$

or after rearranging:

$$d\gamma_{1,2} = \left[\begin{array}{l}-\left(\Delta\underline{\varepsilon}:\underline{\underline{E}}:\underline{\underline{P}}:\underline{\underline{E}}:\Delta\underline{\varepsilon}\right)^{-2}\left(-\left(2\Delta\underline{\varepsilon}:\underline{\underline{E}}:\underline{\underline{P}}:\underline{\sigma}_0\right)\pm\sqrt{D}\right)\left(\Delta\underline{\varepsilon}:\underline{\underline{E}}:\underline{\underline{P}}:\underline{\underline{E}}\right)+ \\ \left(\Delta\underline{\varepsilon}:\underline{\underline{E}}:\underline{\underline{P}}:\underline{\underline{E}}:\Delta\underline{\varepsilon}\right)^{-1}\left(-\underline{\sigma}_0:\underline{\underline{P}}:\underline{\underline{E}}\pm\dfrac{1}{\sqrt{D}}\left(\begin{array}{l}2\left(\Delta\underline{\varepsilon}:\underline{\underline{E}}:\underline{\underline{P}}:\underline{\sigma}_0\right)\left(\underline{\sigma}_0:\underline{\underline{P}}:\underline{\underline{E}}\right)- \\ 2\left(\underline{\sigma}_0:\underline{\underline{P}}:\underline{\sigma}_0-\xi\sigma_y^2\right)\left(\Delta\underline{\varepsilon}:\underline{\underline{E}}:\underline{\underline{P}}:\underline{\underline{E}}\right)\end{array}\right)\right)\end{array}\right]:d\underline{\varepsilon} \tag{3-177}$$

The derivative of the stress-strain relation is obtained by substitution of equation (3-177) into equation (3-174):

$$\begin{aligned}d\underline{\sigma}_1 &= -\frac{1}{\xi\sigma_y}\left(1-\frac{h\Delta\kappa}{\sigma_y}\right)\underline{\underline{E}}:\underline{\underline{P}}:\tilde{\underline{\sigma}}_0 d\kappa - \frac{\Delta\kappa}{\xi\sigma_y}\underline{\underline{E}}:\underline{\underline{P}}:\left(\gamma\,\underline{\underline{E}}:d\underline{\varepsilon}+\underline{\underline{E}}:\Delta\underline{\varepsilon}d\gamma\right)+\underline{\underline{E}}:d\underline{\varepsilon} \\ &= \underline{\underline{Z}}:d\underline{\varepsilon}-\left(\frac{1}{\xi\sigma_y}\left(1-\frac{h\Delta\kappa}{\sigma_y}\right)\underline{\underline{E}}:\underline{\underline{P}}:\tilde{\underline{\sigma}}_0\right)d\kappa\end{aligned} \tag{3-178}$$

where:

$$\underline{\underline{Z}} = \left(\begin{array}{l}\left(\underline{\underline{E}}-\gamma\dfrac{\Delta\kappa}{\xi\sigma_y}\underline{\underline{E}}:\underline{\underline{P}}:\underline{\underline{E}}\right)- \\ \dfrac{\Delta\kappa}{\xi\sigma_y}\Delta\underline{\varepsilon}:\underline{\underline{E}}:\underline{\underline{P}}:\underline{\underline{E}}\left(\begin{array}{l}-\left(\Delta\underline{\varepsilon}:\underline{\underline{E}}:\underline{\underline{P}}:\underline{\underline{E}}:\Delta\underline{\varepsilon}\right)^{-2}\left(-\left(2\Delta\underline{\varepsilon}:\underline{\underline{E}}:\underline{\underline{P}}:\underline{\sigma}_0\right)\pm\sqrt{D}\right)\left(\Delta\underline{\varepsilon}:\underline{\underline{E}}:\underline{\underline{P}}:\underline{\underline{E}}\right)+ \\ \left(\Delta\underline{\varepsilon}:\underline{\underline{E}}:\underline{\underline{P}}:\underline{\underline{E}}:\Delta\underline{\varepsilon}\right)^{-1}\left(\begin{array}{l}-\underline{\sigma}_0:\underline{\underline{P}}:\underline{\underline{E}}\pm \\ \dfrac{1}{\sqrt{D}}\left(\begin{array}{l}2\left(\Delta\underline{\varepsilon}:\underline{\underline{E}}:\underline{\underline{P}}:\underline{\sigma}_0\right)\left(\underline{\sigma}_0:\underline{\underline{P}}:\underline{\underline{E}}\right)- \\ 2\left(\underline{\sigma}_0:\underline{\underline{P}}:\underline{\sigma}_0-\xi\sigma_y^2\right)\left(\Delta\underline{\varepsilon}:\underline{\underline{E}}:\underline{\underline{P}}:\underline{\underline{E}}\right)\end{array}\right)\end{array}\right)\end{array}\right)\end{array}\right) \tag{3-179}$$

An expression for $d\kappa$ as a function of $d\underline{\varepsilon}$ can be derived from the derivative of the yield function, see equation (3-135):

$$h\xi\sigma_y d\kappa = \underline{\sigma}_1 : \underline{\underline{P}} : d\underline{\sigma}_1 \Rightarrow \qquad d\kappa = \frac{\underline{\sigma}_1 : \underline{\underline{P}} : \underline{\underline{Z}}}{h\xi\sigma_y + \frac{1}{\xi\sigma_y}\left(1 - \frac{h\Delta\kappa}{\sigma_y}\right)\underline{\sigma}_1 : \underline{\underline{P}} : \underline{\underline{E}} : \underline{\underline{P}} : \underline{\tilde{\sigma}}_0} : d\underline{\varepsilon} \tag{3-180}$$

Combining equations (3-178) and (3-167) gives the neat consistent stiffness tensor for Euler forward integration for when the stress state jumps from the elastic state to the plastic state. In this formulation, the strain dependence of the scalar γ is taken into account:

$$d\underline{\sigma}_1 = \left(\underline{\underline{Z}} - \frac{\frac{1}{\xi\sigma_y}\left(1 - \frac{h\Delta\kappa}{\sigma_y}\right)\left(\underline{\underline{E}} : \underline{\underline{P}} : \underline{\tilde{\sigma}}_0\right)\left(\underline{\sigma}_1 : \underline{\underline{P}} : \underline{\underline{Z}}\right)}{h\xi\sigma_y + \frac{1}{\xi\sigma_y}\left(1 - \frac{h\Delta\kappa}{\sigma_y}\right)\underline{\sigma}_1 : \underline{\underline{P}} : \underline{\underline{E}} : \underline{\underline{P}} : \underline{\tilde{\sigma}}_0} \right) : d\underline{\varepsilon} \tag{3-181}$$

3.8 Applications

After the previous theoretical consideration, the performance of the mixed elastoplastic / rigid plastic material model will be investigated for two academic problems and a realistic problem. The mixed material model is applied in two configurations. The first configuration makes use of the consistent stiffness tensor (see Sections 3.6.3 and 3.7.1). The second configuration makes direct use of the expression for the new stress state (equation (3-148) for the elastoplastic part and equation (3-149) for the rigid plastic part), from now on called the direct approach. For the elastoplastic part of the latter configuration, the stiffness tensor will be the elasticity tensor and the term with the old stress state will be taken into account at the right-hand side of the finite element equations.

The results obtained with the mixed material model are compared with the results obtained with a consistent Euler backward elastoplastic material model and a rigid plastic material model.

3.8.1 One-element test

The one-element test is performed to investigate the convergence behavior of the mixed elastoplastic / rigid plastic material model compared to the other material models. A 3-node triangular element was used in this test.

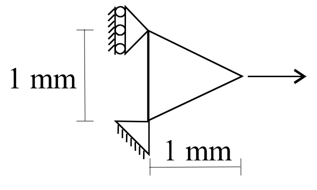

Figure 3-7. One-element test

One node is suppressed in both the x- and y-directions, a second node is only suppressed in the x-direction and the third node is pulled in the x-direction. Simulations with two different magnitudes of the displacement increments were performed, i.e. a displacement increment of 0.001 mm to test the elastoplastic part of the mixed material model, and a displacement increment of 0.01 mm to test the rigid plastic part of the mixed material model. The mechanical unbalance criterion was set at 10^{-14}.

After 30 steps, prescribing a displacement increment of 0.001 mm, the elastoplastic material model gave a yield stress of 304.3 MPa and a plastic thickness strain of -0.0140 for isotropic material behavior, and in each step quadratic convergence was observed. The mixed elastoplastic / rigid plastic material model gave the same results as the elastoplastic material model for both the consistent and the direct approaches. However the consistent algorithm showed quadratic convergence while the direct algorithm showed slower convergence, as expected. For anisotropic material behavior (R_0 = 1.85, R_{45} = 1.52, R_{90} = 2.37) the elastoplastic material model gave a yield stress of 301.3 MPa and a plastic thickness strain of -0.00989, and in each step quadratic convergence was observed. Again the mixed elastoplastic / rigid plastic material model gave the same results as the elastoplastic material model for both the consistent (quadratic convergence) and the direct (slower convergence) approaches.

After 30 steps, prescribing a displacement increment of 0.01 mm, the rigid plastic material model gave a yield stress of 448.2 MPa and a plastic thickness strain of -0.132 for isotropic material behavior and a yield stress of 440.9 MPa and a plastic thickness strain of -0.0925 for anisotropic material behavior (R_0 = 1.85, R_{45} = 1.52, R_{90} = 2.37). Convergence was reached in 1 iteration per step. The mixed elastoplastic / rigid plastic material model gave the same simulation results while for both the consistent and the direct approaches, convergence was reached in 1 iteration also.

From the one-element test it can be concluded that, depending on the displacement increment, the mixed elastoplastic / rigid plastic material model shows the same performance as the elastoplastic material model or the rigid plastic material model and that consistency, when applied, is proven by quadratic convergence.

3.8.2 Tensile test

In order to preserve quadratic convergence the stiffness tensor must be consistent with the integration algorithm and changes of geometry. However, the mixed elastoplastic / rigid plastic material model is not set up consistently with respect to changes in geometry due to the complexity involved in taking into account the differential form of the $\underline{\boldsymbol{B}}$-tensor. As a result, quadratic convergence will not be observed when the geometry changes during the computation, which will be shown with the help of the tensile test. To model this test, 20 triangular elements were used, see Figure 3-8. The nodes at the lower side of the strip are suppressed in the y-direction, representing the center line. The nodes at the left side of the strip are suppressed in the x-direction and the nodes at the right side of the strip are pulled in the x-direction.

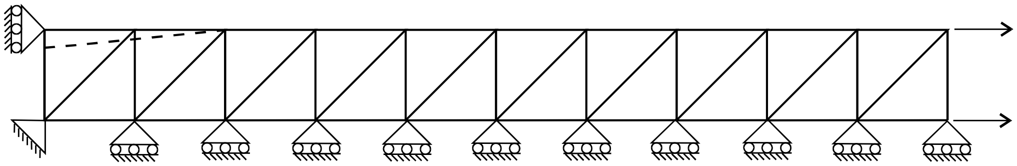

Figure 3-8. Finite element mesh of the tensile test

The performance of the mixed material model was compared with the elastoplastic model and the rigid plastic model during 100 incremental steps. Again the step size was varied to validate the elastoplastic part and the rigid plastic part of the mixed material model and simulations were performed for both isotropic and anisotropic material behavior. The mechanical unbalance criterion was set at 10^{-14}.

The elastoplastic material model and the consistent elastoplastic part of the mixed material model gave the same simulation results after 100 steps and showed quadratic convergence per step, whereas convergence was reached after 3 iterations. The direct approach of the mixed material model also showed the same simulation results, however, convergence was linearly reached after 10 iterations. Also the rigid plastic material model and the rigid plastic part of the mixed material model for both the consistent and direct approaches gave the same results after 100 steps while convergence was reached in 1 iteration.

Another simulation was performed in which the mixed material model switched from the rigid plastic state to the elastoplastic state and vice versa during the simulation. The convergence behavior of this simulation equaled the convergence behavior of the separate parts of the model as described above.

In the previous set of simulations the deformation pattern was uniform and no necking occured. To enforce necking and thus to enforce changes in geometry, a small imperfection of 1% of the strip width at the left-hand side of the strip was introduced, see the dashed line in Figure 3-8. The first few steps of the simulation were fully elastic in the case of the elastoplastic material model. Since linear elasticity was assumed, convergence should have been reached in 1 iteration. However 3 or 4 iterations were necessary to reach the unbalance criterion of 10^{-14}, caused by the non-consistent approach of geometrical non-linearity during the iterative procedure. In the subsequent steps the material starts to deform plastically and hence almost quadratic convergence was observed (7 iterations per step) using the elastoplastic material model and the consistent elastoplastic part of the mixed material model. Again, quadratic convergence was not observed due to geometrical non-linearity. In the case of the direct approach, the elastoplastic part of the mixed material model needed about 900 iterations per step to reach convergence which was a consequence of using the elasticity tensor as the stiffness tensor.

3.8.3 Rectangular product

The deep drawing of a rectangular product was used to compare the behavior of the mixed elastoplastic / rigid plastic material model with that of the elastoplastic material model and the rigid plastic material model in a simulation of a realistic problem. The geometry of the rectangular tools and the blank are given in Figure 3-9. The product depth was 75 mm and the blank thickness was 0.7 mm.

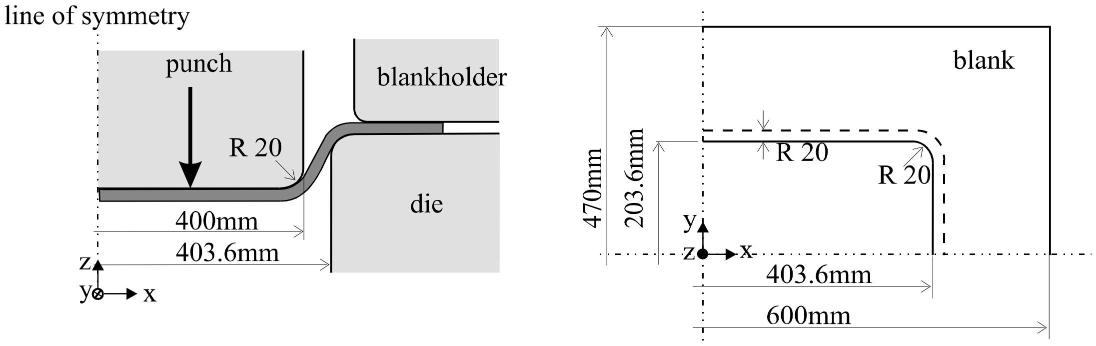

Figure 3-9. Tool geometry

A first set of simulations was performed with an incremental step size of 0.2 mm where the three material models were applied separately. The material behavior was assumed to be isotropic, the mechanical unbalance was set at 0.02. The plastic thickness strain distribution in the rectangular product after 75 mm deep drawing is depicted in Figure 3-10 for the three material models used.

It is observed that the thickness strain distribution calculated with the mixed elastoplastic / rigid plastic material model inclines towards the results calculated with the elastoplastic material model whereas the results of the rigid plastic material model differ drastically from the results obtained with the other material models. The plastic thickness strain in the case of the rigid plastic material model is higher than the plastic thickness strain in the elastoplastic and the mixed material models. This can be explained as follows. The denominator of the rigid plastic formulation (see equation (3-114)) consists of the equivalent plastic strain increment. Problems arise when no plastic strain occurs in some parts of the product during the deep drawing simulation, the so-called dead metal zones. To avoid division by zero in the rigid plastic formulation, a small amount of fictive strain is assumed when no plastic strain occurs. The effect of this fictive strain on the deep drawing simulation would be very small if it is set to a very small value. However, when the value of the fictive strain is set too small, the stress is forced to the yield surface, even if in reality the situation should be elastic. This will lead to bad convergence and locally incorrect results. Therefore, the fictive strain is set to a value that represents the strain increment causing the stress state from zero to the yield surface. In this case the rigid plastic material model degenerates to a viscous model for small strain increments. Consequently, the plastic strain will be considerably overestimated in the dead metal zones, such as the bottom of the product and in some parts of the flange, when the rigid plastic formulation is used.

The simulation with the mixed elastoplastic / rigid plastic material model was performed using the direct approach. Simulations using the consistent approach did not converge after a few steps. The reason for not converging is that for an integration point, the state of the mixed material model can change from elastoplastic to rigid plastic (or reverse) during the iteration process. Since it was only required that the stress state of both parts of the model had to be on the yield surface for the case in which the incremental plastic strain $\Delta\kappa$ equals the reference strain κ_{ref}, it is not demanded that the direction of the stress state of both parts must be equal. This difference between the directions of the stress states, determined with both parts of the mixed material model, yields a non-converging process.

A second set of simulations was performed in which the material behavior was assumed to be anisotropic ($R_0 = 1.85$, $R_{45} = 1.52$, $R_{90} = 2.37$). The mechanical unbalance was set at 0.02 and the incremental step size was 0.4 mm. The thickness strain distribution in the rectangular product after 75 mm deep drawing is shown in Figure 3-11 for the elastoplastic material model, the mixed material model and the rigid plastic material model. Again, the simulation results obtained with the mixed elastoplastic / rigid plastic material model incline towards the elastoplastic material model. The reason for the divergent values obtained with the rigid plastic material model has already been described in this section concerning isotropic material behavior.

Finally, the robustness of both the elastoplastic material model and the mixed elastoplastic / rigid plastic material model were compared. For this purpose the incremental step size was increased until the simulation no longer converged, starting with a step size of 0.1 mm with an interval of 0.1 mm. For the elastoplastic material model the maximum step size reached was 0.5 mm. For the mixed material model the maximum step size reached was 0.8 mm. From this it can be concluded that the mixed material model is more stable than the elastoplastic material model. However, the convergence behavior of the mixed material model is worse than the elastoplastic material model since the consistent formulation of the mixed material model cannot be used for deep drawing simulations.

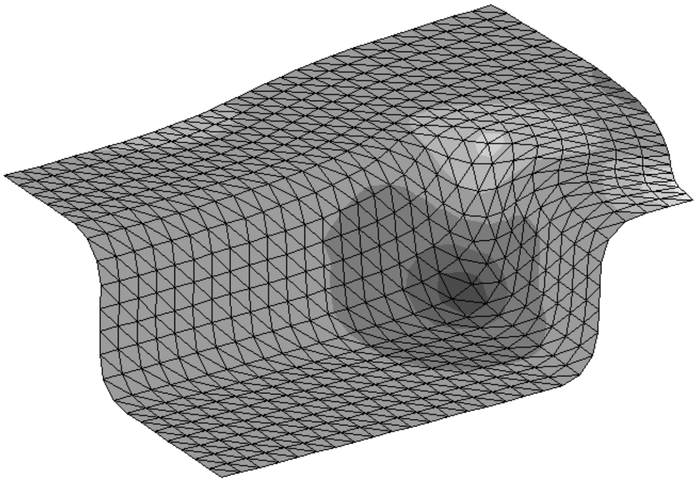

elastoplastic material model

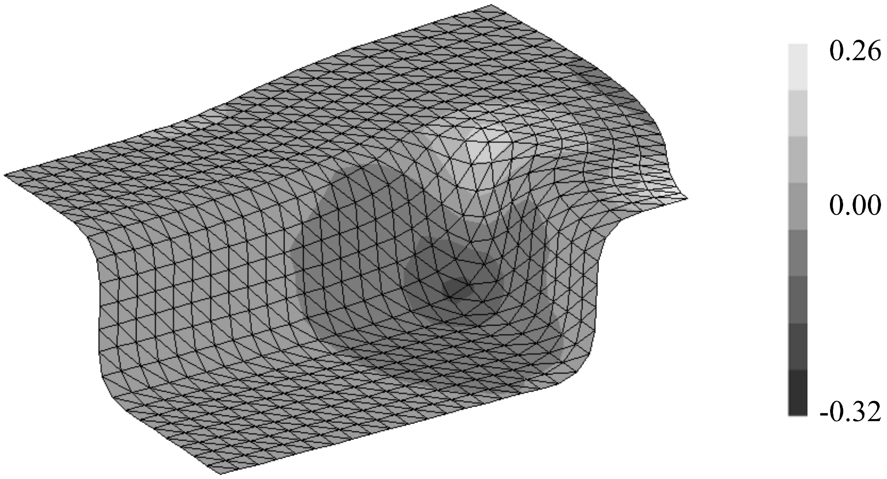

mixed elastoplastic / rigid plastic material model

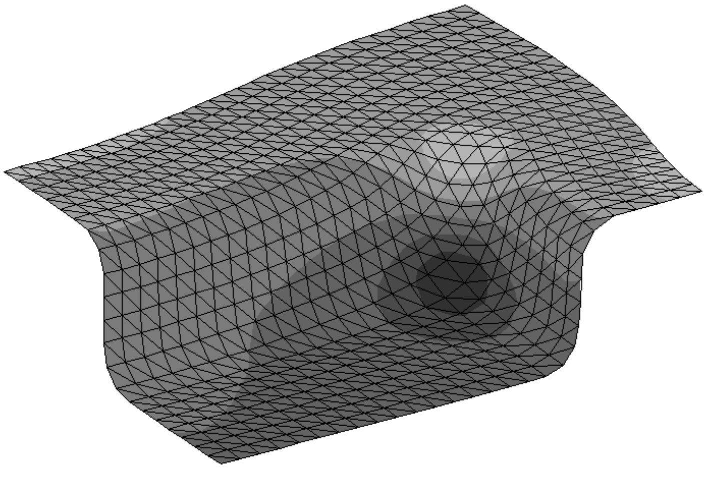

rigid plastic material model

Figure 3-10. Plastic thickness strain distribution in the rectangular product for isotropic material behavior

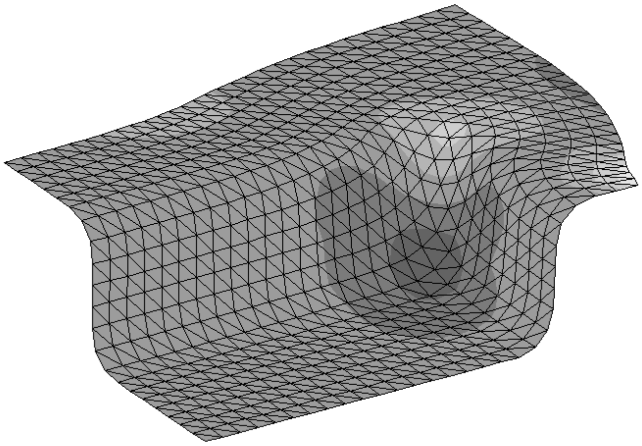

elastoplastic material model

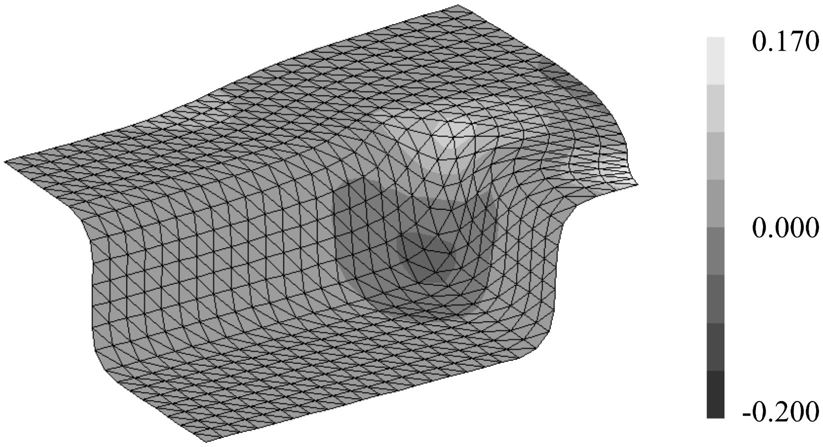

mixed elastoplastic / rigid plastic material model

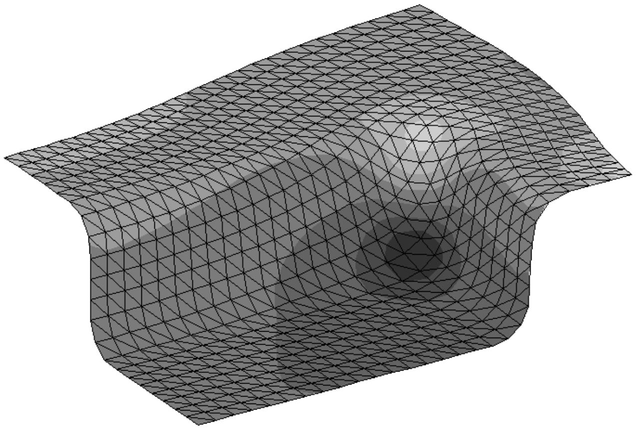

rigid plastic material model

Figure 3-11. Plastic thickness strain distribution in the rectangular product for anisotropic material behavior

3.9 Discussion

The advantage of the rigid plastic material model is its robust behavior and fast computation time. However, the model is not capable of accurately describing the deformation behavior in dead metal zones. The plastic strain is considerably overestimated in these zones, hereby affecting the deformation behavior of the entire product. The rigid plastic material model is, however, perfectly suitable for highlighting deformation trends. For an accurate computation, the elastoplastic material model or the mixed elastoplastic / rigid plastic material model must be used despite the increase in computation time.

The stiffness tensor derived is consistent with the integration algorithm for the mixed elastoplastic / rigid plastic material model. Quadratic convergence is observed for the academic problems as described in the former section, even if the state of mixed material model switches from elastoplastic plastic to rigid plastic during the simulation. Since the academic problems have a 1-dimensional character, the direction of the stress state for both parts of the model is almost equal in case that $\Delta\kappa = \kappa_{ref}$. However, the consistent approach fails in realistic problems such as deep drawing where the deformation pattern has a 3-dimensional character. Consequently, at the reference strain, the direction of the stress state determined by both parts of the model are not equal, yielding a non-converging process. Therefore the direct approach of the mixed material model must be used in this type of problem.

The direct approach of mixed material model is more robust than the elastoplastic material model but it needs more iterations per step to converge. As a consequence, a simulation with large incremental steps using the mixed material model will be as fast as a simulation with smaller incremental steps using the elastoplastic material model. Since a simulation becomes more accurate at smaller incremental steps, generally the elastoplastic material model is preferred to the mixed material model. Only for critical product simulations which can be run overnight, is the mixed material model to be favored to increase the chance of a converging simulation.

3.10 References

[Atzema, 1992]
Atzema E.H., J. Huétink, ‘Incremental formulations of rigid-plastic and elastic-plastic constitutive equations for simulation of forming processes’, Computational Plasticity Fundamentals and Applications, D.R.J. Owen et al. (eds.), Pineridge Press, Swansea, p. 1065-1076, 1992

[Atzema, 1994]
Atzema E.H., ‘Formability of sheet metal and sandwich laminates’, Ph.D. Thesis, University of Twente, Enschede, ISBN 90-90069410, 1994

[Borst, 1990]
Borst R. de, P.H. Feenstra, ‘Studies in anisotropic plasticity with reference to the Hill criterion’, Int. J. Num. Meth. Eng., vol. 29, p. 315-336, 1990

[Carleer, 1997]
Carleer B.D., ‘Finite element analysis of deep drawing’, Ph.D. Thesis, University of Twente, Enschede, ISBN 90-90103589, 1997

[Drucker, 1949]

Drucker D.C., ‘The significance of the criterion for additional plastic deformation of metals’, J. Colloid Sci. vol. 3, p. 299-311, 1949

[Hill, 1950]
Hill R., ‘The mathematical theory of plasticity’, Clarendon Press, Oxford, 1950

[Huétink, 1999]
Huétink J., A.H. v.d. Boogaard, A.D. Rietman, J. Lof, T. Meinders, ‘A mixed elastoplastic / rigid plastic material model’, Int. J. Num. Meth. Eng., vol. 46, p. 1421-1434, 1999

[Hughes, 1998]
Hughes T.J.R., T. Belytschko, ‘Nonlinear finite element analysis’, short course, vol. 3, 1998

[Koenis, 1994]
Koenis P.T.G., ‘The Hill yield criterion in the finite element method’, Master’s Thesis, University of Twente, Enschede, 1994

[Meinders, 1999]
Meinders T, A.H. van den Boogaard, J. Huétink, ‘A mixed elastoplastic / rigid plastic material model’, Proceedings of the 4th International Conference on Numerical Simulations of 3-D Sheet Metal Forming Processes, J.C. Gelin & P. Picard (eds.), vol.1, p. 137-142, 1999

[Nikishkov, 1993]
Nikishkov G.P., S.N. Atluri, ‘Implementation of a generalized midpoint algorithm for integration of elastoplastic constitutive relations for Von Mises hardening material’, Comput. Struct., vol. 49, p. 1037-1044, 1993

[Ortiz, 1985]
Ortiz M., E.P. Popov, ‘Accuracy and stability of integration algorithms for elastoplastic constitutive relations’, Int. J. Num. Meth. Eng., vol. 21, p. 1561-1576, 1985

[Ortiz, 1986]
Ortiz M., J.C. Simo, ‘An analysis of a new class of integration algorithms for elastoplastic constitutive equations’, Int. J. Num. Meth. Eng., vol. 23, p. 353-366, 1986

[Rice, 1971]
Rice J.R., D.M. Tracy, ‘Computational fracture mechanics’, Symp. Num. and Comp. Meth. Struct. Mech., Fenves (ed.) Urbana, Illinois, New York, Adademic Press, p. 585-623, 1971

[Simo, 1985a]
Simo J.C., M. Ortiz, ‘A unified approach to finite deformation elastoplastic analysis based on the use of hyperelastic constitutive equations’, Comp. Meth. Appl. Mech. Eng., vol. 49, p. 221-245, 1985

[Simo, 1985b]
Simo J.C., R.L. Taylor, ‘Consistent tangent operators for rate-independent plasticity’, Comp. Meth. Appl. Mech. Eng., vol. 48, p. 101-118, 1985

[Simo, 1998]
Simo J.C., T.J.R. Hughes, ‘Computational inelasticity’, Springer-Verlag New York, 1998

[Vreede, 1992]
Vreede P.T., ‘A finite element method for simulations of 3-dimensional sheet metal forming, Ph.D. Thesis, University of Twente, Enschede, ISBN 90-90047549, 1992

[Wilkins, 1964]
Wilkins M.L., ‘Calculation of elastic-plastic flow’, Methods of Computational Physics, Alder et al. (eds.), vol. 3, p. 211-263, New York, Academic Press, 1964

4. Equivalent drawbead model

4.1 Introduction

The quality of a sheet metal stamping part is secured by the material flow into the die cavity. Therefore it is important to control the material flow rate to avoid defects like wrinkling and tearing. Furthermore, in car body manufacturing it is important that outer panels should be subjected to sufficient straining because of the flex resistance. Generally, the material flow is controlled by the blankholder: a restraining force is created by friction between the tools and the blank. However, during the forming stage, the blankholder does not make contact with the entire blank which means that it cannot fully control the material flow. Moreover, when a high restraining force is required, a higher blankholder force must be applied which may cause excessive wear in the tools and galling in the blank [Xu, 1997]. Therefore, a local control mechanism is desired which restrains the material flow sufficiently at relatively low blankholder pressure. These demands can be fulfilled by drawbeads, which are protrusions on the die surface, see Figure 4-1. A drawbead consists of two components, the bead itself and a matching groove, the contra-bead. The drawbead creates a restraining force by cyclically bending and unbending the sheet as it traverses the drawbead, causing strain hardening and a change in the strain distribution with consequently thinning of the blank [Wouters, 1994], [Carleer, 1994], [Triantafyllidis, 1986], [Maker, 1987].

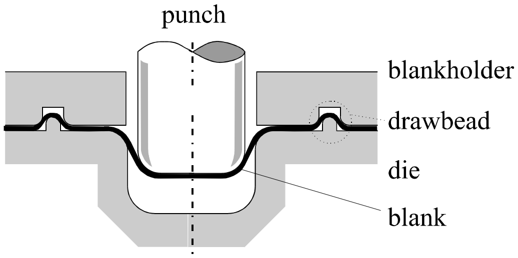

Figure 4-1. Deep drawing process including drawbeads

The performance of the drawbead, or drawbead-like protrusions such as stepbeads or endbeads (Figure 4-2), is mainly determined by the drawbead geometry. The radii of the drawbead and the clearance between the drawbead tools can be varied, but also the shape of the cross-section. The shape of the cross-section can be semicircular ($w = 2R$, see Figure 4-2), rectangular or non-symmetric, where each shape has its specific characteristics. When a semi-circular drawbead geometry is used, the material is subjected to three bending and unbending sequences, whereas for the rectangular drawbead geometry, the material is subjected to four bending and unbending sequences. Therefore, the drawbead with a rectangular cross-section will lead to a higher restraining force provided that the bending radii are the same. Another characteristic of the rectangular drawbead is that it is relatively insensitive to lubrication. This is explained as follows. The blank does not follow the rectangular drawbead geometry at the top of the bead during forming, but creates a small cavity between the tool and the blank, see Figure 4-2 (left picture). This cavity is situated between the two radii of the bead and becomes a depot for the lubricant which is easily squeezed out of the contact areas due to this cavity.

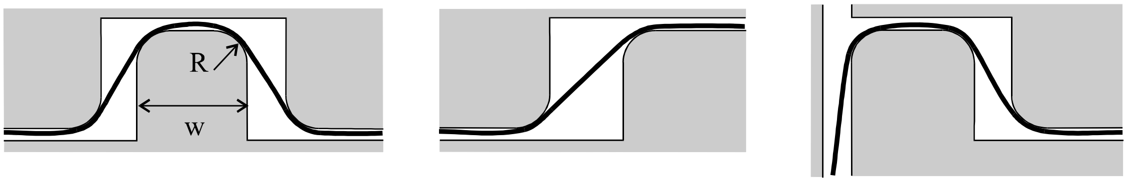

drawbead stepbead endbead

Figure 4-2. Cross-section of a drawbead, stepbead and endbead

To take into account the effects of the drawbead on the deep drawing process, the drawbead should be modeled properly in a finite element simulation to guarantee an accurate simulation. However, modeling the exact drawbead geometry requires a large number of elements due to the small radii of the drawbead. Evidently this large number of elements will increase the computation time for such finite element simulations drastically. An equivalent drawbead approach is therefore commonly adopted in finite element codes to overcome this problem of excessive computation time. The commonly used equivalent drawbead models represent the drawbead as an additional and constant drawbead restraining force [Haug, 1991], [Kawka, 1994], [Taylor, 1993], [Stoughton, 1988], whereas the model of Stoughton is used most widely. A more sophisticated model which accounts for the influence of the drawbead penetration depth on the drawbead restraining force is under construction [Mattiasson, 1999]. Consequently, the history of the drawbead restraining force as well as the changes in the strain distribution and thinning of the blank are not taken into account in these equivalent drawbead models, which results in inaccurate modeling of the drawbead behavior [Carleer, 1997], [Meinders, 1998b].

This chapter contains the description of an equivalent drawbead model which does incorporate the effects of sheet thinning and strain changes. Both the drawbead restraining force (DBRF) and the plastic thickness strain are considered to be history dependent. In this equivalent drawbead model the real drawbead is replaced by an artificial line on the tool surface on which a numerical algorithm acts. A discrete material element passing this line will experience a time dependent DBRF and a time dependent thickness strain. Simultaneously a drawbead lift force, which appears when material is pulled through the drawbead, is subtracted from the total blankholder force. The drawbead forces and strains can be obtained from experiments or from a 2D plane strain drawbead simulation, in which the real drawbead is accurately simulated.

The 2D plane strain drawbead model is discussed in Section 4.2. Experiments performed to validate the performance of the 2D drawbead model, are also presented here. The implementation of the DBRF, the lift force and the plastic thickness strain in the equivalent drawbead model are discussed in Section 4.3. Two different algorithms have been developed to take into account the plastic thickness strain. One algorithm is based on a stress estimate and one algorithm is based on a penalty constraint method. In Section 4.4 the performance of the equivalent drawbead model in deep drawing simulations is investigated.

4.2 2D plane strain drawbead model

A 2D plane strain drawbead model was developed to obtain accurate data concerning the drawbead forces and the thickness strain during the forming process. First, the reliability of the 2D drawbead model is proven. Subsequently the model is used to determine the process dependent drawbead forces and strains for all possible drawbead geometries. Note that the plane strain assumption holds for the straight part of the drawbead. The deformation patterns of the blank in the vicinity of the drawbead ends are fully three dimensional and hence the plane strain model does not hold for these parts of the drawbead.

The 2D plane strain drawbead model makes use of the Arbitrary Lagrangian Eulerian (ALE) formulation [Huétink, 1986], [Huétink, 1990], [Helm, 1998]. This formulation is characterized by an uncoupling of the material and the grid displacements. The mesh can be deformed in a restricted way independently of the material flow: the mesh is fixed in the main flow direction, but it is free to deform perpendicular to this flow direction. The main advantages of this ALE-formulation are that the grid refinements remain at their initial position and that the effects of sheet thinning can be described as well. Since the grid is fixed in the flow direction, far less elements can be used than when an Updated Lagrangian formulation is applied, where refinements must be used on the complete sheet, since in the latter formulation the material and grid displacements are fully coupled.

The finite element mesh of the 2D drawbead model is depicted in Figure 4-3. A pre-deformed blank is used in the 2D drawbead model since the initial closing of the drawbead hardly affects the simulation results while taking up 25% of the computation time [Beugels, 1993], [Brouwer, 1999]. The blank is modeled with 4-node bilinear plane strain elements. Contact between the sheet and the drawbead is described by contact elements [Huétink, 1989]. An extra bend is added to the 2D drawbead model to obtain simulation results which can directly be compared with the experimental results.

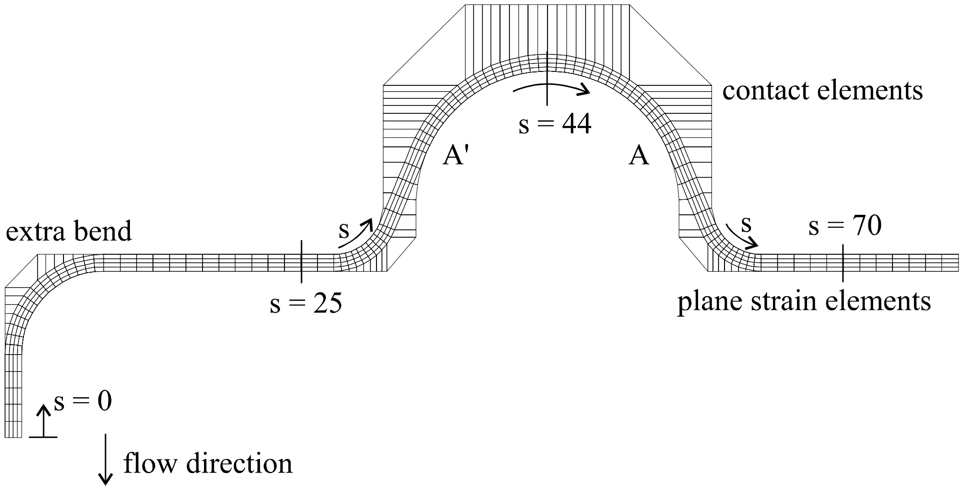

Figure 4-3. Finite element mesh of the 2D plane strain drawbead model. Coordinate distance ‘s’ in the drawbead is given in [mm]

4.2.1 Convection schemes

The ALE formulation can be divided into two steps. The first step is a usual Langrangian step, followed by a second step which is an explicit Eulerian step (purely convective). This method is known as the split ALE formulation.

After the Langrangian step, the integration point values must be mapped onto the mesh defined by the user (Eulerian step). The mapping can be established by constructing a function f based on the integration point data of the Lagrangian mesh [Helm, 1998]. A mathematical representation of this Eulerian step is given by the convection equation:

$$\frac{\partial f}{\partial t} + v \cdot \frac{\partial f}{\partial x} = 0 \tag{4-182}$$

The convected quantity is denoted by *f*, the relative velocity between the material and the mesh is denoted by *v*. The mapping can be established by solving the above convection equation. In the literature various schemes can be found which deal with this problem. In this section three different schemes are compared, i.e. an isotropic scheme and an orthotropic scheme proposed by Huétink [Huétink, 1986], and a finite volume $\kappa = 1/3$-scheme [Stoker, 1999].

In brief, the different schemes work as follows. The schemes of Huétink are based on a central difference method applying node averaging combined with interpolation techniques to determine the new value of *f*. The central difference method leads to oscillation whereas the interpolation technique suffers from numerical diffusion. Both techniques are combined using a heuristic weight factor based on the incremental step size where the interpolation technique acts like a smoothing algorithm. Oscillations in the central difference method occur in the part of the algorithm where the gradient of the function *f* is multiplied by the incremental displacement vector. For the isotropic scheme the interpolation algorithm has the same numerical diffusion in all directions, consequently leading to numerical diffusion perpendicular to the flow direction. In the orthotropic scheme the interpolation part of the algorithm is replaced by a combination of interpolation and extrapolation techniques, where the Courant number depends on the direction. In the central difference method oscillations do not occur in the direction perpendicular to the flow direction. Therefore it is not necessary to apply smoothing in the direction perpendicular to the flow direction, and hence extrapolation techniques, which do not suffer from smoothing, are used to determine the value of *f*. More details of the orthotropic scheme can be found in [Wisselink, 2000].

The finite volume method is based on a balance of fluxes of the value *f* between the surrounding elements, which makes the method conservative. A method is said to be conservative if the integral of a state variable over the whole domain remains the same. The boundary integral is determined independently from the element from which it is considered. This results in an ingoing flux of one element being equal to the outgoing flux for another element. A cell-centered finite volume scheme based on integration point data is used which depends on a factor κ. For $\kappa = 1$ the scheme degenerates to an upwind scheme whereas for $\kappa = 1/3$ it is shown that the scheme is even third-order accurate for steady state situations [Stoker, 1999]. Special limiter functions must be used to prevent oscillations.

The three different convection schemes are used in the 2D plane strain model for one specific drawbead geometry to compare the performance of each scheme [Brouwer, 1999]. The DBRF needed to pull the sheet through the drawbead is given in Figure 4-4 as a function of the material displacement. Both the isotropic and the orthotropic convection scheme reach their steady state value, whereas the κ=1/3 scheme does not converge to a steady state value. However, the DBRF and the plastic thickness strain both reach their steady state value when a material particle has been pulled through the entire drawbead [Cao, 1993]. Also, some oscillations can be observed in the κ=1/3 scheme.

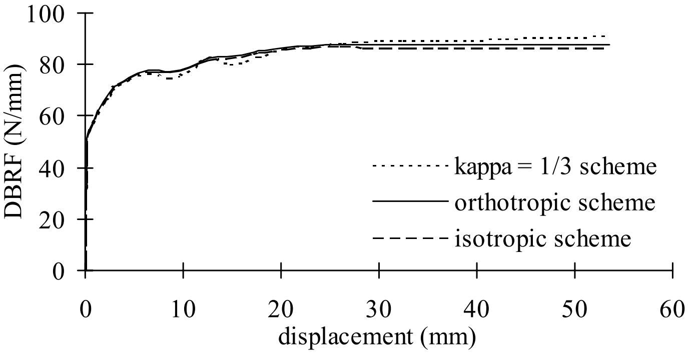

Figure 4-4. Drawbead restraining force as a function of the material displacement

The equivalent plastic strain in the mid-plane of the blank is given in Figure 4-5 as a function of the material displacement. The three convection schemes show major differences in the calculated equivalent plastic strain.

First the difference in graph shapes between the three convection schemes is examined. The isotropic scheme and the orthotropic scheme increase monotonously as expected, whereas the $\kappa=1/3$ scheme shows sections with a negative gradient. This was also observed by [Pelgrim, 1997]. From the definition of equivalent plastic strain, it is impossible to have negative gradients in the equivalent plastic strain graph. It can be concluded that despite the limiter used, oscillations still occur for the $\kappa=1/3$ scheme leading to non-realistic simulation results.

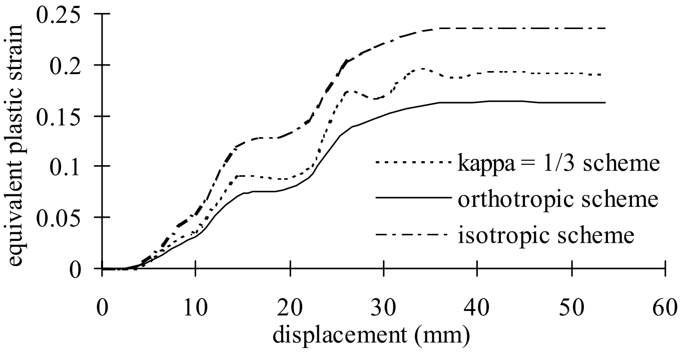

Figure 4-5. Equivalent plastic strain distribution in the mid-plane as a function of the material displacement

Second, the difference in steady state values of the three convection schemes is considered. These differences can be explained by plotting the equivalent plastic strain as a function of the position in the blank thickness direction, see Figure 4-6. The mid-plane of the blank is situated at 0.4 mm. The stress and strain distribution across the blank thickness must show a maximum value at the outer fibers and a minimum at the mid-plane of the blank. However, in the isotropic convection scheme numerical diffusion occurs in the direction perpendicular to the flow direction, yielding an increase of the plastic strain in the mid-plane and a decrease of the plastic strain at the outer fibers (dashed flat line). The difference in equivalent plastic strain graphs of Figure 4-6, obtained with the three convection schemes, shows this effect of numerical diffusion. The equivalent plastic strain curves, given in Figure 4-5, are recorded at a node lying in the mid-plane of the blank. Therefore, the orthotropic scheme and the $\kappa=1/3$ scheme lead to a smaller equivalent plastic strain than the isotropic scheme. Since numerical diffusion in the perpendicular direction is restricted for the orthotropic and the $\kappa=1/3$ scheme, they give a more accurate description of the equivalent plastic strain distribution over the thickness.

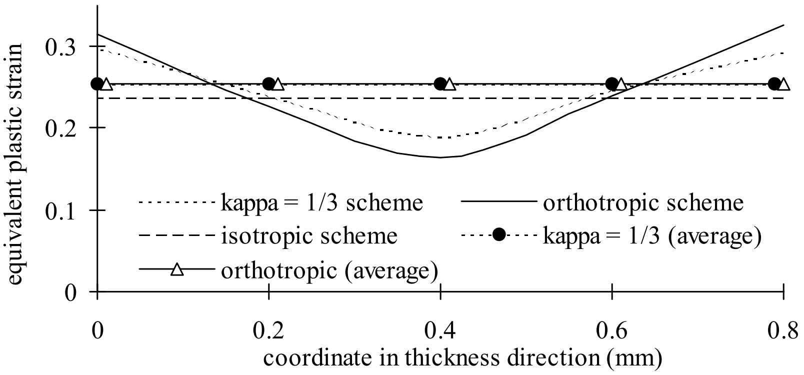

Figure 4-6. Equivalent plastic strain as a function of the position in blank thickness direction

The average equivalent plastic strain values for the orthotropic scheme and the κ=1/3 scheme are also depicted in Figure 4-6. The equivalent plastic strain for the isotropic scheme, recorded at the mid-plane, is significantly lower than the average equivalent plastic strain of these schemes. Note that the 2D plane strain drawbead model will serve as an input for the equivalent drawbead model in which it is only possible to prescribe the plastic strain over the total blank thickness. Therefore the equivalent plastic strain, recorded at the mid-plane, is not a reliable representation of the total plastic strain in the blank. For these schemes, an improved representation of the equivalent plastic strain over the total blank thickness can be obtained by averaging the equivalent plastic strain distributions at different positions in the blank thickness direction. Figure 4-7 depicts these averaged equivalent plastic strain distributions for the orthotropic and the κ=1/3 scheme, together with the plastic strain distribution for the isotropic scheme.

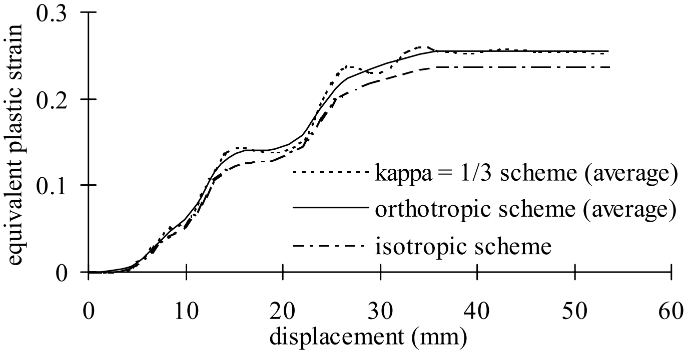

Figure 4-7. Averaged equivalent plastic strain curves as a function of the material displacement

It is concluded that the orthotropic convection scheme shows the best performance for 2D drawbead simulations. It does not show any oscillations and gives a reliable prediction of the plastic strain distribution over the thickness due to the absence of significant numerical diffusion in the direction perpendicular to the flow direction. When used in the equivalent drawbead model, the equivalent plastic strain distribution must be averaged at different positions across the blank thickness.

4.2.2 Analytical verification

Analytical models to determine the DBRF can provide a first insight into the performance of the 2D plane strain drawbead model. In this section, the results of a simple analytical model and a more sophisticated analytical model are compared with the results of the 2D plane strain drawbead model.

4.2.2.1 Simple analytical model

As a first orientation, the numerical 2D plane strain drawbead model is compared with a simple analytical model which includes a number of simplifications [Meinders, 1999]. A moment *M* per millimeter width is needed to bend a strip with thickness *t* along a radius *R*, see Figure 4-8.

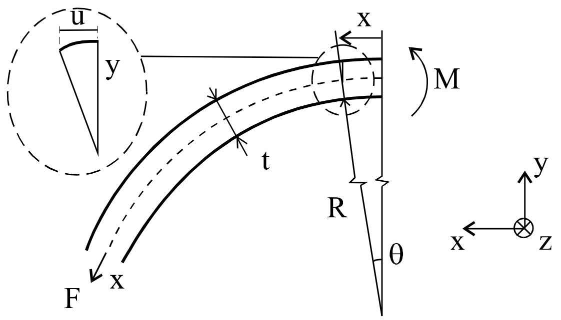

Figure 4-8. Principle outline for calculation of the bending force

Assuming a fully plastic moment and that the neutral plane coincides with the mid-plane, this moment can be written as:

$$M = 2\int_{0}^{\frac{1}{2}t} \sigma_x y dy \qquad (4\text{-}183)$$

The material is assumed to obey both the Ludwik-Nadai hardening law and the Von Mises yield criterion. Hence, the stress in the plane strain situation can be written as:

$$\sigma_{ps} = \tfrac{2}{\sqrt{3}} C\varepsilon^n \qquad \text{where} \qquad \varepsilon = \frac{u}{x} = \frac{y\theta}{\left(R + \frac{1}{2}t\right)\theta} \qquad (4\text{-}184)$$

Substitution of equation (4-184) into (4-183) gives:

$$M = \frac{4C}{\sqrt{3}\left(R + \frac{1}{2}t\right)^n} \frac{1}{n+2} \left(\tfrac{1}{2}t\right)^{n+2} \qquad (4\text{-}185)$$

The force needed to bend the strip can be calculated by equating the internal and external work. The internal work yields:

$$W_{\text{int}} = \int\int \sigma\varepsilon dA = \int\int \sigma\kappa y dA = 2\kappa\int \int_{0}^{\frac{1}{2}t} \sigma y dy dx = M\kappa\left(R + \tfrac{1}{2}t\right)\int_{0}^{\theta} d\alpha = M\theta \qquad (4\text{-}186)$$

where curvature $\kappa = \dfrac{1}{R + \frac{1}{2}t}$ and strain $\varepsilon = \kappa y$.

The external work is given by:

$$W_{ext} = Fx \tag{4-187}$$

The force per millimeter width can be calculated by equating equations (4-186) and (4-187):

$$F = \frac{M\theta}{x} = \frac{4C}{\sqrt{3}\left(R + \frac{1}{2}t\right)^{n+1}} \frac{1}{n+2} \left(\tfrac{1}{2}t\right)^{n+2} \tag{4-188}$$

To compare the 2D drawbead model with this simple analytical model, a specific drawbead geometry is chosen. The clearance is 0.7 mm which equals the blank thickness. The material model applied here is ideal plastic with a C-value of 149 MPa and a hardening exponent of 0.0, and friction is neglected. Within this drawbead with a semicircular cross-section the material will be bent and sequentially unbent two times around a radius of 3 mm and once around a radius of 8 mm. When the sheet thinning is neglected, the total Drawbead Restraining Force (DBRF) will be:

$\text{DBRF}_{\text{analytical}} = 30.21$ N/mm.

The DBRF calculated with the 2D plane strain drawbead model amounts to:

$\text{DBRF}_{\text{simulation}} = 26.50$ N/mm.

Taking into account that the analytical solution is an upper bound criterion due to the incorporated simplifications, it can be concluded that the DBRF calculated with the 2D plane strain drawbead model is a reasonable prediction of the real DBRF.

4.2.2.2 Stoughton model

A frequently used and more sophisticated analytical model to determine the DBRF is proposed by Stoughton [Stoughton, 1988]. The Stoughton model is based on the virtual work principle and makes use of the effective material bending radius instead of the drawbead radii. In this model, the forces are derived by equating the work required to pull the sheet through the drawbead to the work required to bend and straighten the sheet and overcome the frictional forces in sliding over the bead radii. The DBRF results from the accumulation of bending and frictional forces from various regions of the drawbead. The material is assumed to obey the Holomon hardening law which incorporates strain rate sensitivity. This hardening law degenerates to the Ludwik-Nadai hardening law when strain rate effects are neglected.

The analytical formulation of the DBRF is given by equation (4-189). For the derivation of this equation and its components, the reader is referred to [Stoughton, 1988].

$$DBRF = \left(\left(F_1 e^{\mu\theta} + \mu F_e + F_2 + F_3\right) e^{2\mu\theta} + \mu F_e + F_4 + F_5\right) e^{\mu\theta} + F_6 \tag{4-189}$$

First, virgin material with a given initial thickness enters the drawbead from the right in Figure 4-9 and is bent along the first contra-bead radius R4, resulting in a bending force F_1. Due to sliding over the contra-bead radius, this force is increased by a factor $e^{\mu\theta}$, where θ is the angle of contact between the sheet and the contra-bead radius and μ is the friction coefficient. Since the model accounts for initial elastic displacements due to the closing of the drawbead, an additional friction force due to this elastic displacement acts at the point of contact at the contra-bead entrance radius with size $\mu F_e/2$. Here F_e is the elastic normal force.

The additional restraining force F_2 to unbend the sheet at the contra-bead radius R4 is calculated, taking sheet thinning and strain changes into account due to the first bend. Then the sheet is re-bent in the opposite direction at the bead radius R2. Following this strategy for the entire drawbead yields the above analytical formulation for the DBRF.

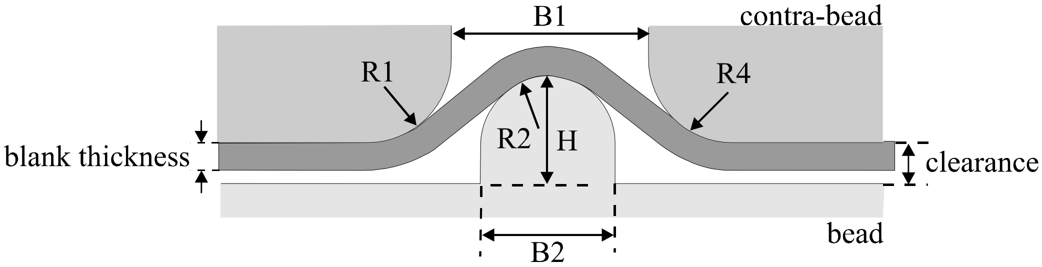

Figure 4-9. Drawbead geometry

An identical strategy is used to derive an analytical formulation for the lift force. This force appears when material is pulled through the drawbead and its direction is opposite to the blankholder force.

The performance of the Stoughton model and the 2D plane strain drawbead model will be compared for three different drawbead geometries, see Table 4-1. The steady state values of the 2D plane strain drawbead model for the DBRF and the lift force are given in Table 4-2 together with the analytical results.

Geometry (mm)	drawbead 1	drawbead 2	drawbead 3
R1, R4	3	3	3
R2	5	5	8
H	8	5	12
B1	13.6	13.6	20
B2	10	10	16
blank thickness	0.7	0.7	0.7
clearance	0.7	0.7	0.9

Table 4-1. Drawbead dimensions

		Stoughton (N/mm)	2D model (N/mm)	difference (%)
drawbead 1	DBRF	72.9	78.7	7.4
	Lift force	60.9	72.9	16.5
drawbead 2	DBRF	62.7	59.8	-4.9
	Lift force	50.7	68.2	25.7
drawbead 3	DBRF	69.7	82.7	15.7
	Lift force	58.8	72.0	18.3

Table 4-2. DBRF and lift force for Stoughton model and 2D drawbead model

The DBRF for drawbead 1 and drawbead 2 compare very well, however a greater deviation between the calculated results is seen for drawbead 3. The explanation for this phenomenon lies in the way the material follows the drawbead geometry. For drawbead 1 and drawbead 2 the cavity between the contra-bead and the bead (B1-B2, see Figure 4-9) is narrow and the clearance between the tools equals the blank thickness. This means that the blank is forced to mainly follow the drawbead geometry, see Figure 4-10a. Note that for clarity only the mid-plane of the deformed blank is plotted. The analytical Stoughton model is based on this type of deformation patterns and hence the agreement between the analytical results and the simulation results will be good. However, for drawbead 3, the cavity between the contra-bead and the bead is large and the clearance between the tools is larger than the blank thickness. As a result, the deformed blank shape will look like Figure 4-10b. The analytical Stoughton model is not able to deal accurately with this type of deformation pattern, which explains the larger deviation between the analytical DBRF and the DBRF obtained with the 2D drawbead model.

The difference in the calculated lift force is around 20% between both models for all drawbead geometries. Stoughton already observed a moderate difference between the analytically and the experimentally determined lift forces but did not explain this difference.

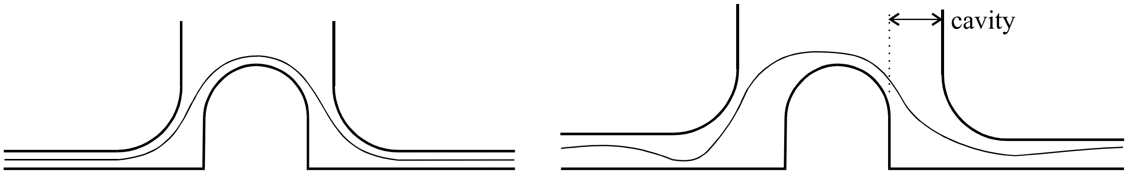

(a) drawbead with narrow cavity and clearance (b) drawbead with large cavity and clearance

Figure 4-10. Deformed blank shape in different drawbeads

4.2.3 Experimental verification

An experimental setup was designed and built to validate the performance of the 2D plane strain drawbead model. The experiments were performed at Hoogovens Steelworks on a fully equipped Erichsen press [Drent, 1993]. A principle outline of this experimental setup is given in Figure 4-11. A strip of sheet material is clamped between a blankholder and a die. The drawbead is situated in the blankholder - die region. The material is pulled through the drawbead by moving the punch into the die cavity.

The experimental results and numerical results will be compared for drawbead 3, see Table 4-1. The die shoulder radius R5 is 5 mm. The used sheet material has a C-value of 551 MPa, a hardening exponent of 0.23 and the yield stress is 149 MPa. The sheet metal is lubricated on both sides with a deep drawing oil with a viscosity of 0.04 Pa·s at 20 ºC. The surface roughness of the tools is about 25 μm. The punch speed is kept constant at 3 mm/s. The sheet width is set at 50 mm. The friction coefficient for the numerical simulation is set at 0.13 according to the experiment.

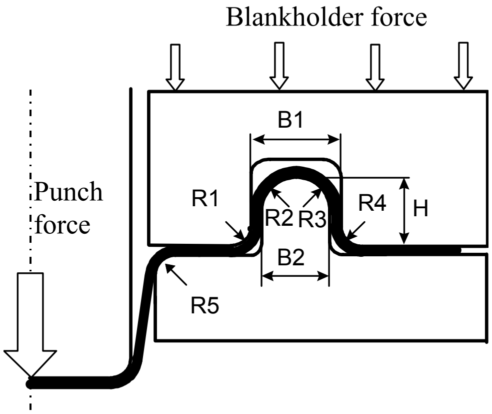

Figure 4-11. Experimental setup of the drawbead tester

The DBRF is recorded at the exit of the drawbead, see Figure 4-3. To avoid an enormous increase in the computation time, the punch rounding is not modeled in the 2D plane strain drawbead model, since it will not significantly affect the results. The calculated DBRF needed to pull the sheet through the drawbead is shown in Figure 4-12 as a function of the material displacement. The DBRF appears to be history dependent, its value is a function of the amount of material which has already passed the drawbead. The punch force is recorded during the course of the experiment and is also shown in Figure 4-12. The stationary value of the measured punch force is 106 N/mm which agrees well with the stationary value of the calculated DBRF. The large deviation between experiment and simulation for small displacements is a result of the difference between the experimental setup and the 2D drawbead model. During the experiment the sheet is initially flat and is bent around the die shoulder (R5, see Figure 4-11) when the punch moves downwards. This means that during the experiment the effective die bending radius will decrease from infinite (initial flat situation) to approximately the die shoulder radius (end of punch stroke), yielding a smooth increase of the bending force. However, in the 2D plane strain drawbead simulation the sheet is initially modeled along the die shoulder radius (see Figure 4-3), yielding a maximum bending force at the die shoulder radius when the simulation is started.

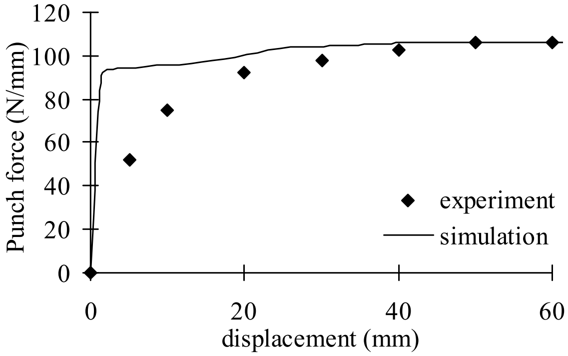

Figure 4-12. Drawbead restraining force as a function of the displacement

The plastic thickness strain in the sheet is calculated comparing the initial thickness with the final thickness and is depicted in Figure 4-13 as a function of the coordinate distance 's' in the drawbead, see Figure 4-3. The plastic thickness strain is also history dependent. Due to the plane strain assumption and the nearly incompressible material behavior the magnitude of the plastic thickness strain is almost equal to the magnitude of the tangential strain. The plastic thickness strain, derived from the measured thickness after drawbead processing and the initial thickness, is also given in Figure 4-13 as a function of the coordinate distance in the drawbead. The experimentally determined plastic thickness strain agrees well with the simulation result.

Since the lift force was not recorded during the course of the experiment, the simulated lift force cannot be compared with the experimental data and is therefore not considered in this section.

The good agreement between the experimental data and numerical simulations provides sufficient evidence for the reliability of the 2D plane strain drawbead model in predicting the DBRF and the plastic thickness strain. Comparisons of simulation and experimental results for other drawbead geometries also show good agreement [Carleer, 1997], [Pelgrim, 1997]. Having demonstrated the reliability of the 2D plane strain drawbead model, it can be used to accurately determine the process dependent drawbead forces and strains for all possible drawbead geometries.

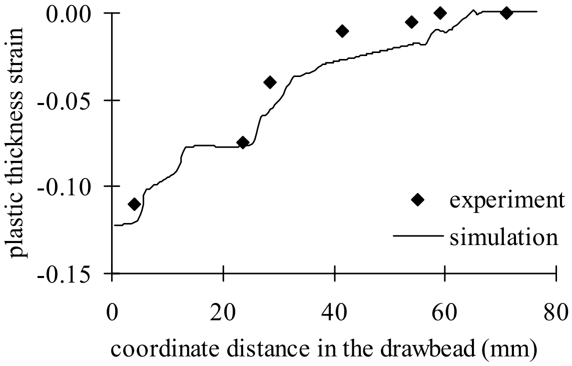

Figure 4-13. Plastic thickness strain as a function of the coordinate distance

4.2.4 Preparation of the results for the purpose of the equivalent drawbead model

The results as generated with the 2D drawbead model need to be modified in order to be used as an input for the equivalent drawbead model because of the following two reasons. Firstly, the experiments were performed including a die shoulder radius R5, see Figure 4-11, since it was not possible to build an experimental setup without a die shoulder radius. However, the die radius R5 contributes to both the DBRF and the plastic thickness strain. The measured and simulated values should therefore be corrected for this additional contribution. This was done by performing a simulation in which the die shoulder radius was absent to generate the modified DBRF and the plastic thickness strain.

Secondly, the plastic thickness strain as given in Figure 4-13 is represented as a function of the position along the drawbead in order to compare the simulation results with the experimental data. Since in deep drawing simulations the drawbead will be represented as a line in the equivalent drawbead model, the position in the drawbead is not known. Therefore the plastic thickness strain is also calculated as a function of the material displacement to serve as an input parameter for the equivalent drawbead.

The modified results of the 2D plane strain drawbead model to be used in the equivalent drawbead model are given in Figure 4-14.

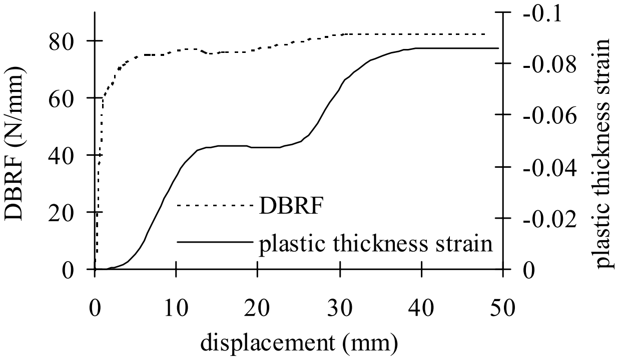

Figure 4-14. DBRF and plastic thickness strain obtained with the 2D drawbead model

An almost flat plateau, situated between 15 mm and 25 mm displacement, can be distinguished in both graphs of the drawbead characteristics. This phenomenon can be explained with the help of Figure 4-3. At position *A* the material is bent with a certain curvature and, up to position *A'*, the sheet will follow the same curvature. Hence, the material undergoes no additional bending deformation in the region between *A* and *A'* which results in the almost flat plateau in the graphs. For this specific drawbead configuration the steady state is reached after 37 mm material displacement. The steady state value for the DBRF reads 83 N/mm and for the plastic thickness strain -0.086.

4.3 Equivalent drawbead model

The purpose of an equivalent drawbead model is to replace the real drawbead to avoid a drastic increase in computation time for deep drawing simulations without significant loss of accuracy. Furthermore, the equivalent drawbead model has more advantages compared to the use of the real drawbead geometry. First, the equivalent drawbead is a flexible design tool. The effect of varying the position or geometry of the drawbead on the material flow can be studied very easily without the necessity to adapt the CAD drawings for a variation in the position or geometry of the real drawbead. Second, sheet metal forming processes are generally simulated with plate or shell elements for which a plane stress assumption is made. This assumption applies when the bending radii are large compared to the sheet thickness. However, the radii of a drawbead are usually very small and as a result the plane stress assumption is not valid when the material traverses the drawbead. In contrast, the equivalent drawbead model incorporates the results of the 2D plane strain drawbead model which are determined without the plane stress assumption.

The equivalent drawbead model, represented as a line on the tool surface, is given in Figure 4-15. During the deep drawing simulation a finite element which passes the drawbead line will obtain an additional DBRF and a plastic thickness strain whilst the lift force is subtracted simultaneously from the total blankholder force.

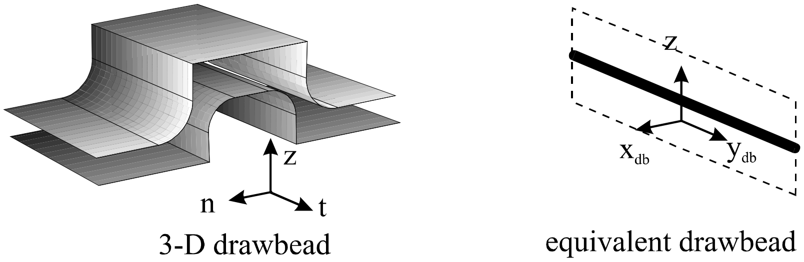

Figure 4-15. Schematic drawing of a 3-dimensional drawbead and its equivalent drawbead representation

The material flow in the normal direction *n* only causes a DBRF and plastic thickness strain whilst the tangential component *t* makes no contribution, see Figure 4-15 [Carleer, 1996]. This supports the approach to separate the total material flow into a normal and a tangential component. Consequently, only the normal component of the material flow will be taken into account for the equivalent drawbead model. The coordinate system for the equivalent drawbead model is also given in Figure 4-15, where x_{db} and y_{db} denote the directions normal and tangential to the drawbead, respectively. The y_{db}-axis is the plane strain direction of the 2D-drawbead analysis.

The input of the equivalent drawbead model consists of a drawbead restraining force, a plastic thickness strain and a lift force. The implementation of these drawbead characteristics in the equivalent drawbead model are treated separately in the following sections. Combining the derived expressions for the separate drawbead characteristics completes the equivalent drawbead model. The implementation of the lift force is described in Section 4.3.1, the implementation of the drawbead restraining force in Section 4.3.2. Two different mathematical descriptions of the implementation of the plastic thickness strain are described in Section 4.3.3. The performance of both strain algorithms are compared in Section 4.3.4.

4.3.1 Implementation of the lift force

The direction of the lift force, which appears when the material is pulled through the drawbead, is opposite to the blankholder force direction. This lift force causes a rise of the entire blankholder from which it can be concluded that the drawbead lift force is not a local phenomenon but will affect the total deep drawing process. The lift force is therefore subtracted from the total blankholder force during the deep drawing simulation.

4.3.2 Implementation of the drawbead restraining force

The drawbead restraining force appears on an element when this element passes the drawbead line. The direction of the DBRF is opposite to the material flow with the restriction that it acts perpendicular to the drawbead line. The DBRF is taken into account as an additional body force in the set of the finite element equations:

$$\underline{K} \cdot \Delta \boldsymbol{u} = \boldsymbol{f} - \boldsymbol{r}_0 + \boldsymbol{f}_{dbrf} \qquad (4\text{-}190)$$

Here $\underline{K}$ is the stiffness matrix and $\Delta \boldsymbol{u}$ is the incremental displacement vector. The vectors on the right-hand side, $\boldsymbol{f}$ and $\boldsymbol{f}_{dbrf}$, denote the force vector and the additional drawbead restraining force vector, respectively. The vector $\boldsymbol{r}_0$ is the initial reaction force.

The force $\boldsymbol{f}_{dbrf}$ is assigned to the element nodes which already passed the equivalent drawbead and equals the integral of the DBRF per unit width f_{db} over the width w_i:

$$\boldsymbol{f}_{dbrf} = \int_{w_i} f_{db} \mathrm{d}s \qquad (4\text{-}191)$$

where w_i is the projected element side length on the equivalent drawbead line, see Figure 4-16.

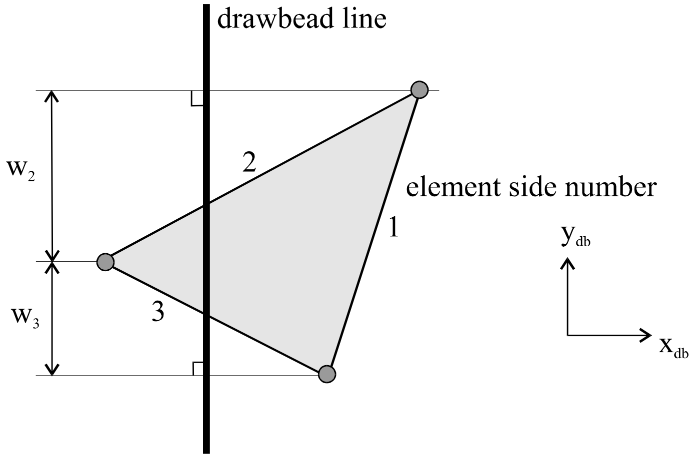

Figure 4-16. Projected element side length w_i

4.3.3 Implementation of the plastic thickness strain

Two different algorithms were examined to implement the plastic thickness strain in the equivalent drawbead model. The first algorithm is based on a stress estimate, the second algorithm is based on a penalty constraint method. Note that in this chapter stresses and strains are regarded as invariant tensors, as introduced in Chapter 2. The asterisks, denoting the invariant form, will be dropped for convenience.

4.3.3.1 Stress estimate

The first algorithm to implement the plastic thickness strain is based on the change in stress state because of the prescribed drawbead strain. An extra stiffness term is added to the left-hand side of the finite element equations at the element level, which appears as the drawbead stiffness matrix $\underline{K}_{db}$ [Carleer, 1997], [Meinders, 1996]:

$$\left(\underline{K} + \underline{K}_{db}\right) \cdot \Delta \boldsymbol{u} = \boldsymbol{f} - \boldsymbol{r}_0 \tag{4-192}$$

The drawbead stiffness matrix can be written in terms of drawbead stresses and appears as an extra drawbead force vector in the right-hand side of the finite element equations:

$$\underline{K} \cdot \Delta \boldsymbol{u} = \boldsymbol{f} - \boldsymbol{r}_0 + \int\limits_V \underline{\underline{\boldsymbol{B}}}^t : \Delta \underline{\sigma}_{db} dV \tag{4-193}$$

where $\Delta\underline{\sigma}_{db}$ is the incremental drawbead stress tensor to be estimated and $\underline{\underline{\boldsymbol{B}}}^t$ is a third order tensor containing the gradient of the shape functions. The drawbead stress $\Delta\underline{\sigma}_{db}$ has to be estimated to solve equation (4-193) and can be determined with the help of the incremental elastoplastic constitutive equation [Vreede, 1992]:

$$\Delta \underline{\sigma}_{db} = \left(\underline{\underline{E}} - (1-h)\underline{\underline{Y}}\right) : \Delta \underline{\varepsilon}_{db} \tag{4-194}$$

where $\Delta\underline{\varepsilon}_{db}$ is the incremental drawbead strain tensor, $\underline{\underline{E}}$ is the elasticity tensor, $\underline{\underline{Y}}$ is the yield tensor and h is the hardening rate. Equation (4-194) can be solved when $\underline{\underline{E}}$, $\underline{\underline{Y}}$ and h are known and when sufficient boundary conditions are incorporated.

Boundary conditions

Three assumptions are made with respect to boundary conditions. First, tangential to the equivalent drawbead, a plane strain condition is assumed, see Figure 4-17. Since a plane strain situation is assumed in the y_{db}-direction the material will only elongate in the x_{db}-direction due to the prescribed drawbead strain. Second, the blank thickness is very small compared to the other blank dimensions, and therefore a plane stress state can be assumed. Third, the shear stress in the x_{db}-y_{db} plane is neglected, since only the direction of the material flow normal to the drawbead line contributes to the drawbead force and strain.

Summarizing, the boundary conditions can be expressed as:

$$\begin{aligned} &\Delta\varepsilon_{db\_y} = 0 \\ &\Delta\varepsilon_{db\_z} = \Delta\varepsilon_{pr\_thick} \\ &\Delta\sigma_{db\_z} = \Delta\sigma_{db\_xz} = \Delta\sigma_{db\_yz} = 0 \\ &\Delta\sigma_{db\_xy} = 0 \end{aligned} \tag{4-195}$$

where $\Delta\varepsilon_{pr\_thick}$ is the incremental prescribed plastic thickness strain. With these boundary conditions, equation (4-194) reduces to a system of three equations with two unknown stress components, $\Delta\sigma_{db\_x}$ and $\Delta\sigma_{db\_y}$, and one unknown strain component, $\Delta\varepsilon_{db\_x}$.

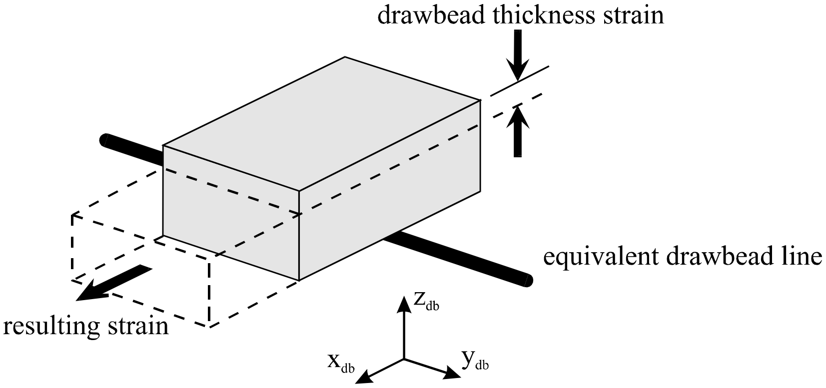

Figure 4-17. Graphic representation of the plane strain condition

Elasticity tensor

When the stress tensor $\Delta\underline{\sigma}_{db}$ and the strain tensor $\Delta\underline{\varepsilon}_{db}$ are written as vectors, the tensor $\underline{\underline{E}}$ can be written as a matrix. For isotropic material behavior the components of the elasticity matrix $\underline{\underline{E}}$ are:

$$\underline{\underline{E}} = \begin{bmatrix} 2G+\lambda & \lambda & \lambda \\ \lambda & 2G+\lambda & \lambda \\ \lambda & \lambda & 2G+\lambda \end{bmatrix} \tag{4-196}$$

where the shear modulus G and λ are the Lamé constants. The matrix is reduced to a 3*3 matrix since it is assumed that no additional shearing will occur in the drawbead.

Yield tensor

The following expression for the yield tensor $\underline{\underline{Y}}$ with associated yielding holds:

$$\underline{\underline{Y}} = \frac{\underline{\underline{E}} : \frac{\partial\phi}{\partial\underline{\sigma}} \frac{\partial\phi}{\partial\underline{\sigma}} : \underline{\underline{E}}}{\frac{\partial\phi}{\partial\underline{\sigma}} : \underline{\underline{E}} : \frac{\partial\phi}{\partial\underline{\sigma}}} \tag{4-197}$$

where ϕ is the yield function. To determine the components of the yield tensor, the drawbead strains are assumed to be totally plastic. This is allowed since the elastic part of the drawbead strains is negligibly small. Because of the plastic incompressibility and the plane strain assumption in the y_{db}-direction, for small displacement increments the strain increments satisfy the linear relation:

$$\Delta\varepsilon_{db\_x} = -\Delta\varepsilon_{db\_z} \tag{4-198}$$

The plastic deformation satisfies the normality flow rule according to Drucker. With this flow rule an expression for the stress derivatives of the flow criterion is found:

$$\underline{\dot{\varepsilon}}^p = \dot{\lambda}\frac{\partial\phi}{\partial\underline{\sigma}} \Rightarrow \frac{\partial\phi}{\partial\sigma_{db\_x}} = -\frac{\partial\phi}{\partial\sigma_{db\_z}} \tag{4-199}$$

where $\dot{\lambda}$ is the plastic multiplier and ϕ is the yield function. Writing the yield tensor $\underline{\underline{Y}}$ as a matrix and using equation (4-199), the numerator of equation (4-197) can be written as:

$$\underline{\underline{E}}:\frac{\partial\phi}{\partial\underline{\sigma}}\frac{\partial\phi}{\partial\underline{\sigma}}:\underline{\underline{E}} = \begin{bmatrix} \Psi & 0 & -\Psi \\ 0 & 0 & 0 \\ -\Psi & 0 & \Psi \end{bmatrix} \tag{4-200}$$

where:

$$\Psi = 4 \cdot G^2\left(\frac{\partial\phi}{\partial\sigma_{db\_x}}\right)^2 \tag{4-201}$$

Working out the denominator of the yield matrix yields:

$$\frac{\partial\phi}{\partial\underline{\sigma}}:\underline{\underline{E}}:\frac{\partial\phi}{\partial\underline{\sigma}} = 4 \cdot G\left(\frac{\partial\phi}{\partial\sigma_{db\_x}}\right)^2 \tag{4-202}$$

Using equations (4-200) and (4-202), an expression is found for the yield matrix $\underline{Y}$ in which the yield matrix only depends on the shear modulus G:

$$\underline{Y} = \begin{bmatrix} G & 0 & -G \\ 0 & 0 & 0 \\ -G & 0 & G \end{bmatrix} \tag{4-203}$$

Hardening rate

An expression for the hardening rate is defined, see equation (2-59):

$$h = \frac{f}{f - \frac{\partial\phi}{\partial\underline{\sigma}}:\underline{\underline{E}}:\frac{\partial\phi}{\partial\underline{\sigma}}} \tag{4-204}$$

where, for the Hill'48 yield criterion:

$$f = -4(R+1)^2\sigma_y^2\frac{\partial\sigma_y}{\partial\varepsilon} \tag{4-205}$$

where R is the anisotropy parameter, σ_y is the yield stress and ε is the equivalent strain. The hardening rate is calculated using the stress state of the previous step.

Using equations (4-196), (4-203) and (4-204) and the boundary conditions (2-1), the incremental elastic plastic constitutive equation can be solved with respect to the unknown drawbead stress and strain components. Substitution of the drawbead stress tensor into equation (4-193) completes the implementation of the drawbead thickness strain based on stress estimate.

4.3.3.2 Penalty constraint method

The second algorithm to add an additional plastic thickness strain in the equivalent drawbead model is based on a penalty constraint method. An extra stiffness term $\underline{Kc}_{db}$ and an extra force vector $\boldsymbol{fc}_{db}$ are therefore added to the finite element equations at the element level [Meinders, 1998a]:

$$\left(\underline{K} + \underline{Kc}_{db}\right) \cdot \Delta \boldsymbol{u} = \boldsymbol{f} - \boldsymbol{r}_0 + \boldsymbol{fc}_{db} \tag{4-206}$$

The drawbead stiffness matrix $\underline{Kc}_{db}$ and the drawbead constraint force vector $\boldsymbol{fc}_{db}$ will be derived using a constraint method. As mentioned before, only the component of the material flow normal to the drawbead line will be taken into account for the equivalent drawbead model, see Figure 4-18.

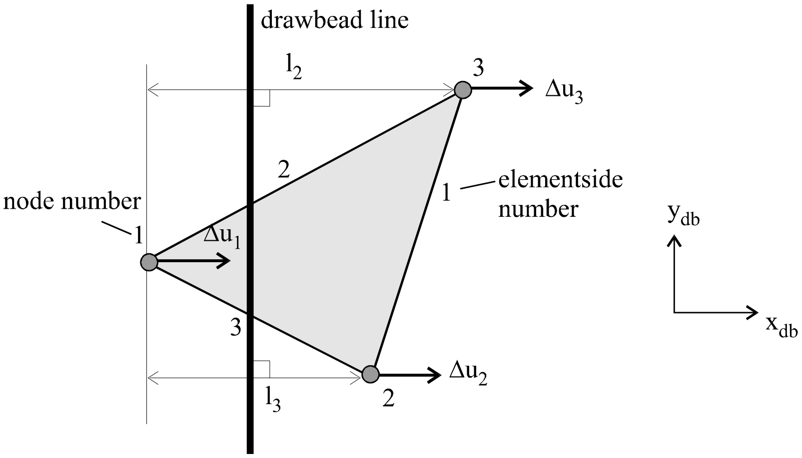

Figure 4-18. Element geometry configuration

The constraint equations will be derived for the element depicted in Figure 4-18. The nodes and the element sides are numbered arbitrarily. The element side lengths projected on the normal of the drawbead line are represented by l_i. A set of constraint equations can be defined for this element:

$$\begin{bmatrix} -1 & 1 & 0 \\ -1 & 0 & 1 \end{bmatrix} \cdot \begin{Bmatrix} \Delta u_1 \\ \Delta u_2 \\ \Delta u_3 \end{Bmatrix} = \begin{Bmatrix} \Delta l_3 \\ \Delta l_2 \end{Bmatrix} \qquad \Rightarrow \qquad \underline{A} \cdot \Delta \underline{u} = \underline{q} \tag{4-207}$$

The elongation of the element side Δl_i is given by:

$$\Delta l_i = \frac{\Delta \varepsilon_{pr\_thick} \cdot l_i^{init}}{m} \tag{4-208}$$

where $\Delta \varepsilon_{pr\_thick}$ is the prescribed drawbead strain and l_i^{init} the perpendicular element side length in the first iteration. The variable m represents the number of steps required for the entire element to pass over the drawbead. The least squares method is applied to transform the constraint equation into a matrix form:

$$\left(\underline{A} \cdot \underline{u} - \underline{q}\right)^2 = minimum \qquad \Rightarrow \qquad \frac{\partial}{\partial u}\left(\underline{A} \cdot \underline{u} - \underline{q}\right)^2 = 0 \Rightarrow \underline{A}^T \underline{A} \cdot \underline{u} = \underline{A}^T \underline{q} \tag{4-209}$$

Multiplying the combination of equations (4-207) and (4-209) with a penalty factor k yields:

$$k \cdot \begin{bmatrix} 2 & -1 & -1 \\ -1 & 1 & 0 \\ -1 & 0 & 1 \end{bmatrix} \cdot \begin{Bmatrix} \Delta u_1 \\ \Delta u_2 \\ \Delta u_3 \end{Bmatrix} = k \cdot \begin{Bmatrix} -\Delta l_3 - \Delta l_2 \\ \Delta l_3 \\ \Delta l_2 \end{Bmatrix} \tag{4-210}$$

The left-hand side of the above equation represents the symmetric drawbead stiffness matrix $\underline{Kc}_{db}$, whereas the right-hand side represents the drawbead constraint force $\boldsymbol{fc}_{db}$. In shorthand notation, equation (4-210) reads:

$$\underline{Kc}_{db} \cdot \Delta \boldsymbol{u} = \boldsymbol{fc}_{db} \tag{4-211}$$

The penalty factor k is necessary to create a drawbead stiffness matrix in which the components are of the same order of magnitude as the components in the element stiffness matrix. The penalty factor must be large enough to describe the drawbead behavior properly. However, it may not be too large since otherwise it will dominate the solution of the total system. Therefore, the value of the multiplier k is related to the largest value of the element stiffness matrix.

Convergence of the global weak equilibrium is generally not reached in one iteration. If the mechanical unbalance does not satisfy the required accuracy after the first iteration, the incremental displacement vector is recalculated in an iterative process until the desired accuracy has been reached. The drawbead stiffness matrix remains constant during this iteration process, but the right-hand side of the finite element equations at the element level changes to:

1^{st} *iteration* (4-212)

$$\left(\underline{K} + \underline{Kc}_{db}\right) \cdot \Delta \boldsymbol{u} = \boldsymbol{f}^{\#1} - \boldsymbol{r}_0$$

$$\text{with} \qquad \boldsymbol{f}^{\#1} = \boldsymbol{f} + \boldsymbol{fc}_{db}$$

n^{th} *iteration*

$$\left(\underline{K} + \underline{Kc}_{db}\right) \cdot \Delta\Delta \boldsymbol{u}^n = \boldsymbol{f}^{\#n} - \boldsymbol{r}^{n-1}$$

$$\text{with} \qquad \boldsymbol{f}^{\#n} = \boldsymbol{f}^{\#n\text{-}1} + \Delta \boldsymbol{fc}_{db}^n$$

where $\boldsymbol{r}^{n-1}$ is the reaction force vector from the previous iteration. The drawbead constraint forces during the iteration process are given by:

1^{st} *iteration* (4-213)

$$\underline{fc}_{db} = k \cdot \begin{Bmatrix} -\Delta l_3 - \Delta l_2 \\ \Delta l_3 \\ \Delta l_2 \end{Bmatrix}$$

n^{th} *iteration*

$$\Delta \underline{fc}_{db}^n = k \cdot \begin{Bmatrix} -\Delta\Delta l_3^n - \Delta\Delta l_2^n \\ \Delta\Delta l_3^n \\ \Delta\Delta l_2^n \end{Bmatrix}$$

The prescribed elongation in the n^{th} iteration is represented by $\Delta\Delta L_i^n$ and depends on the elongation already obtained in the previous iterations Δl_i^{n-1}:

$$\Delta\Delta l_i^n = \Delta l_i - \Delta l_i^{n-1} \tag{4-214}$$

Note that the expressions derived for the drawbead stiffness matrix and the drawbead constraint force vector are defined in the local drawbead coordinate system. To add equation (4-211) to the finite element equations at the element level, the drawbead coordinate system has to be rotated towards the element coordinate system through a rotation matrix. Doing this completes the implementation of the drawbead thickness strain based on a penalty constraint method.

4.3.4 Comparison between the two drawbead strain algorithms

A deep drawing simulation of a rectangular product was carried out to compare the drawbead strain algorithm based on a stress estimate and the algorithm based on a penalty constraint method. The setup for this simulation is described in Section 4.4. A drawbead with the geometry of drawbead 1 (see Table 4-1, Section 4.2.2.2) is placed on the long side of the product. The steady state value of the DBRF is 82.7 N/mm and the steady state value of the plastic thickness strain is -0.086. Three simulations were performed. In one simulation only the DBRF was prescribed, whilst in the other two simulations both the DBRF and the plastic thickness strain were prescribed, using the different drawbead strain algorithms. For all the simulations, the plastic thickness strain in the rectangular product is given in Figure 4-19 as a function of the coordinate distance along the y-axis. The equivalent drawbead line is situated at a coordinate distance of 197 mm.

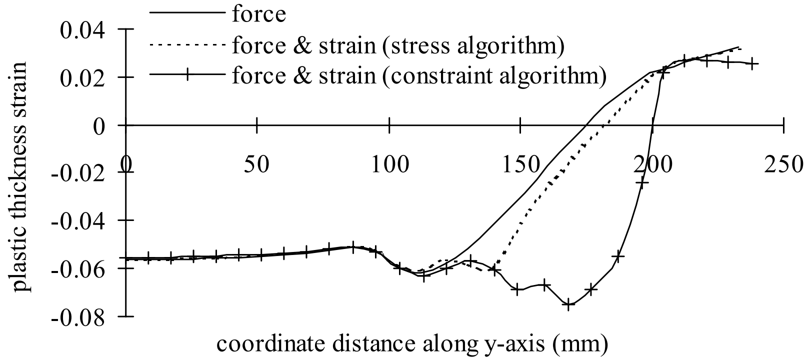

Figure 4-19. Thickness strain distribution along the y-axis

The result of the simulation in which the DBRF and the drawbead strain based on stress estimate are implemented, is almost identical to the result obtained with the simulation in which only the DBRF is prescribed. Consequently, it can be concluded that the implementation of the drawbead strain based on stress estimate hardly affects the plastic thickness strain distribution in the product. Implementing the drawbead strain based on the penalty constraint method does significantly affect the thickness strain distribution in the blank. The plastic thickness strain distribution under the punch (0 - 100 mm) is almost identical to the strain distribution when only a DBRF is prescribed. However, a clear difference in the thickness strain distribution between the two simulations can be seen in the material which has passed the equivalent drawbead. The maximum thickness strain reaches -0.075 at a coordinate distance of 170 mm. At a coordinate distance of 180 mm the difference between the two simulations amounts to -0.073. The steady state value of the prescribed plastic thickness strain was -0.086. Hence it can be concluded that the plastic thickness strain in the material increases by almost the prescribed drawbead strain when the constraint algorithm is used in the equivalent drawbead model. Note that the increase in plastic thickness strain does not equal the prescribed plastic thickness strain due to the application of a penalty factor.

The differences between the results obtained using the different strain algorithms can be explained as follows. The simulations were performed with a mechanical unbalance criterion of 0.01 with a maximum of 5 iterations per incremental step. Since the convergence behavior of the stress algorithm was very bad, the unbalance criterion was set at 0.05. This is the main reason for the differences in the simulation results using the stress algorithm and the constraint algorithm. To achieve an unbalance criterion of 0.01 in the simulation based on stress estimate, more than 75 iterations per incremental step were necessary, yielding a slight increase in the plastic thickness strain. Consequently, the drawbead strain algorithm based on stress estimate is not efficient for deep drawing simulations due to the bad convergence behavior. Therefore, the drawbead strain algorithm based on the penalty constraint method is used in the equivalent drawbead model.

4.4 Applications

The equivalent drawbead model as described in Section 4.3 must be validated. For this, a numerical and an experimental verification were performed. The numerical verification consisted of a comparison between the simulation results of a strip test with an equivalent drawbead and a strip test in which the real drawbead geometry was modeled. The experimental verification consisted of a comparison between the simulation results and experimental data of the deep drawing of a rectangular product. Finally, the performance of the equivalent drawbead model was demonstrated by a deep drawing simulation of an automotive product.

4.4.1 Numerical verification

First, the performance of the equivalent drawbead model was verified by a strip drawing simulation. A simulation was performed in which the real drawbead geometry was modeled. In this simulation a fine mesh containing 1380 plate elements based on Mindlin theory was used [Carleer, 1997]. These elements can account for membrane-, bending-, and shear stresses. A simulation was performed in which the drawbead geometry was replaced by an equivalent drawbead model. For this simulation 600 plate elements based on Mindlin theory were used. A coarse mesh was used in the latter simulation since the real drawbead geometry was omitted. The finite element models of both simulations are shown in Figure 4-20.

The plastic thickness strain of the two simulations as a function of the coordinate distance along the strip is compared in Figure 4-21. It can be seen that the maximum reduction in thickness compares well for the two simulations. Some deviation between the simulations can be observed at the right side of Figure 4-21, which can be explained as follows. The equivalent drawbead line is situated at a coordinate distance of 110 mm. Once the steady state value of the prescribed drawbead strain is reached as the material traverses the drawbead line, every new element which passes the drawbead will be subjected to this steady state value. An element which has not yet passed the drawbead line is not subjected to the prescribed drawbead strain. As a result the plastic thickness strain drops from the prescribed drawbead strain value to zero within the length of one element. However, in the simulation with the real drawbead geometry an element is subjected to a bending and unbending process as it traverses the drawbead geometry. Hence, the developed plastic thickness strain in the element depends on the position within the drawbead. The real drawbead geometry is represented at the coordinate distance interval [110 - 140 mm]. This explains why in the real drawbead simulation the plastic thickness strain slightly decreases from its maximum value to zero at the coordinate distance interval [110 - 140 mm].

The small deviation between the two simulations at the left side of Figure 4-21 is due to the closing of the blankholder when the real drawbead geometry is modeled. The closing of the blankholder results in the development of some plastic strain in the drawbead region which slightly affects the strain distribution in the entire strip.

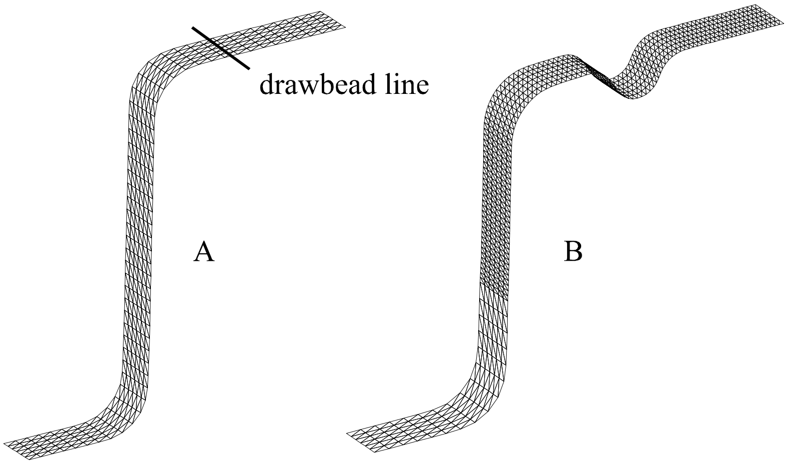

Figure 4-20. Finite element models of a strip drawing simulation with an equivalent drawbead (A) and with a real drawbead (B)

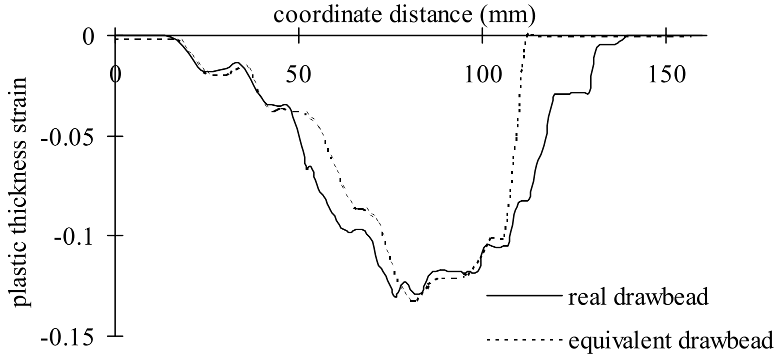

Figure 4-21. Plastic thickness strain distribution along the strip

4.4.2 Experimental verification

The equivalent drawbead model was also applied to the deep drawing simulation of a rectangular product using two different drawbead geometries. For verification the product was stamped to obtain experimental data. The dimensions of the two different drawbeads are listed in Table 4-1, drawbead 1 and drawbead 2 (Section 4.2.2.2), and the geometrical parameters are illustrated in Figure 4-9. The 2D plane strain drawbead model is used to determine the DBRF, the lift force and the plastic thickness strain of the two different drawbeads. The results obtained with the 2D drawbead model are given in Figure 4-22 for drawbead 1 and in Figure 4-23 for drawbead 2.

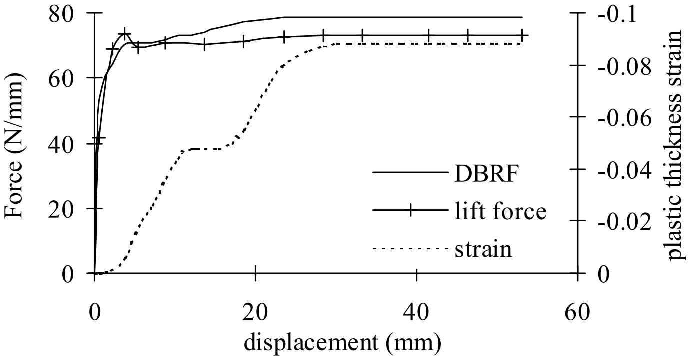

Figure 4-22. Drawbead 1 characteristics

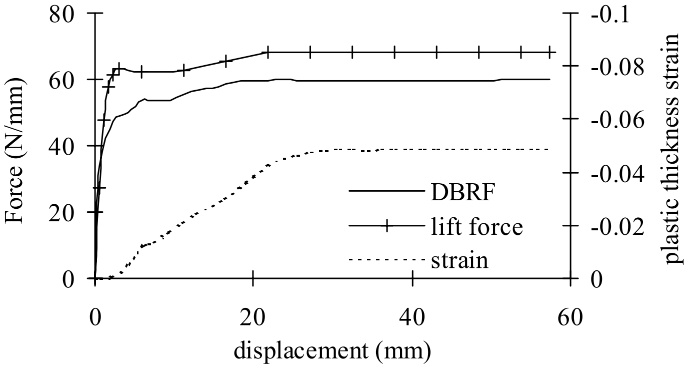

Figure 4-23. Drawbead 2 characteristics

The tool geometry for the rectangular product is given in Figure 4-24. The dimensions of the tools and the blank are listed in Table 4-3. Drawbeads with a length of 200 mm are placed in the die-blankholder region, both at a distance of 126.8 mm in the positive and negative y-directions.

Tool description	dimension (mm)
punch length	400
punch width	200
radius punch shoulder	20
radius punch corner	20
die length	403.6
die width	203.6
radius die shoulder	10
radius die corner	20
product depth	100

Blank description	dimension (mm)
blank length	600
blank width	470
blank thickness	0.7

Table 4-3. Tool and blank dimensions

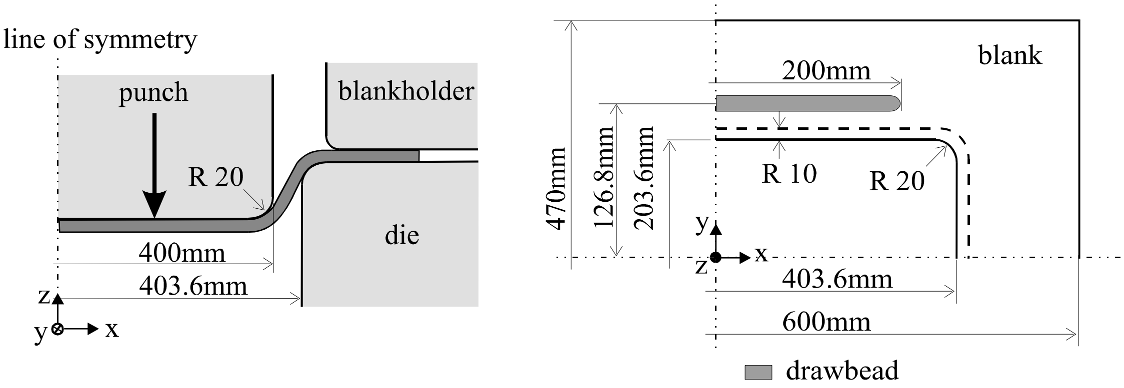

Figure 4-24. Tool geometry of the rectangular product

The blank is meshed with 4160 3-node triangular plate elements based on Mindlin theory with 5 integration points across the thickness. Contact between the sheet and the tools is described with contact elements in which a friction coefficient of 0.16 is assumed. The material behavior is assumed to be elastoplastic.

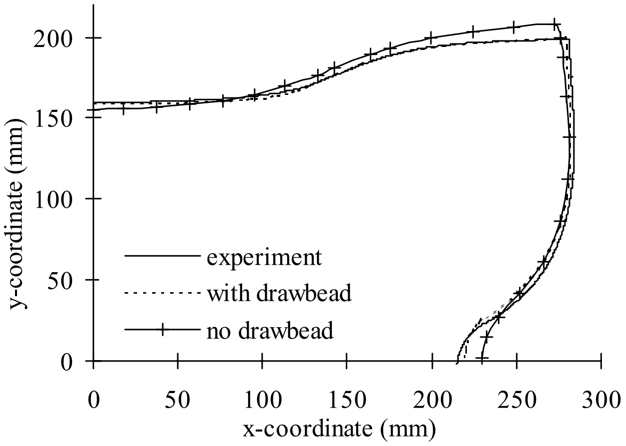

Figure 4-25. Flange shapes of rectangular product: drawbead 1

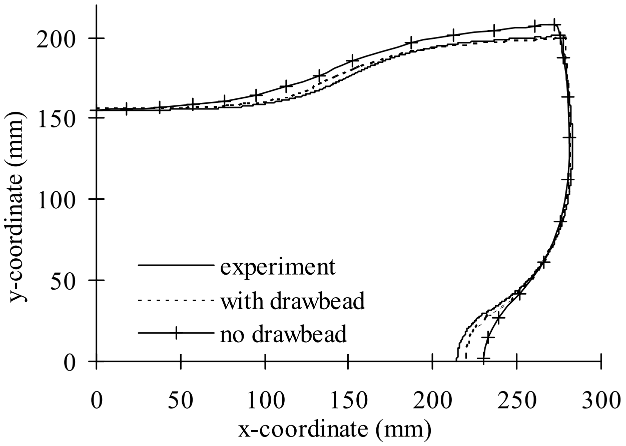

Figure 4-26. Flange shapes of rectangular product: drawbead 2

A set of simulations was performed for each of the two drawbead geometries to test the equivalent drawbead model. A set of simulations consists of a simulation without drawbeads and a simulation in which DBRF, the lift force and the plastic thickness strain are prescribed in the equivalent drawbead model.

The flange shapes obtained by the deep drawing simulations of the rectangular product after a punch stroke of 100 mm are given in Figure 4-25 for drawbead 1 and in Figure 4-26 for drawbead 2. The experimentally determined flange shapes for the rectangular products with different drawbeads are also shown in these figures.

The discussion of the results obtained will focus on the differences between the simulation with and without the equivalent drawbead model. For the simulation with drawbead 1 it can be seen that the draw-in at the drawbead position (0-100 mm x-coordinate) is significantly less when an equivalent drawbead model is used, which was also expected. It is also observed that the draw-in at other parts in the product is higher when an equivalent drawbead model is used. Since the material flow is restrained in the drawbead region, the material will flow more easily out of other regions into the die cavity, resulting in a higher draw-in in these regions. Consequently, the tip of the blank is rotated due to the change in the material flow pattern. The simulation with drawbead 2 also shows this behavior, however, drawbead effects in the drawbead region are less obvious due to the lower prescribed drawbead characteristics, see Figure 4-23.

The simulated flange shape, obtained with the equivalent drawbead model, compares very well with the experimentally determined flange shapes for the rectangular products with different drawbeads. It can be concluded that the equivalent drawbead model is a powerful tool to replace the real drawbead geometry in deep drawing simulations.

4.4.3 Simulation of a fender

Finally, a simulation was carried out to demonstrate the performance of the equivalent drawbead model in the deep drawing simulation of a real automotive product. The numerical tool description is given as an exploded view in Figure 4-28. The initial blank was a rectangle of 810 x 680 mm, with an initial thickness of 1.2 mm and made from aluminum. The final product depth was 118 mm. To avoid a long computational time, the blank was coarse meshed with 11016 3-node triangular elements based on membrane theory and the material behavior was assumed to be rigid plastic.

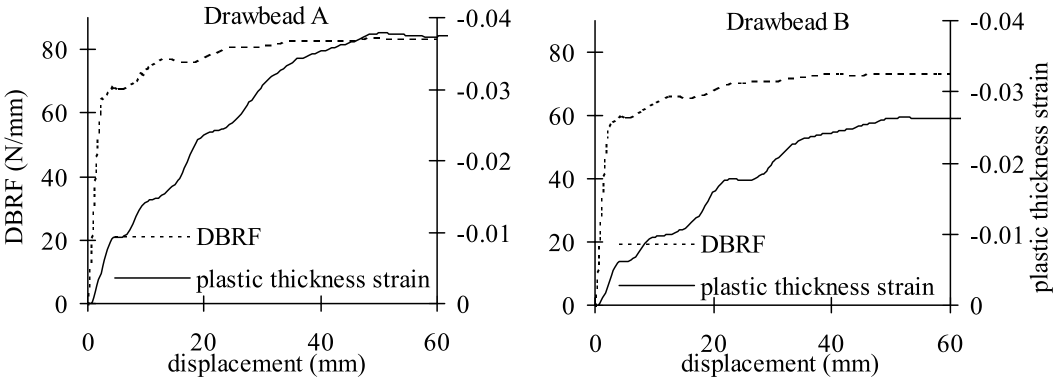

Figure 4-27. DBRF and plastic thickness strain for drawbead A and drawbead B

The tool geometry of the fender comprised three drawbeads. The geometry of the drawbeads along the long side of the product were equal, drawbead A. The geometry of the drawbead along the short side of the product differed from the other drawbeads, drawbead B.

In the simulation, the three drawbeads were replaced by an equivalent drawbead model. The drawbead characteristics of both drawbead A and drawbead B were determined with the 2D plane strain drawbead model and are given in Figure 4-27.

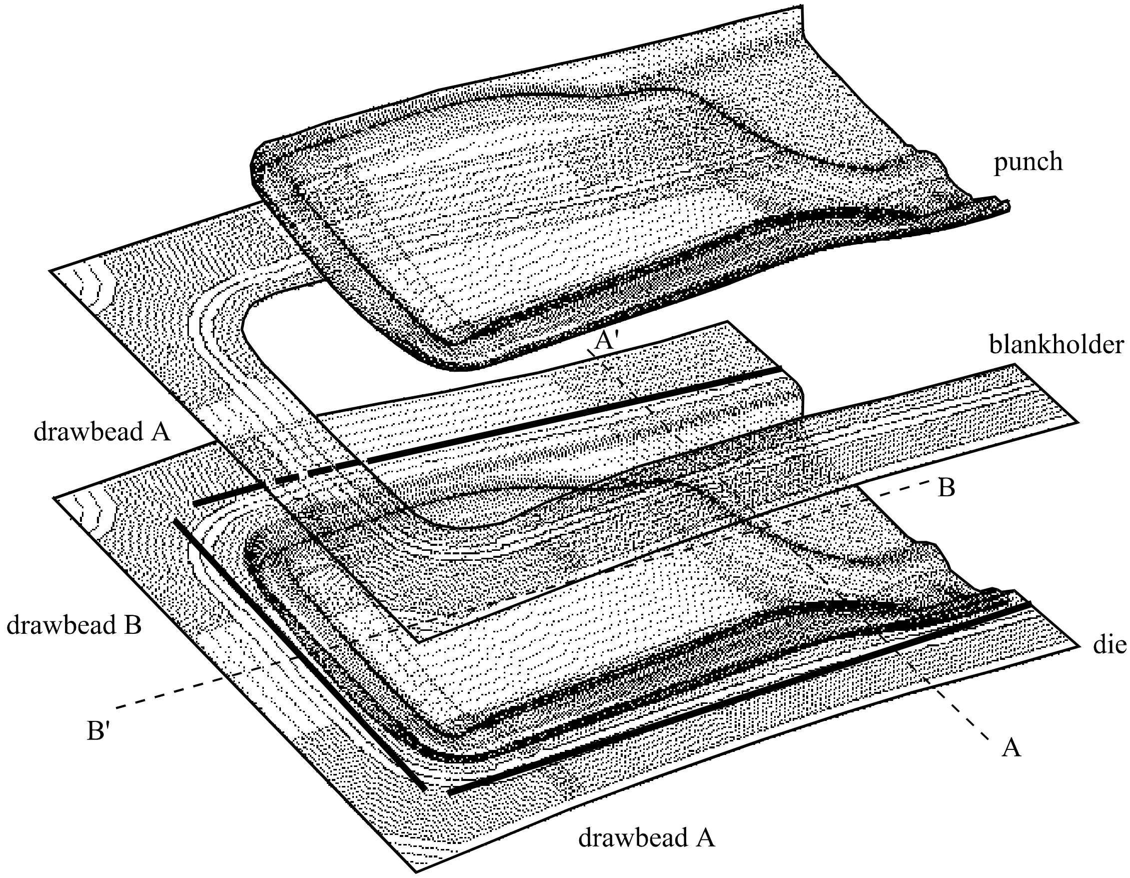

Figure 4-28. Tool description for the fender

One simulation was performed in which the equivalent drawbead model was applied and one simulation was carried out without drawbeads. First the plastic thickness strain distribution in the fender is shown along cross-section AA', see Figure 4-29, and cross-section BB', see Figure 4-30 (the definition of the cross-sections is given in Figure 4-28). These figures clearly show that the strain distribution in the entire product changes due to the applied drawbeads. Roughly, it can be concluded that the plastic thickness strain in the entire product is increased by -0.04 when the equivalent drawbead model is applied.

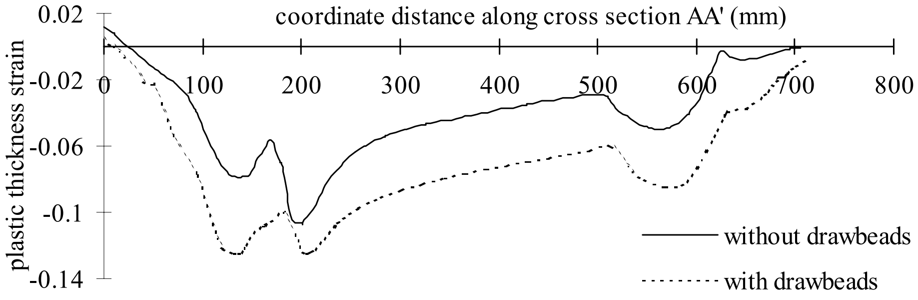

Figure 4-29. Plastic thickness strain distribution along cross-section AA'

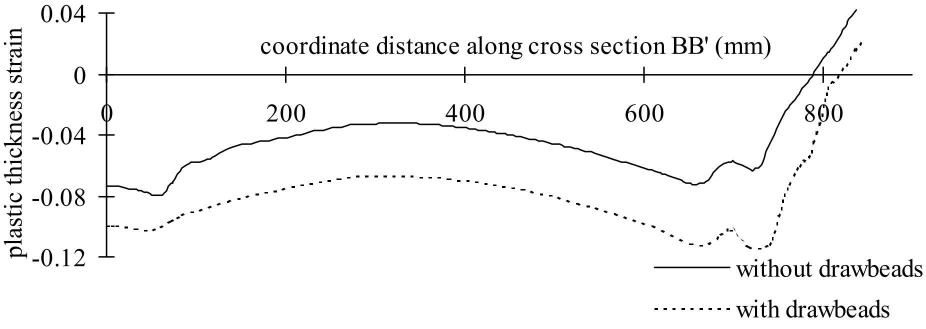

Figure 4-30. Plastic thickness strain distribution along cross-section BB’

The flange shape of the fender, determined with both simulations, is depicted in Figure 4-31. This figure shows that the draw-in of the blank is decreased when the equivalent drawbead model is applied due to the prescribed restraining force and plastic thickness strain. The material displacement through the different drawbeads is small in this product. Along the short side of the product, the material displacement through the drawbead is maximally 20 mm. Along the upper long side of the product, the material displacement through the drawbead is also maximally 20 mm and along the lower long side of the product this displacement is maximally 12 mm. Figure 4-27 shows that for these displacements, the steady state values of the DBRF and the plastic thickness strain are not reached for the two drawbeads. Therefore it is important to incorporate the DBRF and plastic thickness strain as history dependent rather than using the steady state value.

Finally, the plastic thickness strain distribution in the fender is given in Figure 4-32 for both simulations. It is concluded that the strain distribution in the entire product is significantly influenced when the equivalent drawbead model is applied.

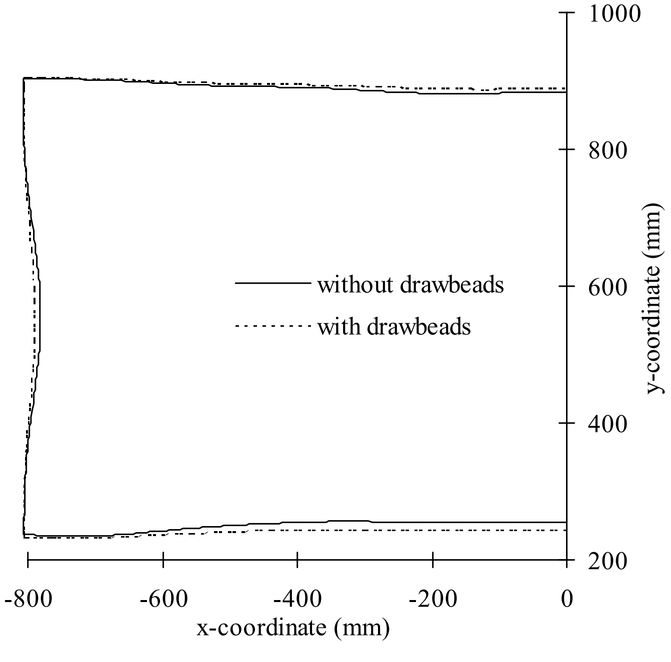

Figure 4-31. Flange shapes of the fender

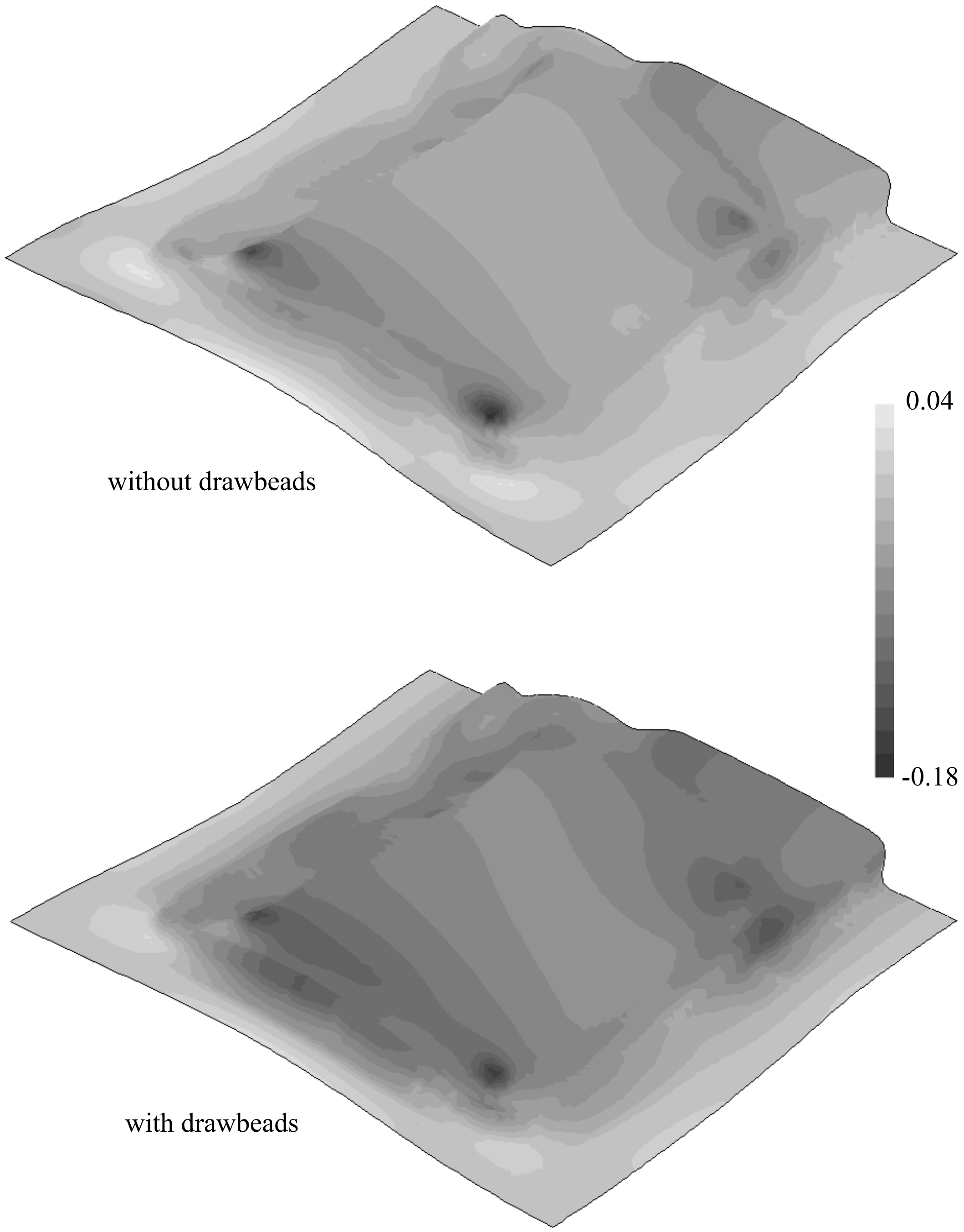

Figure 4-32. Plastic thickness strain distribution in the fender

4.5 Concluding remarks

A 2D plane strain drawbead model was developed which gives reliable predictions of the drawbead restraining force (DBRF), the lift force and the plastic thickness strain for all different drawbead geometries. The results of the 2D plane strain drawbead model serve as an input for the equivalent drawbead model. The equivalent drawbead model developed here replaces the real drawbead geometry by a line on the tool surface on which a numerical algorithm acts. This numerical algorithm incorporates the history dependent DBRF, the lift force and changes in the strain distribution. Two different strain algorithms have been developed to take the strain changes into account. The strain algorithm based on a penalty constraint method is preferred to the strain algorithm based on a stress estimate because of the better convergence behavior. Experiments were carried out to test the performance of the equivalent drawbead model. The good agreement between the experimental results and the simulation results shows that the equivalent drawbead model is a powerful tool to replace the real drawbead geometry in deep drawing simulations.

Note that the equivalent drawbead model is based on a plane strain assumption. If the drawbead is sufficiently long, the deformation pattern in the straight part of the drawbead can be assumed as plane strain. For this part of the drawbead, the real drawbead geometry can successfully be replaced by the equivalent drawbead model. However, the deformation pattern of the blank in the vicinity of the drawbead ends is fully three-dimensional and hence the plane strain assumption does not hold for these parts of the drawbead. Improper design of the drawbead ends can cause the sheet to wrinkle and this phenomenon cannot be taken into account in the equivalent drawbead model.

4.6 References

[Beugels, 1993]
Beugels J., ‘Drawbead simulaties’, Master’s Thesis, University of Twente, Enschede, 1993

[Brouwer, 1999]
Brouwer J.T., ‘Verification of drawbead models’, Master’s Thesis, University of Twente, Enschede, 1999

[Cao, 1993]
Cao J., M.C. Boyce, ‘Drawbead penetration as a control element of material flow’, SAE 930517, Sheet Metal and Stamping Symposium, Detroit, 1993

[Carleer, 1994]
Carleer B.D., P.T. Vreede, M.F.M. Louwes, J. Huétink, 1994, ‘Modelling drawbeads with finite elements and verification’, J. Mat. Proc. Tech. , vol. 45/1-4, p. 63-69, 1994

[Carleer, 1996]
Carleer B.D., T. Meinders, J. Huétink, ‘Equivalent drawbead model in finite element simulations’, Proceedings of the 3rd International Conference on Numerical Simulations of 3-D Sheet Metal Forming Processes, J.K. Lee et al. (eds.), Dearborn, Michigan, p. 25-31, 1996

[Carleer, 1997]
Carleer B.D. ‘Finite element analysis of deep drawing’, Ph.D. Thesis, University of Twente, Enschede, ISBN 90-90103589, 1997

[Drent, 1993]
Drent P., ‘Some experimental investigations on drawbeads’, Report 29625, Hoogovens Group R&D, Corporate Research Laboratory, IJmuiden, 1993

[Haug, 1991]

Haug E., E. Di Pasquale, A.G. Pickett, D. Ulrich, 'Industrial sheet metal forming simulation using explicit finite element methods', FE-simulation of 3-D Sheet Metal Forming Process in Automotive Industry, VDI Berichte 894, 1991

[Helm, 1998]
Helm P.N. van der, J. Huétink, R. Akkerman, 'Comparison of artificial dissipation and limited flux schemes in Arbitrary Langrangian Eulerian finite element formulations', Int. J. Num. Meth. Eng., vol. 41, p. 1057-1076, 1998

[Huétink, 1986]
Huétink J., 'On the simulation of thermo-mechanical forming processes', Ph.D. Thesis, University of Twente, Enschede, 1986

[Huétink, 1989]
Huétink J., P.T. Vreede, J. van der Lugt, 'The simulation of contact problems in forming processes with a mixed Euler-Lagrangian FE method' Proceedings of the 3rd International Conference on Numerical Methods in Industrial Forming Processes, E.G. Thompson et al. (eds.), Balkema, Rotterdam, p. 549-554, 1989

[Huétink, 1990]
Huétink J., P.T. Vreede, J. van der Lugt, 'Progress in mixed Eulerian-Lagrangian finite element simulation of forming processes', Int. J. Num. Meth. Eng., vol. 30, p. 1441-1457, 1990

[Kawka, 1994]
Kawka M., N. Wang, A. Makinouchi, 'Improving drawbeads and friction models in simulations of industrial sheet metal forming processes', Metal Forming Simulation in Industry, B. Kröplin and E. Luckey (eds.), 1994

[Maker, 1987]
Maker B., S.K. Samanta, G. Grab, N. Triantafyllidis, 'An analysis of drawbeads in sheet metal forming: part 2 - experimental verification', J. Eng. Mat. Tech., vol. 109, p. 164-170, 1987

[Mattiasson, 1999]
Mattiasson K., L. Bernspång, 'Drawbead modeling in sheet metal stamping simulation', Proceedings of the 4th International Conference on Numerical Simulations of 3-D Sheet Metal Forming Processes, J.C. Gelin & P. Picard (eds.), Besançon, vol. 1, p. 235-242, 1999

[Meinders, 1996]
Meinders T., 'Drawbead modeling in 3-D deep drawing processes', Master's Thesis, University of Twente, Enschede, 1996

[Meinders, 1998a]
Meinders T., B.D. Carleer, H.J.M. Geijselaers, J. Huétink, 'The implementation of an equivalent drawbead model in a finite element code for sheet metal forming', J. Mat. Proc. Tech., vol. 83, p. 234-244, 1998

[Meinders, 1998b]

Meinders T., H.J.M. Geijselaers, J. Huétink, 'Implementation of plastic thickness strain in an equivalent drawbead model based on a penalty constraint method', Proceedings of the 6th International Conference on Numerical Methods in Industrial Forming Processes, J. Huétink & F.P.T. Baaijens (eds.), Balkema, Rotterdam, p. 911-916, 1998

[Meinders, 1999]
Meinders T., H.J.M. Geijselaers, J. Huétink, 'Equivalent drawbead performance in deep drawing simulations', Proceedings of the 4th International Conference on Numerical Simulations of 3-D Sheet Metal Forming Processes, J.C. Gelin & P. Picard (eds.), Besançon, vol. 1, p. 243-248, 1999

[Pelgrim, 1997]
Pelgrim M.T.H., 'Implementation and validation of drawbeads in finite elements', Master's Thesis, University of Twente, Enschede, 1997

[Stoker, 1999]
Stoker H.C., 'Developments of the Arbitrary Lagrangian Eulerian Method in non-linear solid mechanics', Ph.D. Thesis, University of Twente, Enschede, ISBN 90-36512646, 1999

[Stoughton, 1988]
Stoughton T.B., 'Model of drawbead forces in sheet metal forming', Proceedings of the 15th Biennial Congres of IDDRG, Dearborn, Michigan, p. 205-215, 1988

[Taylor, 1993]
Taylor L.M., J. Cao, A.P. Karafillis, M.C. Boyce, 'Numerical methods in sheet metal forming', Proceedings of the 2nd International Conference on Numerical Simulations of 3-D Sheet Metal Forming Processes, A. Makinouchi et al. (eds.), Isehara, 1993

[Triantafyllidis, 1986]
Triantafyllidis N., B. Maker, S.K. Samanta, 'An analysis of drawbeads in sheet metal forming: part 1 - problem formulation', J. Eng. Mat. Tech., vol. 108, p. 321-327, 1986

[Vreede, 1992]
Vreede P.T., 'A finite element method for simulations of 3-dimensional sheet metal forming', Ph.D. Thesis, University of Twente, Enschede, ISBN 90-90047549, 1992

[Wisselink, 2000]
Wisselink H.H., 'Analysis of guillotining and slitting: finite element simulations', Ph.D. Thesis, University of Twente, Enschede, ISBN 90-36513995, 2000

[Wouters, 1994]
Wouters P., G. Montfort, J. Defourny, 'Numerical simulation and experimental evaluation of the modifications of material properties in a drawbead', Recent Developments in Sheet Metal Forming Technology, M.J.M. Barata Marques (ed.), Lisbon, p. 389-401, 1994

[Xu, 1997]
Xu S.G., M.L. Bohn, K.J. Weinmann, 'Drawbeads in sheet metal stamping - A review', SAE 970986, Sheet Metal Stamping Symposium, Detroit, 1997

5. Adaptive remeshing

5.1 Introduction

Zienkiewicz published his book entitled ‘The finite element method in structures and continuum mechanics’ in 1967. This book was the first to deal with the finite element method [Zienkiewicz, 1991]. At that time the power of a computer was considerably less than that available nowadays. Hence, the finite element computations had to be simple to obtain solutions in a reasonable time. From the late sixties onwards, the development of computer technology has increased drastically. Due to this increase in calculation capacity, finite element programs were developed to make more complex computations. Slowly the type of computation changed from academic test problems to practical problems. It became possible to use the finite element method for simulating complex production processes.

Today, industries such as the automotive and aerospace industry require the solution of highly complex problems concerning three-dimensional geometries, non-linear material behavior, contact conditions and large deformations. Consequently, the numerical simulation of these types of problems is potentially very expensive, even when simplifying assumptions such as membrane kinematics are made. Despite the high computer power available, it is desired that a computation can be performed overnight. Hence, the computational costs (computation time, time to prepare the initial element mesh and the amount of data to store) must be minimized while still maintaining the desired accuracy. This goal can be achieved by adaptive remeshing; the initial finite element mesh can be changed in a specific way during the simulation. Adaptive remeshing has two major advantages. First, the computational costs can be reduced by starting the simulation with a relatively coarse mesh. Remeshing at specific parts in the mesh can take place when these coarse elements are no longer able to accurately describe the geometry or the steep gradients in state variables, and this is usually the case in the final stage of the forming process. Second, when large deformations develop, the initial mesh can be highly distorted, so that the numerical simulation becomes unstable or crashes. To prevent a high mesh distortion, adaptive remeshing can be applied to enhance the element mesh during simulation.

Globally, the adaptive remeshing procedure can be divided into three phases. First, some measure of the accuracy of the solution is required. This so-called error estimator will be used to define a remeshing criterion (Section 5.2). Next, a new mesh must be generated which must satisfy specific requirements (Section 5.3). Finally, a procedure for the transfer of state variables and boundary conditions from the old mesh to the new mesh is required (Section 5.4). The performance of the adaptive remeshing procedure is demonstrated on the basis of several deep drawing simulations (Section 5.5). A preliminary study on the coupling of a wrinkling prediction model to the adaptive remeshing procedure is treated in Section 5.6.

5.2 Remeshing criterion

Remeshing must be performed when a specified error is exceeded. Huerta proposed two different approaches that can be used for assessing the error of the given mesh: error estimators and error indicators [Huerta, 1998]. Error estimators are based on optimality theory and are computationally expensive. Most error estimators are well defined for linear problems but not, however, for non-linear problems. Error indicators instead are based on heuristic considerations, i.e. an existing quantity is chosen as an indicator.

In the in-house finite element code DiekA two error indicators have been implemented. The first error indicator is based on the thickness error, the second error indicator is based on a geometrical error. These two estimators will be discussed briefly, for a detailed description the reader is referred to [Selman, 1999a].

5.2.1 Error indicator based on thickness error

First an area weighted nodal averaging technique is used to determine the smooth thickness $\bar{t}_n$ at a given node:

$$\bar{t}_n = \frac{1}{\sum\limits_{e=1}^{elemc} A_e} \sum_{e=1}^{elemc} \left(\sum_{gp=1}^{ngaus} A_e w_{gp} L_{gp} t_{gp} \right) \tag{5-215}$$

where A_e is the area of the element, *elemc* is the number of elements connected to node *n*, *ngaus* is the number of gauss integration points per element, w_{gp} is the weight function and t_{gp} the thickness at a gauss integration point. The function L_{gp} extrapolates integration point data to the nodes. The smooth thickness at a gauss point is calculated via the Gauss interpolation function N_n:

$$\bar{t}_{gp} = \sum_{n=1}^{nnode} N_n \bar{t}_n \tag{5-216}$$

with *nnode* the number of nodes per element. Finally, the relative thickness error per element Π_e^t is calculated, using the actual integration point thickness and the smooth thickness:

$$\Pi_e^t = \frac{1}{A_e} \int_{A_e} \left| \frac{\bar{t}_{gp} - t_{gp}}{t_{gp}} \right| dA_e = \frac{1}{A_e} \int_{A_e} \left| \frac{\bar{t}_{gp} - t_{gp}}{t_{gp}} \right| J d\xi d\eta = \sum_{gp=1}^{ngaus} \left| \frac{\bar{t}_{gp} - t_{gp}}{t_{gp}} \right| w_{gp} \tag{5-217}$$

where ξ and η are the natural coordinates and J is the Jacobian. An element needs to be refined when this thickness error exceeds a user-defined thickness error.

5.2.2 Error indicator based on geometrical error

For each element an orthogonal coordinate reference system is determined that is unique and node number independent, represented by the covariant base vectors g_i [Batoz, 1992]. For linear triangular elements this tangent set of axes is constant within the element. The variation of these tangent sets from one element to its neighboring elements indicates a variation of the geometry which cannot be represented by facet elements. Therefore, a nodal averaging technique is used to quantify the variation of the tangent sets of axes, see equation (5-218). In general, the smooth nodal base vectors are not orthogonal because of the applied averaging technique.

$$\bar{\boldsymbol{g}}_{i(n)} = \frac{1}{\sum\limits_{e=1}^{elemc} A_e} \sum_{e=1}^{elemc} A_e \boldsymbol{g}_i \tag{5-218}$$

where $\bar{\boldsymbol{g}}_{i(n)}$ are the smooth nodal base vectors, A_e the area of the element and *elemc* the number of elements connected to node *n*. The smooth metric tensor contains information concerning the lengths and the angles between the base vectors and is determined by the inner product of the base vectors, equation (5-219):

$$\bar{g}_{ij(n)} = \bar{\boldsymbol{g}}_{i(n)} \cdot \bar{\boldsymbol{g}}_{j(n)} \tag{5-219}$$

The smooth metric tensor per element is an average of the nodal smooth metric tensor at the nodes belonging to that element (*nnode*), equation (5-220):

$$\bar{g}_{ij} = \sum_{n=1}^{nnode} \frac{\bar{g}_{ij(n)}}{nnode} \tag{5-220}$$

Given the metric tensor within an element corresponding to the actual mesh, g_{ij}, and the smooth metric tensor corresponding to a higher order surface, Bonet [Bonet, 1994] uses a Green-Lagrange like tensor $\underline{S}$ to define the geometrical error, equation (5-221). Here only the base vectors in the plane of the surface are taken into account since the third direction is defined as the normal of both in-plane vectors.

$$S_{ij} = \tfrac{1}{2}\left(\bar{g}_{ij} - g_{ij}\right) \qquad i,j = 1,2 \tag{5-221}$$

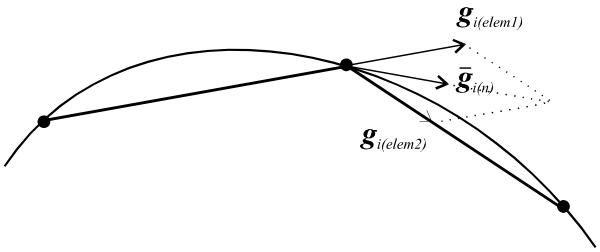

Figure 5-1. Construction of smooth nodal base vector

Note that the tensor $\underline{S}$ is not equal to the Green-Lagrange tensor $\underline{E}$, which can be explained with the help of Figure 5-1. The Green Lagrange tensor $\underline{E}$ should estimate the strain tensor between the faceted geometry, defined by the elements, and the approximated smooth geometry, defined by the smooth nodal base vectors. In the situation as sketched in Figure 5-1, stretching appears and thus the tensor $\underline{E}$ must have a positive value. However, due to the averaging technique that is used to determine the smooth nodal base vector, the length of this smooth vector will be smaller than the vectors from which it is created, yielding a negative value for equation (5-221).

The contravariant components of $\underline{S}$ must be determined since the smooth nodal base vectors are not orthogonal due to the applied averaging technique:

$$S^{ij} = g^{ik} g^{jl} S_{kl} \tag{5-222}$$

Since the third base vector is defined as the normal of the two in-plane base vectors, the deformation in the third direction can be treated as one-dimensional [Jongschaap, 1994]:

$$S_{33} = \tfrac{1}{2}\left(\bar{g}_{33} - g_{33}\right) = \tfrac{1}{2}\left(\bar{\boldsymbol{g}}_3 \cdot \bar{\boldsymbol{g}}_3 - \boldsymbol{g}_3 \cdot \boldsymbol{g}_3\right) = \tfrac{1}{2}\left(\left(\frac{\bar{t}}{t}\right)^2 - 1\right) \tag{5-223}$$

where t is the thickness and $\bar{t}$ the smooth thickness. Considering volume conservation:

$$t\sqrt{g} = \bar{t}\sqrt{\bar{g}} \tag{5-224}$$

where g and $\bar{g}$ are the determinants of the metric tensor and the smooth metric tensor.
The deformation in the normal direction is obtained as follows:

$$S_{33} = \tfrac{1}{2}\left(\frac{g}{\bar{g}} - 1\right) \tag{5-225}$$

The corresponding co- and contravariant components S_{33} and S^{33} are equal for the case in which the normal base vector is a unit vector.

Hence, the geometrical error is defined as the second invariant $\left(\Pi_e^g\right)^2$ of $\underline{S}$:

$$\left(\Pi_e^g\right)^2 = S^{mn} S_{mn} + S^{33} S_{33} \tag{5-226}$$

An element needs to be refined when this geometrical error exceeds a user-defined geometrical error.

5.3 Mesh generation

The second phase of adaptive remeshing is the generation of a new mesh. The goal is to increase the richness of the interpolation at specific parts in the blank as defined by the remeshing criterion. Three different types of spatial discetization can be distinguished: r-adaptivity, p-adaptivity and h-adaptivity [Djokovic, 1998], [Huerta, 1998]. Strategies based on r-adaptivity consist of keeping the number of spatial grid points fixed, but allowing them to move into regions where a finer spatial discretization is needed. This type of adaptation is particularly powerful on problems where a large domain is needed to capture a time varying solution which has steep slopes over only a small fraction of that domain [Drake, 1996]. Strategies based on p-adaptivity consist of changing the degree of the interpolating polynomials in appropriate regions of the mesh. This method is preferred for (linear) smooth solutions or over subregions where the solution is smooth [Li, 1996]. Strategies based on h-adaptivity consist of adapting the number of grid points and changing the mesh connectivity. Grid points are added to areas where more accuracy is demanded (the interpolation will be enriched) and can be deleted in areas where the solution is accurate enough.

Before adaptive remeshing was applied in finite element computations of forming processes, each simulation was started with an initial mesh which had to be generated carefully. One had to estimate which part of the mesh would be located at areas with high curvatures or steep gradients of state variables. This part of the mesh then required a high density of grid points. The problem of complex mesh generation beforehand can be avoided by initially generating a uniform mesh in combination with the use of h-adaptivity during the computation. In the remainder of this section the h-adaptivity strategy, implemented in the in-house code DiekA, will be treated in detail.

5.3.1 Refinement strategy

The adaptive remeshing procedure, as described in this chapter, has been specially developed for sheet metal forming. Generally, the forming of details in a sheet metal product, which correlates with high geometric curvatures and steep gradients of state variables, takes place at the end of the production process. Consequently, starting the simulation with a sufficiently fine mesh, mesh refinement will be necessary at the final stage of the forming process to compute the solution in an accurate way. At present, derefinement techniques whereby nodes are removed as they cease to be necessary will not be considered.

Simulations of sheet metal forming are performed with 3-node triangular elements. Two different approaches can be used to apply the h-adaptivity strategy to triangular elements, see Figure 5-2.

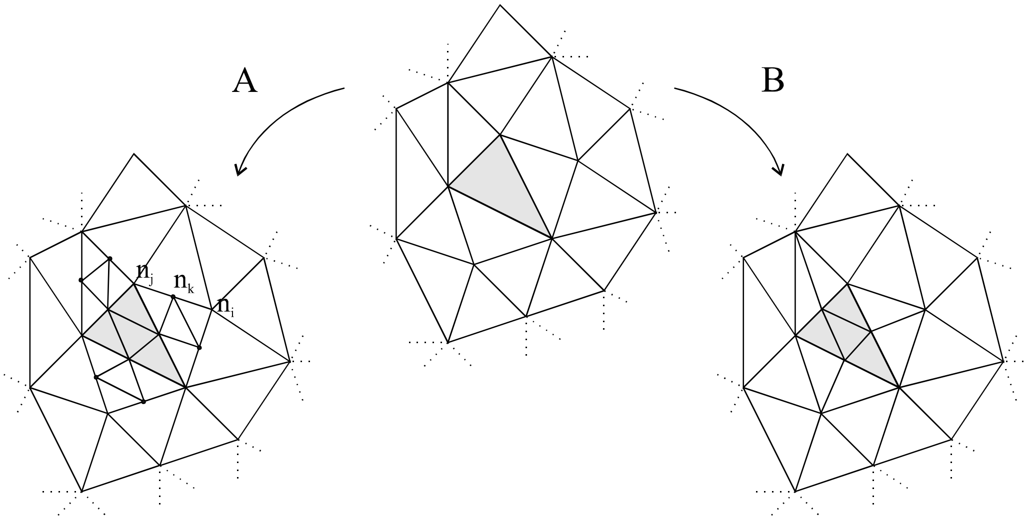

Figure 5-2. Two h-adaptivity strategies for triangular elements

In the first approach (A) the element to be refined (shaded), from now on called an inefficient element, is divided into 4 equal elements, as well as the neighboring elements of the inefficient element. The newly created nodes on the element sides of the neighboring elements, n_k, must be constrained by the old nodes of that element side, n_i and n_j, to preserve mesh compatibility. Consequently, 16 new elements and 9 new nodes are created, from which only 3 nodes contribute to new degrees of freedom, i.e. the new nodes on the element sides of the inefficient element.

In the second approach (B) the inefficient element is divided into 4 equal elements. The neighboring elements are divided into 2 elements, for reasons of conformity from now on called cleft elements. Consequently, 10 new elements and 3 new nodes are created, from which all new nodes contribute to new degrees of freedom. The advantage of this method is that the increase in richness of interpolation is reached by creating less new elements and nodes than in approach (A). A disadvantage of this method is that the aspect ratio of the neighboring elements is halved.

The h-adaptivity method which will be used is an extension of approach (B). The inefficient element has three neighboring elements, from now on called 1st order neighbor elements. Both the inefficient element and the 1st order neighbor elements are divided into 4 equal elements. Each 1st order neighbor element also has two neighboring elements, the 2nd order neighbor elements, which will be divided into 2 elements, see Figure 5-3. In this way, 28 new elements and 9 new nodes are created, from which all nodes contribute to new degrees of freedom. The advantage of this extended refinement approach is that it anticipates the further deformation process by refining both the inefficient element and the 1st order neighbor elements. In approach (B) it is most likely that when the inefficient element has to be refined in simulation step *k*, one of the 1st order neighbor elements will become an inefficient element itself at step *k+j*, and the refinement procedure must be restarted. Taking into consideration that the refinement procedure is time consuming, the extended refinement approach reduces the total time necessary for refinement in an entire simulation.

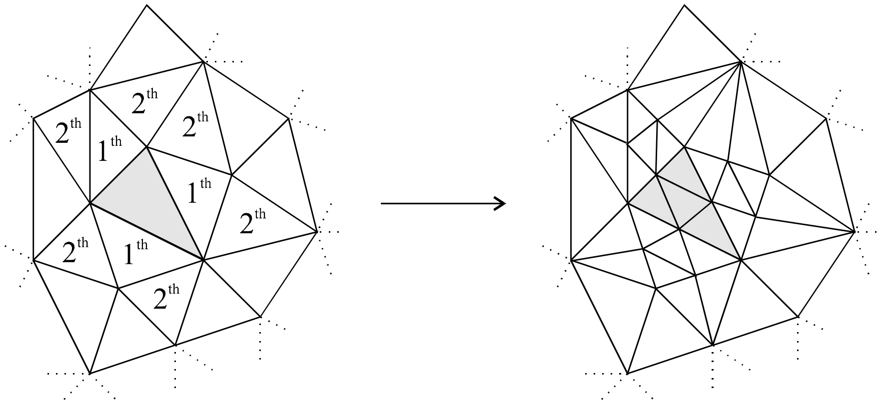

Figure 5-3. H-adaptivity method used in the in-house code DiekA

5.3.2 Degenerated cases

Application of the refinement approach in a practical problem can give rise to difficulties, and these have to be solved to maintain a consistent refinement procedure. Some test simulations were performed to overcome the possible difficulties.

2nd order neighbor surrounded by more than one 1st order neighbors

In the first test case, elements 11 and 13 are set as inefficient elements, see Figure 5-4. Elements 4, 6 and 12 are 1st order neighbor elements and 5 is the 2nd order neighbor element. Following the refinement strategy as described in Section 5.3.1, elements 11, 13, 4, 6 and 12 will each be divided into 4 equal elements. However, a difficulty occurs for element 5. Element 5 is a 2nd order neighbor which has to be divided into 2 elements. This is not allowed because there are already 2 new nodes created on the element sides of element 5 since this element is the 2nd order neighbor of two 1st order neighbor elements. Therefore it is proposed that in situations where a 2nd order neighbor element is surrounded by more than one 1st order neighbor element, this 2nd order neighbor is also divided into 4 equal elements.

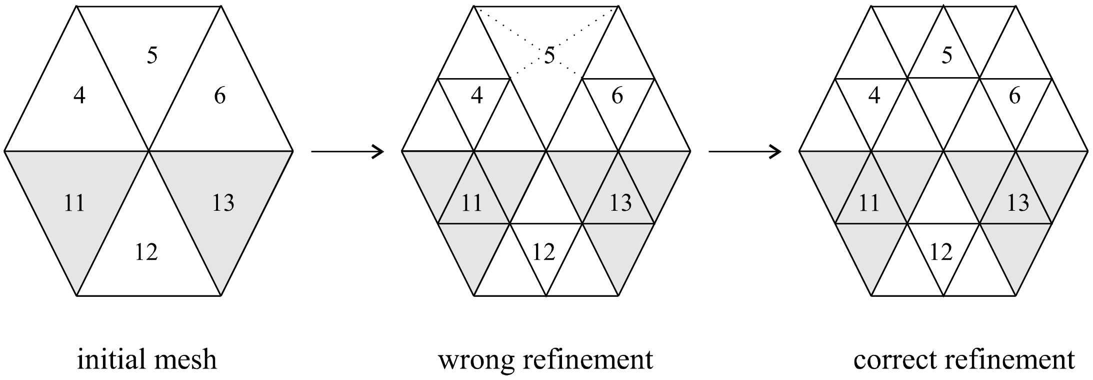

Figure 5-4. 2^{nd} order neighbor element surrounded by two 1^{st} order neighbor elements

Refinement of cleft elements

In the second test case element 1 is refined first, resulting in the element mesh given in Figure 5-5a. After refinement, each element is labeled with a value that denotes the number of refinements: the refine-level. Cleft elements keep the refine-level of the element from which they originate. In other words, elements 2, 3, 4, 9, 10, 11 and 24 have a refine-level of 0, elements 1, 21, 22 and 23 have a refine-level of 1.

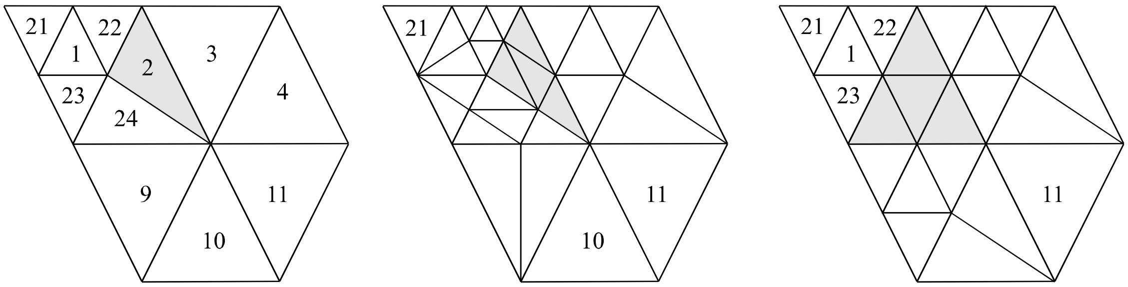

a. initial mesh b. wrong refinement c. correct refinement

Figure 5-5. Refinement of a cleft element

Next, element 2 is set as an inefficient element. From the previous refine phase, element 2 is labeled as a cleft element. Following the refinement strategy of Section 5.3.1, elements 3, 22 and 24 are the 1^{st} order neighbors and elements 4 and 9 are 2^{nd} order neighbors, see Figure 5-5a. The result of this refinement procedure is given in Figure 5-5b. It can be seen that in the initial mesh only elements 2 and 24 have their aspect ratio halved. In the new mesh, elements 2 and 24 are equally divided into 4 elements each, which results in 8 elements with a bad aspect ratio.

A better quality mesh can be created when the cleft elements 2 and 24 are considered as a pair. Before the refinement procedure is started, the cleft elements 2 and 24 are joined, after which for the element combination 2-24 the 1^{st} order neighbors are searched. It is checked that in order to qualify as a neighbor, an element must have the same refine-level as its neighbor, to preserve mesh compatibility. Consequently, the 1^{st} order neighbors of element combination 2-24 are elements 3 and 9, the 2^{nd} order neighbors are elements 4 and 10. Performing the refinement procedure yields a more uniform mesh with a minimum number of elements with bad aspect ratios, see Figure 5-5c.

Inefficient elements with different refine-levels

In the first phase of the adaptive remeshing, the error indicator used selects a list of inefficient elements. This list can contain elements with different refine-levels. Simultaneous refinement of the elements with a different refine-level gives rise to mesh incompatibility, see Figure 5-6. Elements 2 and 22 are the inefficient elements in this example. Mesh incompatibility occurs at the common element side of elements 2 and 22 in the initial configuration. To preserve mesh compatibility, the inefficient elements are subdivided into groups with the same refine-level. The refinement procedure will be carried out for each element group successively, starting with the group with the lowest refine-level. Consequently, in this example element 2 will be refined first, followed by the refinement of element 22, see Figure 5-6.

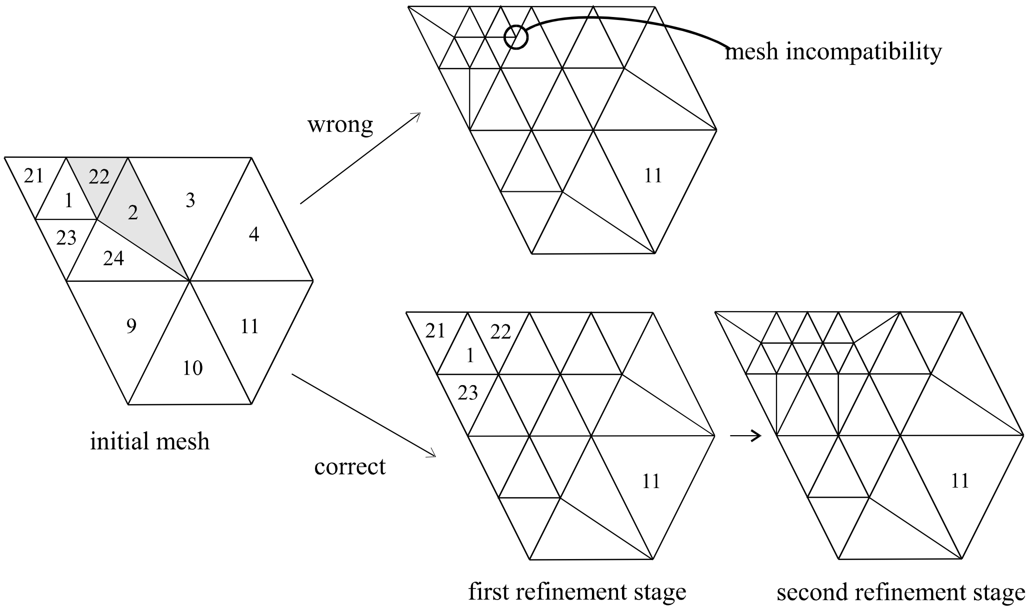

Figure 5-6. Refinement procedure for inefficient elements with different refine-levels

5.4 Data transfer

The third phase of the adaptive remeshing procedure consists of the transfer of state variables from the old mesh to the new mesh (mapping). The process of mapping is visualized in Figure 5-7. The state variables of the old elements are mapped onto the new elements through interpolation functions.

The integration point data of the old element is extrapolated to the old element nodes, equation (5-227) and Figure 5-7a:

$$f_i = L_{ij} \cdot F_j \tag{5-227}$$

where f_i are the nodal values, F_j are the integration point values and L_{ij} is a function that extrapolates the integration point data to the nodes. For a triangular element with three nodes and three integration points, L_{ij} equals the inverse of the Gauss interpolation matrix N_{ij}:

$$N_{ij} = \begin{bmatrix} \frac{4}{6} & \frac{1}{6} & \frac{1}{6} \\ \frac{1}{6} & \frac{4}{6} & \frac{1}{6} \\ \frac{1}{6} & \frac{1}{6} & \frac{4}{6} \end{bmatrix} \tag{5-228}$$

The nodal values of the new nodes are evaluated by simply averaging the nodal values of the old nodes which it is lying in-between, Figure 5-7b. One can choose to use the nodal values of the old nodes, based only on the integration point data of one element (first method), or use the average nodal value of the old nodes, based on the integration point data of all the elements connected to the old node (second method). The first method is implemented for elements with one integration point, the latter method is implemented for elements with 3 integration points. After this, the new integration point data is determined by interpolating the nodal values of the new elements to the integration points, Figure 5-7c.

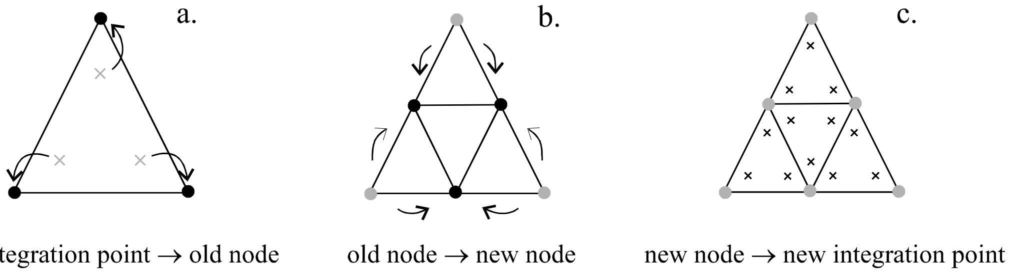

Figure 5-7. Remapping

5.5 Applications

The performance of the refinement procedure as described in the previous sections, will be demonstrated on the basis of several deep drawing simulations. In the first section a square product is simulated with triangular 3-node membrane elements with one integration point. In the second section the same square product is simulated with triangular 3-node plate elements based on Kirchhoff theory [Batoz, 1980], [Carleer, 1997]. This element contains 3 integration points in its plane and 2 to 7 integration points across the thickness. The last section describes the deep drawing simulation of an automotive product. The material behavior is assumed to be rigid plastic to avoid large computational time.

5.5.1 Square product simulation: membrane elements

In this section the refinement procedure developed above will be applied to the deep drawing of a square product, using membrane elements. The punch size is 200 mm and its stroke length is 75 mm in the negative z-direction. The punch has a shoulder radius of 10 mm and a corner radius of 20 mm. The die has the same dimension as the punch, taking into account a 1 mm offset. The initial blank size is 400 mm x 400 mm with an initial thickness of 1 mm. From a symmetrical point of view, only a quarter of the product is simulated. To demonstrate the performance of the refinement procedure an initial coarse mesh is chosen, i.e. a quarter of the blank is meshed with 800 membrane elements with an initial element size of 10 mm. Remeshing will be performed when the thickness error or the geometrical error exceeds 6%.

After 31 displacement increments of 0.5 mm in the negative z-direction, the error indicator algorithm detects elements which have a geometrical error larger than 6%, see Figure 5-8. These elements are situated at the die shoulder and the die corner. In this figure the thickness error is also shown, however, its maximum value does not yet exceed 6%. Subsequently, the elements with an error greater than 6% will be processed by the refinement procedure.

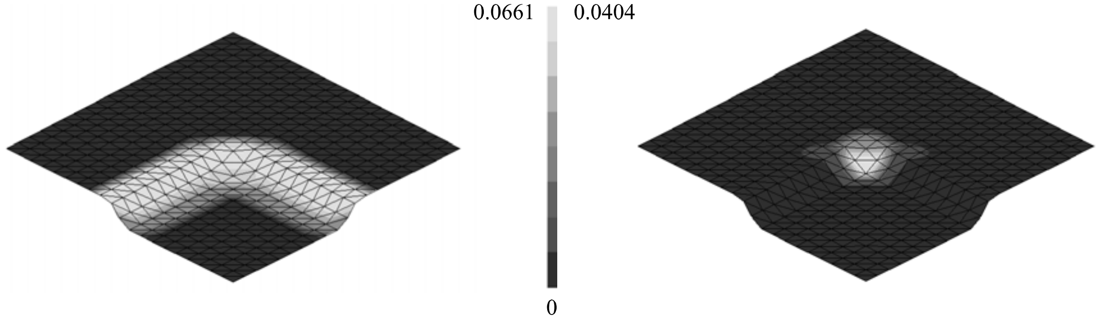

Figure 5-8. Geometrical error distribution (left) and thickness error distribution (right)

To divide an old element into new elements, the newly created nodes will be positioned exactly between two existing nodes. For an old element making contact with a radius of the tool geometry this means that the new node penetrates the tool significantly, which gives rise to unrealistic high contact pressure, see Figure 5-9. Subsequently, the contact algorithm based on a penalty method will force the node towards the tool surface in order to reduce the contact pressure.

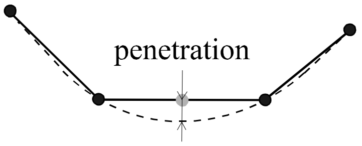

Figure 5-9. Penetration of the tool by a new node

Figure 5-10 depicts the refined mesh in step 32. Due to the refinement the sheet is able to follow the die shoulder geometry more accurately, which leads to more accurate simulation results. Again the geometrical error is shown, from which it can be seen that the error in the refined area (die shoulder and die corner) has decreased significantly to a value of approximately 0.03.

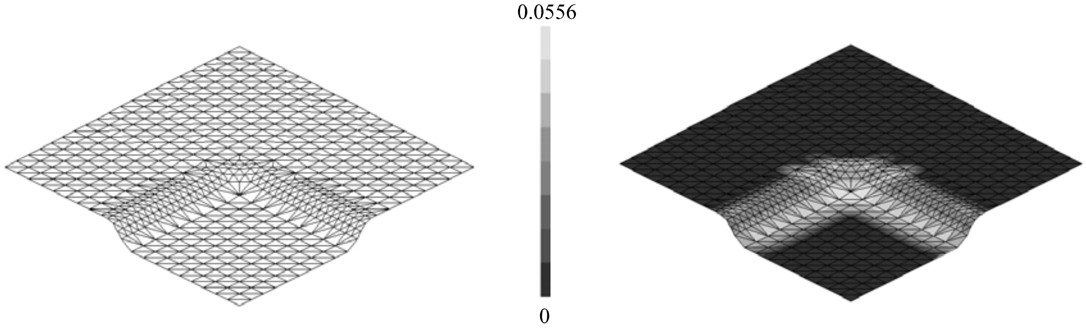

Figure 5-10. Refined mesh and geometrical error distribution in refined mesh

The final product shape is shown in Figure 5-11. The mesh contains 3342 elements, where a large number of elements is generated to describe wrinkling which appears in the die corner. Since these wrinkles do not occur in a simulation with a uniform coarse or fine mesh, they are a result of the refinement procedure. This can be explained with the help of the right-hand picture in Figure 5-11. A cleft element (containing line b) is surrounded by two refined elements (containing lines a and c). Lines a and c follow the tool geometry more accurately than line b which introduces some imperfection in the blank and subsequently spurious wrinkling may occur. To avoid this spurious wrinkling due to mesh refinement it is necessary to start the simulation with a mesh that is not too coarse.

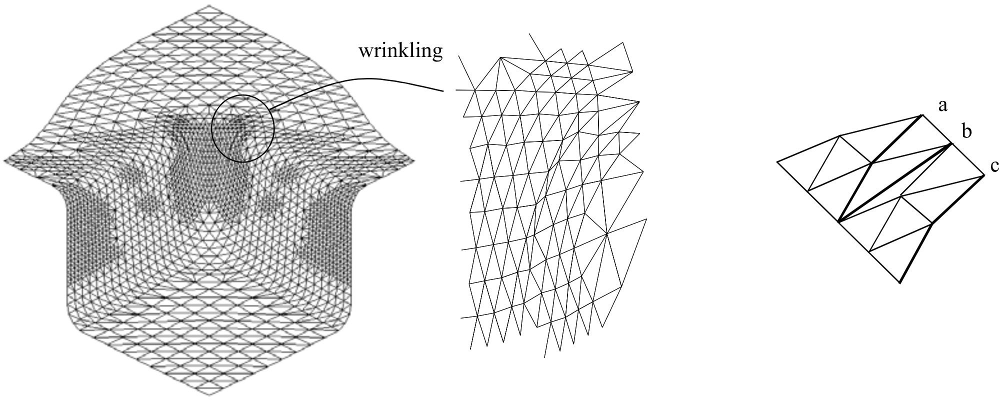

Figure 5-11. Final product shape

The high degree of refinement which is seen at both flat sides of the product can be explained with the help of Figure 5-12. When the angle α between two elements becomes too large, these elements will be refined. The refined elements flow over the tool radius until the surrounding cleft elements also reach the tool radius. Again, the angle between the already refined element and the cleft element becomes too large and the second refinement step is performed which includes a further refinement of some of the already refined elements.

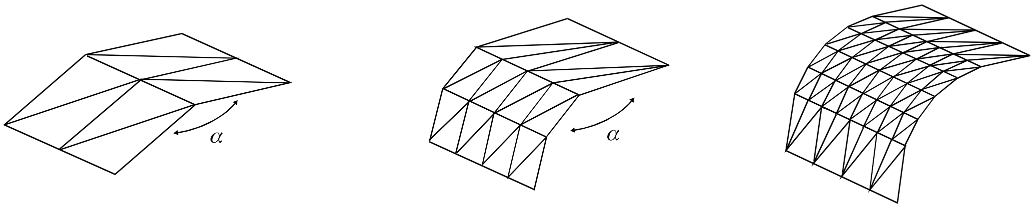

Initial mesh first refinement second refinement

Figure 5-12. Refinement in curved tool area

To finish the analysis of this simulation, the plastic thickness strain distribution of the product simulated with a refined mesh (3342 elements), a coarse mesh (800 elements) and a fine mesh (3200 elements) are compared in Figure 5-13. It can be concluded that, despite the spurious wrinkling, the simulation with the refined mesh gives a more accurate description of the plastic thickness strain than the simulation with the coarse mesh. The CPU-time for the simulation with the refined mesh was 2725 sec on a HP8000 workstation, for the simulation with the coarse mesh 720 sec, and for the fine mesh 2717 sec. The error indicator needed 0.5%, and the refinement procedure 50%, of the computation time for one iteration.

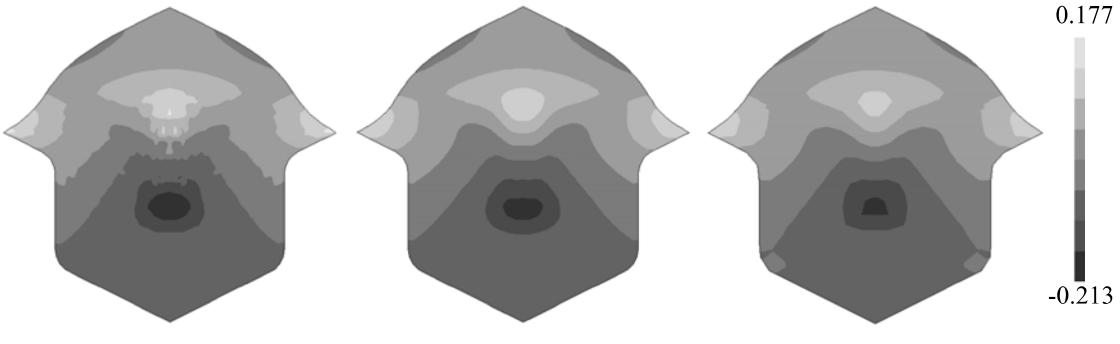

refined mesh fine mesh coarse mesh

Figure 5-13. Plastic thickness strain distribution

The refinement procedure in the former simulation was mainly controlled by the geometrical error indicator. In order to demonstrate the performance of the thickness error indicator the same simulation will be performed, but with a much higher blankholder force to introduce necking in the side wall of the product (the geometrical error is nearly zero in that part). The refined mesh and the thickness error distribution after 40 mm deep drawing are depicted in Figure 5-14. It can clearly be seen that refinement takes place in the area where necking occurs.

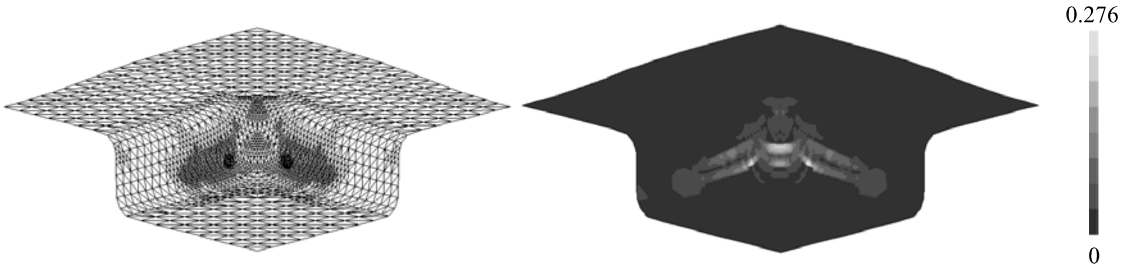

Figure 5-14. Finite element mesh and thickness error distribution

Finally the plastic thickness strain distribution in the simulation using the refined mesh is compared with the plastic thickness strain distribution in the simulation using a fine mesh (5000 elements), see Figure 5-15. The plastic thickness strain in the simulation with the refined mesh is much higher and the area where necking takes place is much smaller. Even without experimental verification it can be concluded that the simulation with the refined mesh gives a more realistic prediction of the necking process.

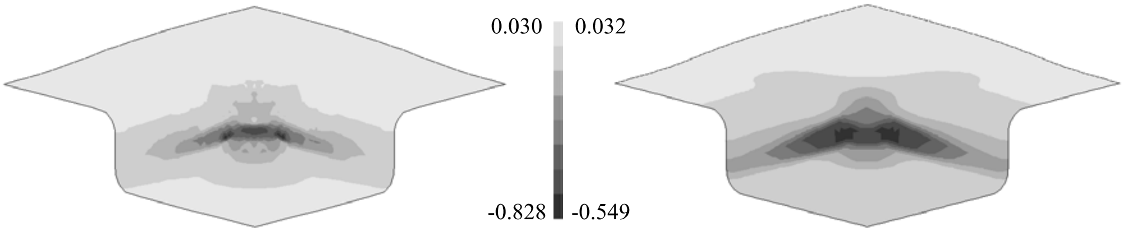

Figure 5-15. Plastic thickness strain distribution for refined mesh (left) and fine mesh (right)

5.5.2 Square product simulation: Kirchhoff elements

In this section the developed refinement procedure will be applied in the deep drawing of a square product, using plate elements based on Kirchhoff theory with 2 integration points across the thickness. The dimensions of the sheet material and the tools are identical to the square product simulation, using membrane elements. Since an initial coarse mesh can give rise to spurious wrinkling initiated by the refinement procedure (see former section), the blank is meshed with 2048 elements for this simulation. After a punch stroke of 75 mm, the plastic thickness strain of the simulation with the refined mesh is compared with the plastic thickness strain of a simulation with a fine mesh (8712 elements with an element side length of 3 mm), Figure 5-16.

The CPU-time needed for the fine mesh was 29915 sec, the refined mesh needed 10067 sec and ends up with 4038 elements. Some differences between these two simulation results can be observed. The maximum negative plastic thickness strain amounts -0.227 for the fine mesh and -0.252 for the refined mesh. The deviation between these values can be explained with the help of Figure 5-17. In this picture a part of a tool geometry (dashed line) is depicted and consists of two flat parts and a curved part. Assuming that elements a to c will be refined, then the contact algorithm will place the new nodes (gray colored) on the tool surface. This means that hardly any deformation will occur in the new elements created out of elements a and c. However, significant deformation will occur in the new elements created out of element b, which will be more than proportional. For the simulation with the initial fine mesh the deformation due to bending along the tool surface will be smoother, which explains the difference in the maximum negative plastic thickness strain.

Also, a higher negative plastic thickness strain in the side walls of the product can be observed for the simulation with the refined mesh. This is caused by the coarse elements which flow initially along the die and punch shoulder, just before these elements are refined. These parts of the blank, situated at the die and punch shoulder and meshed with these coarse elements will behave in a stiffer manner which results in more thickness strain in the side walls of the product between the die and punch shoulder.

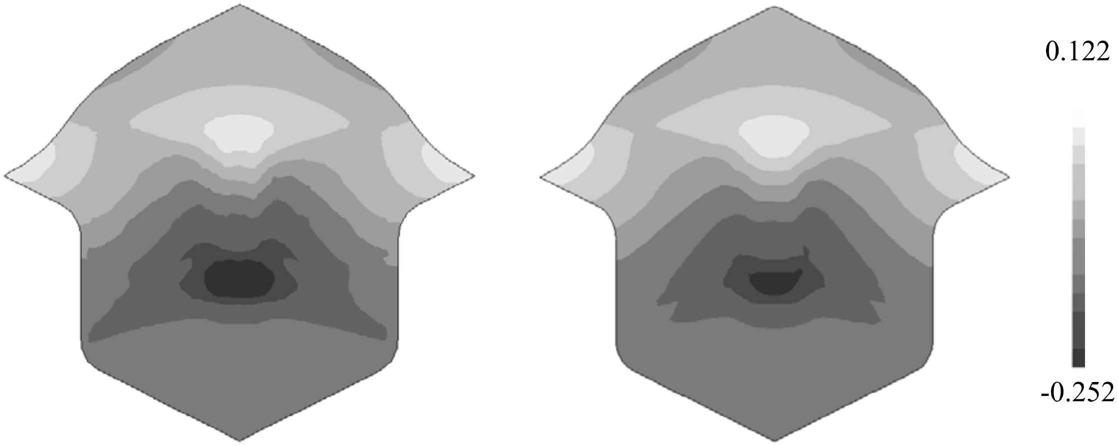

Figure 5-16. Plastic thickness strain distribution for refined mesh (left) and fine mesh (right)

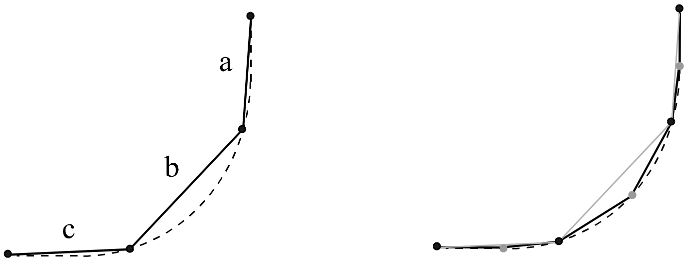

Figure 5-17. Refinement in curved tool area

Another simulation is performed with a much higher blankholder force to introduce necking in the side wall of the product, in order to show the performance of the mapping procedure used, see Section 5.4. The plastic thickness strain distribution for both the simulation with the refined mesh and the fine mesh after 85 mm deep drawing are depicted in Figure 5-18.

In contrast to the simulation results obtained with membrane elements, see Figure 5-15, the negative plastic thickness strain is lower for the simulation with the refined mesh whereas the necking area is almost identical for both simulations. The reason for the deviation in plastic thickness strain is due to the mapping procedure. The integration point data of the new elements will be determined using the average nodal value of the old nodes, based on the integration point data of all elements connected to the old node. This can give rise to data smoothing, especially when high gradients of the state variables are involved which is the case when necking occurs. The simulation with membrane elements gives a more realistic prediction of the necking process, since no smoothing is applied in the mapping procedure for membrane elements. Hence, it is recommended to use a similar mapping procedure for plate elements as for membrane elements in order to avoid smoothing.

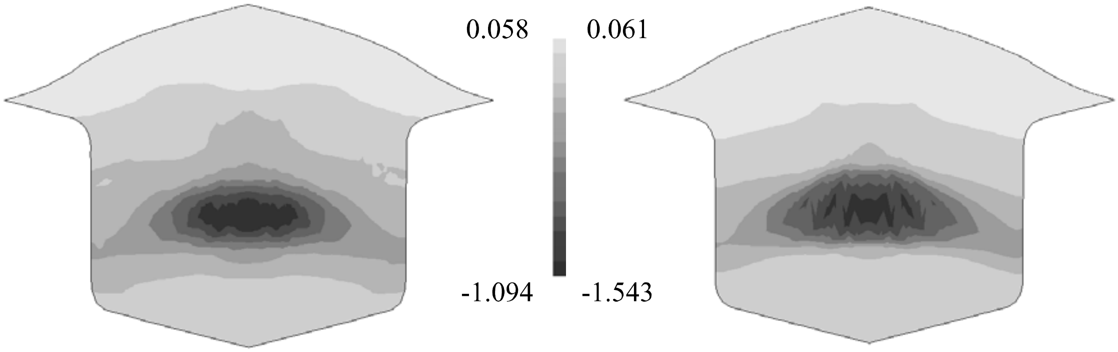

Figure 5-18. Plastic thickness strain distribution for refined mesh (left) and fine mesh (right)

5.5.3 Simulation of a fender

The final test to demonstrate the performance of the refinement procedure is the simulation of a fender. The sheet material used was a rectangle of 810 x 680 mm with an initial thickness of 1.2 mm and was made from aluminum. The sheet was coarse meshed with 11016 membrane elements. The final product depth was 118 mm. The simulation was run with and without the refinement option. The refinement procedure was restricted to one refine-level to avoid an enormous increase in the number of elements and subsequently CPU-time. The generation of new elements during the forming operation is graphically represented in Figure 5-19.

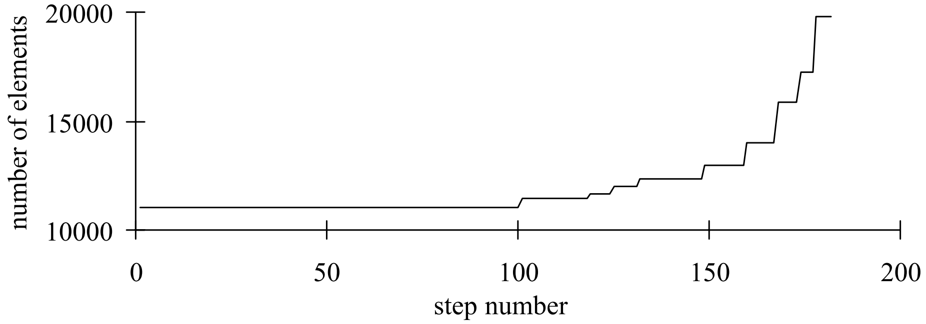

Figure 5-19. Element generation during simulation with refinement

Most of the new elements were created at the final stage of the forming process which has a positive effect on the CPU-time: the CPU-time for the simulation with refinement was 47706 sec on a HP8000 workstation. The CPU-time for the simulation without refinement was 26010 sec. When the same simulation was performed with an initially finer mesh which contained elements that were twice as small as the initially coarse mesh, the CPU-time increased by at least a factor 4. Hence it can be concluded that the refinement procedure can successfully be applied from a CPU-time point of view.

Figure 5-20 depicts the finite element meshes for computations with and without the refinement procedure. The refinement took place, as expected, at the highly curved regions in the tool description.

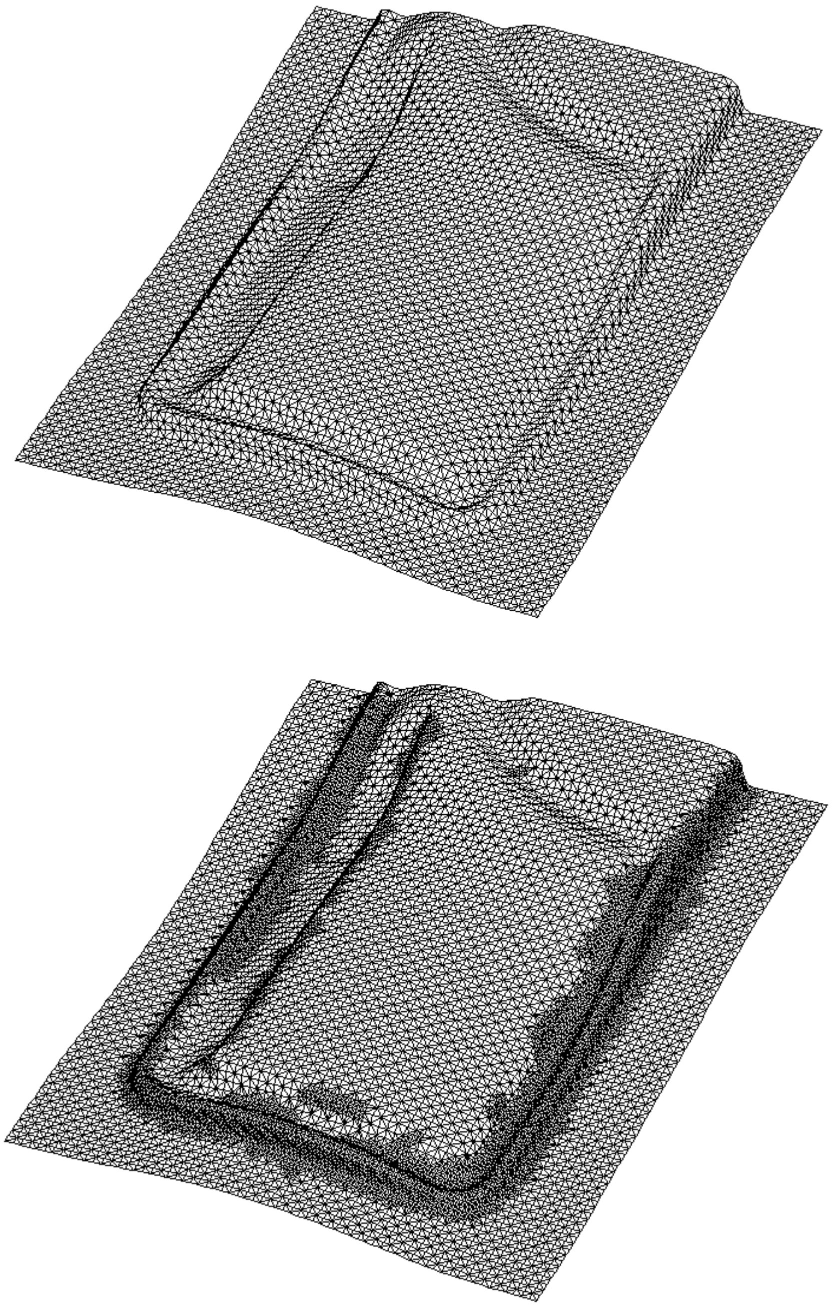

Figure 5-20. Finite element distribution for uniform mesh (upper) and refined mesh (lower)

Finally, the plastic thickness strain distribution is compared for the two simulations, see Figure 5-21. The maximum negative plastic thickness strain is higher for the refined mesh (about 4%) which was expected since the uniform mesh consists of coarse elements. Also, the overall product is more stretched when the refined mesh is used as a result of a better description of the tool geometry.

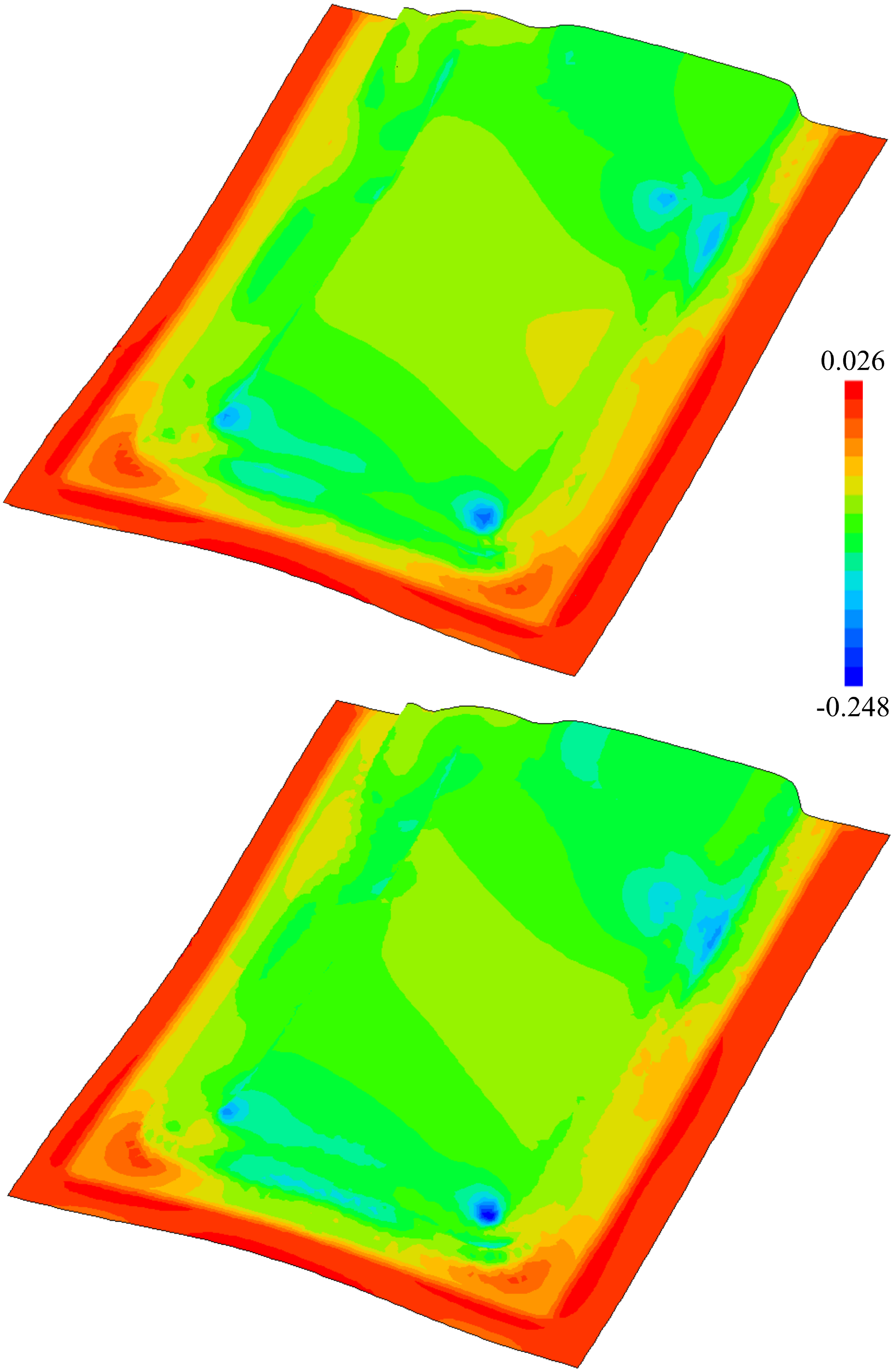

Figure 5-21. Plastic thickness strain distribution for uniform mesh (upper) and refined mesh (lower)

5.6 Prediction of wrinkling in combination with mesh refinement: a preliminary study

Surface distortions such as localized buckling and wrinkling are often observed in sheet metals during deep drawing. Because of the trend in industry towards the usage of thinner, high strength sheet materials, wrinkling is becoming one of the most troublesome failure modes in sheet metal forming. As a consequence, it is desired that a finite element simulation must be able to predict whether a sheet will wrinkle during forming or not. Generally, the dimensions of wrinkles are small compared to the dimensions of the product. As a result very small elements have to be used in a simulation to be able to spot possible wrinkling in the sheet material during forming, leading to an excessive increase of computational cost. Hence, it is desired to incorporate a predictive model for the initiation of wrinkling in a finite element code. When coupling this predictive model to a mesh refinement procedure, a simulation can be started with a relatively coarse mesh and refinement of the mesh will take place in the areas with a high wrinkling risk. In this way, wrinkles can be accurately modeled while avoiding superfluous computational cost. A model for the analysis of local wrinkling has been proposed by Hutchinson and Neale [Hutchinson, 1974], [Hutchinson, 1985]. It consists of formulating the problem within the context of plastic bifurcation theory for thin shell elements. Simplifications arise by exploiting the fact that the short wavelength modes are shallow and can be analyzed using Donnell-Mushtari-Vlasov (DMV) shallow shell theory. This theory restricts the analysis to buckling modes having a characteristic wavelength that is large compared to the sheet thickness but small compared to the local radii of curvatures.

The above mentioned analytical model is being implemented in the finite element code DiekA. For a detailed description concerning the analytical model, simplifications and implementation, the reader is referred to [Selman, 1999b], [Brunet, 1997]. Briefly, a critical wrinkling stress is calculated, which is influenced by the geometry of the sheet (local curvatures), sheet thickness, material properties and the current stress state. A wrinkling risk factor f_σ is defined, using the critical wrinkling stress σ_i^{cr} and the current principal stress σ_i:

$$f_\sigma = \left(\frac{\sigma_i}{\sigma_i^{cr}} \right) \qquad i = 1 \; or \; 2 \text{ (depending on the wrinkling direction)} \tag{5-229}$$

A wrinkling risk exists whenever the wrinkling risk factor is larger than 1. For each element, this wrinkling risk factor is calculated and as it exceeds the value of 1, the element will be processed by the refinement procedure.

The performance of the wrinkling prediction model in combination with mesh refinement was demonstrated by a deep drawing simulation of a hemispherical product. The punch had a radius of 146.5 mm, the die shoulder radius was 30 mm. The sheet thickness was 1 mm and the product depth was 100 mm. Three simulations were performed. The first simulation was performed without the refinement procedure and the blank was coarse meshed (2042 elements). The second simulation was also performed without the refinement procedure, however in this case the blank was fine meshed (8118 elements). The third simulation made use of the refinement procedure, starting with a coarse mesh (2042 elements) and ended up with a locally refined mesh (10808 elements). The deformed meshes for the three simulations after 100 mm deep drawing are given in Figure 5-22. The refined mesh clearly shows the areas where wrinkling takes place. To visualize the appearance of wrinkles in the three simulations, the curvatures in the direction of the principal axes are presented in Figure 5-23 and Figure 5-24. The simulation with the coarse mesh hardly shows any wrinkles whereas the simulation with the fine and refined meshes shows significant wrinkling in and below the die shoulder area. Note that the gray-colored areas in the pictures indicate a curvature higher than 0.1.

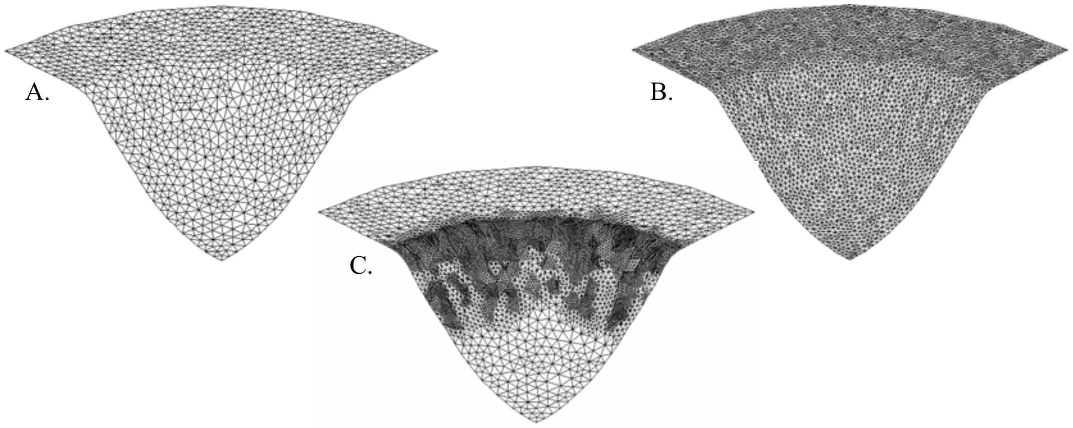

Figure 5-22. Deformed meshes (A: coarse ; B: fine ; C: refined)

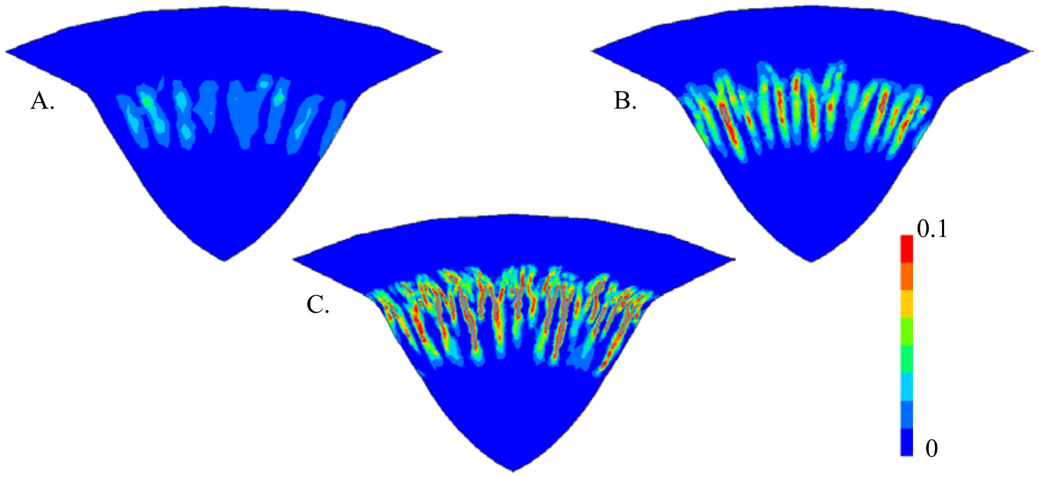

Figure 5-23. Curvature in the first principal direction (A: coarse mesh ; B: fine mesh ; C: refined mesh)

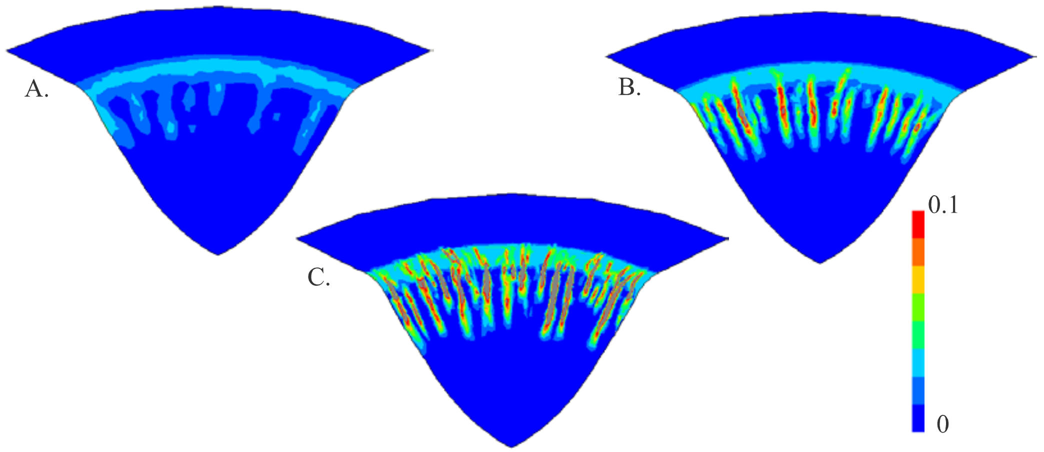

Figure 5-24. Curvature in the second principal direction (A: coarse mesh ; B: fine mesh ; C: refined mesh)

Finally, Figure 5-25 shows the wrinkling risk factor after 40 mm deep drawing for the simulation in which the refinement procedure was used. An element is processed by the refinement procedure when the wrinkling risk factor is higher than 1. This figure clearly shows the risk of wrinkling in and below the die shoulder area. Figure 5-26 shows the wrinkling risk factor in the final product for the three simulations. The figure shows that the simulations with the coarse and refined mesh still show a high potential for wrinkling, from which it can be concluded that the mesh is still too coarse to describe the wrinkling behavior accurately. The simulation with the refined mesh shows a much lower potential for wrinkling, which indicates a more accurate description of the wrinkling behavior (note that the wrinkling risk factor decreases when wrinkles actually occur due to the relaxation of the stress state and change in curvature). Since for this example the refinement procedure was restricted to 2 refine-levels, it still shows some slight potential for wrinkling.

From this preliminary study, it can be concluded that the coupling of the wrinkling prediction model to the refinement procedure can be very powerful to accurately describe the wrinkling behavior, thereby avoiding a uniform mesh with very small elements all over the product and thus also superfluous computational costs.

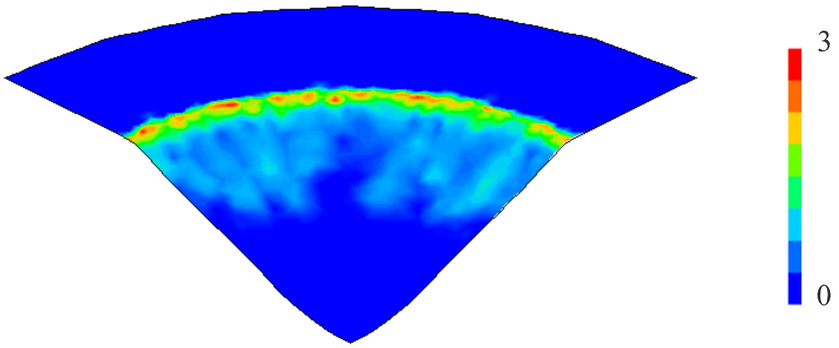

Figure 5-25. Wrinkling risk factor in simulation with mesh refinement after 40 mm deep drawing

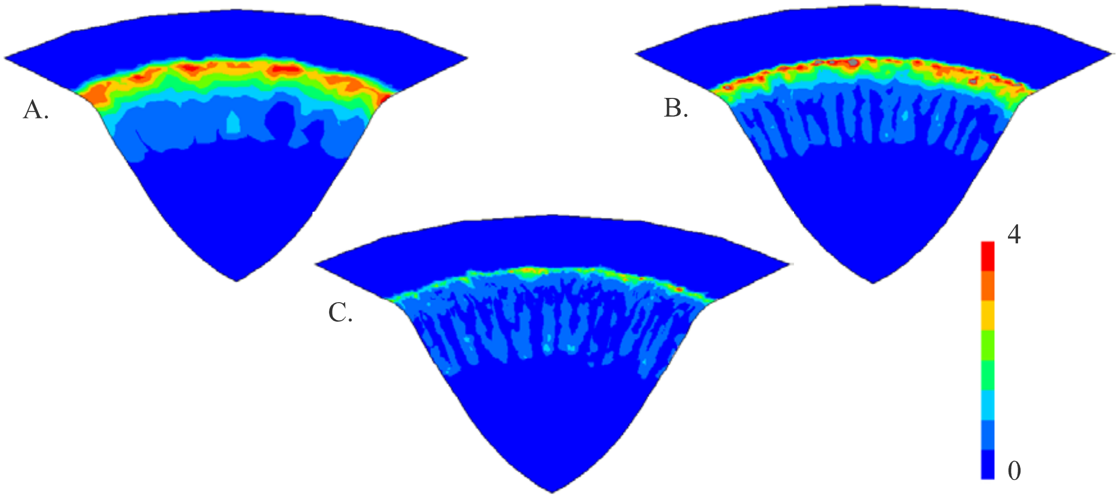

Figure 5-26. Wrinkling risk factor in the final product (A: coarse mesh ; B: fine mesh ; C: refined mesh)

5.7 Concluding remarks

A refinement procedure as implemented in the in-house finite element code DiekA is described in this chapter. Refinement of an element is performed when a user-defined error is exceeded. This error is calculated with two error indicators, an error indicator based on the thickness error and an error indicator based on a geometrical error. The performance of these indicators is demonstrated with three deep drawing applications.

The mesh generation procedure itself is of the h-adaptivity type. A new node is placed exactly between two old nodes of an element which is to be refined, i.e. an inefficient element. As the new node belongs to an inefficient element making contact with a tool radius, significant penetration of this node into the tool geometry will occur which gives rise to unrealistically high contact pressure. A contact algorithm based on a penalty method will then force the new node to the tool surface to reduce this contact pressure. In Section 5.5.2 it is shown that this approach can give rise to an overestimate of the strain state. An option to avoid this overestimate is to place the new node directly on the tool surface, using a closest point projection. Applying this option however has the disadvantage that material is generated, i.e. the total element length of the newly created elements will be greater than the original element without additional straining of the new elements.

Two data map strategies are discussed in Section 5.4. The first one makes use of nodal values which are based on the data of one element, the second one uses nodal values which are based on all the elements connected to that node. The square product simulations with plate elements based on Kirchhoff theory proved that the latter strategy can give rise to significant smoothing, affecting the credibility of the simulation results.

The refinement procedure can successfully be applied in simulations of the deep drawing process, significantly decreasing the required CPU-time for an accurate simulation. However, it is highly recommended not to start a simulation with a too coarse mesh, as this can give rise to spurious wrinkling and superfluous element generation.

Finally, a preliminary study is presented in this chapter in which the refinement procedure is coupled to a wrinkling prediction model. The results of this study show that this coupling can be a powerful tool to simulate wrinkling behavior during the forming process without an excessive increase in computational time.

5.8 References

[Batoz, 1980]
Batoz J.L., K.J. Bathe, L.W. Ho, ‘A study of three-node triangular plate bending elements’, Int. J. Num. Meth. Eng., vol. 15, p. 1771-1812, 1980

[Batoz, 1992]
Batoz J.L., G. Dhatt, ‘Modélisation des structures par éléments finis’, Hermès, Paris, ISBN 2-866013042, 1992

[Bonet, 1994]
Bonet J., ‘Error estimators and enrichment procedures for the finite element analysis of thin sheet metal forming processes’, Int. J. Num. Meth. Eng., vol. 37, p. 1573-1591, 1994

[Brunet, 1997]
Brunet S., J.L. Batoz, S. Bouabdallah, ‘Sur l’evaluation des risques de plissement locale de pieces indistrielles obtenues par emboutissage’, Actes du 3^{ieme} Colloque National en Calcul des Structures, Giens, p. 753-758, 1997

[Carleer, 1997]

Carleer B.D., 'Finite element analysis of deep drawing', Ph.D. Thesis, University of Twente, Enschede, ISBN 90-90103589, 1997

[Djokovic, 1998]
Djokovic D., 'Splines for approximating solutions of partial differential equations', Ph.D. Thesis, University of Twente, Enschede, ISBN 90-36510511, 1998

[Drake, 1996]
Drake R., V.S. Manoranjan, 'A method of dynamic mesh adaptation', Int. J. Num. Meth. Eng., vol. 39, p. 939-949, 1996

[Huerta, 1998]
Huerta A., P. Díez, A. Rodriguez-Ferran, 'Adaptivity and error estimation', Proceedings of the 6th International Conference on Numerical Methods in Industrial Forming Processes, J. Huétink & F.P.T. Baaijens (eds.), Balkema, Rotterdam, p. 63-74, 1998

[Hutchinson, 1974]
Hutchinson J.W., 'Plastic buckling', Adv. Appl. Mech., vol. 14, p. 67-144, 1974

[Hutchinson, 1985]
Hutchinson J.W., K.W. Neale, 'Wrinkling of curved thin sheet metal', Plastic Instability, J. Salencon (ed.), Press Ponts et Chaussees, p.71-78, 1985

[Jongschaap, 1994]
Jongschaap R.J.J., 'Toegepaste tensorrekening', Lecture notes, University of Twente, Enschede, 1994

[Li, 1996]
Li Y., I. Babuška, 'A convergence analysis of a p-version finite element method for one-dimensional elastoplasticity problem with constitutive laws based on the gauge function method', J. Num. Anal., vol. 33, no. 2, p. 809-842, 1996

[Selman, 1999a]
Selman A., 'Error estimation for thin sheet metal forming processes', Report WB.99/NIMR-0154, University of Twente, Enschede, 1999

[Selman, 1999b]
Selman A., 'Notes on wrinkling prediction procedure in thin sheet forming processes with adaptive mesh refinement', Internal report, University of Twente, Enschede, 1999

[Zienkiewicz, 1991]
Zienkiewicz O.C., R.L. Taylor, 'The finite element method', 4th edition, McGraw-Hill Book Company (UK), 1991

6. Conclusions and recommendations

The finite element method is used worldwide to simulate the deep drawing process. However, one of the limitations of a finite element simulation is still the high computational time for complex deep drawing parts. The objective of this work is to decrease the computational time while maintaining the robustness and accuracy. This thesis presents the development of a mixed elastoplastic / rigid plastic material model, an equivalent drawbead model and an adaptive remeshing procedure for sheet metal forming.

The objective of the mixed elastoplastic / rigid plastic material model is to benefit from the advantages of both the elastoplastic and rigid plastic material model, i.e. accuracy and fast convergence over a large range of plastic strain increments. A stiffness tensor was derived that is consistent with the applied stress update algorithm. When applying the consistent stiffness tensor, the mixed material model shows quadratic convergence in academic problems. However, in a deep drawing simulation, the mixed material model yields a non-converging process due to appearance of 3-dimensional deformation patterns. Therefore, instead of the consistent approach, the direct approach of the mixed material model is used in deep drawing simulations. The direct approach of the mixed material model behaves more robustly than the elastoplastic material model but it needs more iterations per step to converge. As a consequence, a simulation with large incremental steps using the mixed material model will be as fast as a simulation with smaller incremental steps using the elastoplastic material model.

Since a simulation becomes more accurate at smaller incremental steps, generally it is recommended to use the elastoplastic material model instead of the mixed material model. Only for critical product simulations which can be run overnight, is the mixed material model to be favored to increase the chance of a converging simulation.

The developed mixed material model did not satisfy the expectations. However, the objective to develop a fast and accurate anisotropic material algorithm, based on the improvements found for the isotropic Von Mises material model, is still interesting and research is this field is recommended.

A mechanism to control the material flow locally is provided by drawbeads. An equivalent drawbead model was developed in which the real drawbead geometry is replaced by a line on the tool surface. A discrete material element passing this line will experience a time dependent drawbead restraining force (DBRF) and a time dependent thickness strain. Simultaneously, a drawbead lift force is subtracted from the total blankholder force. The DBRF is implemented in the equivalent drawbead model as an extra body force. Two different algorithms have been developed to take into account the plastic thickness strain. One algorithm is based on a stress estimate and one algorithm is based on a penalty constraint method. The strain algorithm based on the penalty constraint method is preferred to the algorithm based on the stress estimate because of its better convergence behavior. Experiments were performed to validate the simulation results. The good agreement between the experimental data and the simulation results shows that the equivalent drawbead model is a powerful tool to replace the real drawbead in deep drawing simulations without significant loss of accuracy.

The equivalent drawbead model is based on a plane strain assumption and as a result it is not able to take into account the complex deformation behavior of the material in the vicinity of the drawbead ends. When the deformation patterns at the drawbead ends become important, it is necessary to model the real drawbead geometry instead of using the equivalent drawbead model.

The objective of adaptive remeshing is to decrease the computational time while maintaining the desired accuracy. The adaptive remeshing procedure can be divided into three phases. First, a remeshing criterion is defined based on an error indicator. Two error indicators are presented in this thesis, i.e. an error indicator based on a thickness error and an error indicator based on a geometrical error. Next, a new mesh has to be generated which must satisfy specific requirements. A refinement strategy based on h-adaptivity is developed for 3-node triangular plate elements. Finally, a procedure for the transfer of state variables and boundary conditions from the old mesh to the new mesh is required. Two transfer procedures are implemented. The first procedure uses the nodal values of the old nodes, based on the integration point data of one element. The second procedure uses the averaged nodal values of the old nodes, based on the integration point data of the all the elements connected to the old node. It is recommended to use the first data transfer procedure since the latter transfer procedure leads to inadmissible smoothing. The refinement strategy can lead to an overestimate of the strain or to spurious material generation. Besides, it can lead to spurious wrinkling and superfluous element generation when the refinement strategy is not carefully applied. When correctly used, the adaptive remeshing procedure can successfully be applied to simulations of the real-life deep drawing process, reducing the required computational time for an accurate simulation significantly.

A preliminary study was carried out of the coupling of a wrinkling prediction model to the adaptive remeshing procedure. The results of this study show that this coupling can be a very powerful tool for accurately describing wrinkling behavior, while avoiding an excessive increase in computational cost.

The performance of the refinement procedure strongly depends on the user-defined admissible error. It is recommended to investigate the influence of the admissible error on the overestimate of the strain and generation of spurious wrinkling, spurious material and superfluous elements.

List of symbols

Scalars

A	area
B	width
C	Nadai parameter
E	elasticity modulus
f	function to be convected, hardening parameter
f_σ	wrinkling risk factor
F	force
F, G, H, L, M, N	anisotropy parameters
g	determinant of the metric tensor
G	shear modulus
h	hardening modulus
H	height
J	Jacobian
l	length
L	extrapolation function
M	moment
n	hardening exponent
N	interpolation function
R	anisotropy parameter, radius
s	length, coordinate distance
S	surface
t	time, thickness
T	end time
v	relative velocity
V	volume
w	projected element side length on drawbead line, weight function
W	work
β	scalar
ε	true strain
ϕ	yield function
γ	scalar
η, ξ	natural coordinates
κ	equivalent plastic strain, parameter in finite volume scheme
λ	constant of Lamé
$\dot{\lambda}$	plastic multiplier

μ	friction coefficient
ν	Poisson’s ratio
π^t	thickness error
π^g	geometric error
θ	angle, arbitrary scalar
$\mathrm{\theta}$	arbitrary scalar
ρ	mass density
σ	true stress
ξ	scalar which depends on the anisotropy parameters
ψ	scalar

Vectors

$\boldsymbol{b}$	base vector
$\boldsymbol{e}$	base vector
$\boldsymbol{f}, \boldsymbol{F}$	force vector
$\boldsymbol{fc}$	force vector related to the penalty constraint method
$\boldsymbol{g}$	arbitrary vector, base vector
$\boldsymbol{n}$	normal vector
$\boldsymbol{P}$	force vector
$\boldsymbol{r}, \boldsymbol{R}$	residual force vector
$\boldsymbol{t}$	surface traction
$\boldsymbol{u}$	displacement
$\hat{\boldsymbol{u}}$	exact solution of $\boldsymbol{u}$
$\boldsymbol{v}$	velocity
$\boldsymbol{x}$	spatial position
$\boldsymbol{X}$	reference position
ξ	independent field variable

Second order tensors

$\underline{B}$	left Cauchy-Green tensor
$\underline{C}$	right Cauchy-Green tensor
$\underline{D}$	rate of deformation
$\underline{e}$	Eulerian strain tensor
$\underline{E}$	Lagrangian strain tensor
$\underline{F}$	deformation gradient
$\underline{g}$	metric tensor
$\underline{G}$	deformation tensor
$\underline{I}$	second order unit tensor
$\underline{K}$	tangent stiffness matrix
$\underline{Kc}$	stiffness matrix related to the penalty constraint method
$\underline{L}$	spatial velocity gradient
$\underline{Q}$	rotation tensor
$\underline{R}$	rotation tensor

$\underline{R}^*$	rotation tensor
$\underline{S}$	2nd Piola-Kirchhoff stress tensor, Green-Lagrange like tensor
$\underline{U}$	right stretch tensor, tensor to simplify the expression for the stress state
$\underline{V}$	left stretch tensor
$\underline{W}$	spin tensor
$\underline{\beta}$	hardening tensor
$\underline{\delta}$	Kronecker delta
$\underline{\varepsilon}$	linear strain tensor
$\underline{\sigma}$	Cauchy stress tensor
$\hat{\underline{\sigma}}_0$	mapped initial stress
$\tilde{\underline{\sigma}}_0$	mapped initial stress

Third order tensors

$\underline{\underline{\boldsymbol{B}}}$	tensor relating $\underline{D}$ to $\boldsymbol{v}$
$\underline{\underline{\boldsymbol{B}}}^t$	tensor relating $\underline{D}$ to $\boldsymbol{v}$

Fourth order tensors

$\underline{\underline{A}}$	tensor to simplify the expression for the stress state
$\underline{\underline{E}}$	elasticity tensor
$\underline{\underline{H}}$	fourth order unit tensor
$\underline{\underline{L}}^y$	material tensor related to plasticity
$\underline{\underline{P}}$	tensor containing the anisotropy parameters
$\underline{\underline{T}}$	permutation tensor
$\underline{\underline{Y}}$	yield tensor
$\underline{\underline{Z}}$	tensor to simplify the expression for the stress state
$\underline{\underline{\alpha}}$	interpolation tensor
$\underline{\underline{\psi}}$	derivative of tensor $\underline{\underline{\alpha}}$ with respect to κ

Operators

$\mathring{\underline{\alpha}}$	Jaumann time derivative of tensor $\underline{\alpha}$
$\dot{\underline{\alpha}}$	material time derivative of tensor $\underline{\alpha}$
$\underline{\alpha}^{-1}$	inverse of tensor $\underline{\alpha}$
$\underline{\alpha}^{T}$	transpose of tensor $\underline{\alpha}$
$\underline{\alpha}^{-T}$	inverse transpose of tensor $\underline{\alpha}$
$\varphi(\cdot)$	mapping function
Δ	increment
$\vec{\nabla}\cdot$	pre-gradient operator
$\cdot\bar{\nabla}$	post-gradient operator

$\bar{\cdot}$	average value

Subscripts

0	initial
0, 45, 90	angle to rolling direction
1	end of time increment
db	drawbead
$dbrf$	drawbead restraining force
e	element
ext	external
gp	Gauss point
i	counter representing an element side
i, j	covariant components
int	internal
k	concerning iteration k
n	node
pr_thick	prescribed thickness strain
ps	plane strain
ref	reference
t	concerning the mechanical boundary conditions, trial
u	concerning the kinematic boundary conditions
x, y, z	axis
y	yield

Superscripts

e	elastic
cr	critical
i, j	contravariant components
$init$	initial
n	concerning increment n, concerning iteration n
p	plastic
α	node
β	node
$*$	invariant

Abbreviations

CAD	computer aided design
DBRF	drawbead restraining force

Others

B	reference domain
S	spatial domain

List of publications

Journal publications

Huétink J., A.H. van den Boogaard, A.D. Rietman, J. Lof, T. Meinders, 'A mixed elastoplastic / rigid plastic material model', Int. J. Num. Meth. Eng., vol. 46, p. 1421-1434, 1999

Meinders T., B.D. Carleer, H.J.M. Geijselaers, J. Huétink, 'The implementation of an equivalent drawbead model in a finite element code for sheet metal forming', Int. J. Mat. Proc. Tech., vol. 83, p. 234-244, 1998

Meinders T., A.C. van den Berg, J. Huétink, 'Deep drawing simulations of tailored blanks and experimental verification', International Sheet Metal Review, Mack Brooks Publishing, vol. 1, p. 80-83, 1999

Meinders T., A.C. van den Berg, J. Huétink, 'Deep drawing simulations of tailored blanks and experimental verification', Int. J. Mat. Proc. Tech., vol. 103, p. 65-73, 2000

Conference contributions

Berg A.C. van den, T. Meinders, B. Stokman, 'Deep drawing simulation of tailored blanks', Proceedings of the 20th Biennial congress, p. 133-144, 1998

Carleer B.D., T. Meinders, J. Huétink, 'Equivalent drawbead model in finite element simulations', Proceedings of the 3rd International Conference on Numerical Simulations of 3-D Sheet Metal Forming Processes, J.K. Lee et al. (eds.), Dearborn, Michigan, p. 25-31, 1996

Carleer B.D., T. Meinders, H.H. Pijlman, J.Huétink, H.Vegter, 'A planar anisotropic yield function based on multi axial stress states in finite elements', proceedings COMPLAS'97, D.R.J. Owen et al. (eds.), vol. 1, p. 913-920, 1997

Huétink J., A.H. van den Boogaard, A.D. Rietman, J. Lof, T. Meinders, 'A mixed elastoplastic / rigid plastic material model', proceedings IACM'98, S.R. Idelsohn et al. (eds.), on CD-rom, 1998

Meinders T., B.D. Carleer, H. Vegter, J. Huétink, 'Recent development in finite element simulations of the deep drawing process', proceedings Shemet '97, H.J.J. Kals et al. (eds.), p. 385-396, 1997

Meinders T., A.C. van den Berg, J. Huétink, 'Deep drawing simulations of tailored blanks and experimental verification', proceedings Shemet'98, H.J.J. Kals et al. (eds.), p. 235-246, 1998

Meinders T., B.D. Carleer, J. Huétink, 'Simulation of the deep drawing process: a hierarchical method', proceedings ESAFORM'98, J.L. Chenot et al. (eds.), p. 187-190, 1998

Meinders T., H.J.M. Geijselaers, J. Huétink, 'Implementation of plastic thickness strain in an equivalent drawbead model based on a penalty constraint method', Proceedings of the 6th International Conference on Numerical Methods in Industrial Forming Processes, J. Huétink & F.P.T. Baaijens (eds.), Balkema, Rotterdam, p. 911-916, 1998

Meinders T., A.H. van den Boogaard, J. Huétink, 'A mixed elastoplastic / rigid plastic material model', Proceedings of the 4th International Conference on Numerical Simulations of 3-D Sheet Metal Forming Processes, J.C. Gelin & P. Picard (eds.), Besançon, vol. 1, p. 137-142, 1999

Meinders T., H.J.M. Geijselaers, J. Huétink, 'Equivalent drawbead performance in deep drawing simulations', Proceedings of the 4th International Conference on Numerical Simulations of 3-D Sheet Metal Forming Processes, J.C. Gelin & P. Picard (eds.), Besançon, vol. 1, p. 243-248, 1999

Pijlman H.H., J. Huétink, T. Meinders, B.D. Carleer, H. Vegter, 'The implementation of the Vegter yield criterion and a physically based hardening rule in finite elements', proceedings IACM'98, S.R. Idelsohn et al. (eds.), on CD-rom, 1998

Acknowledgment

Dit proefschrift is mede tot stand gekomen door de wetenschappelijke en sociale bijdrage van een aantal mensen die ik bij deze wil bedanken.

Allereerst wil ik Han Huétink bedanken voor zijn begeleiding in de afgelopen 4 jaar. Zonder jouw wetenschappelijk inzicht en enthousiasme zou ik niet in staat zijn geweest om dit proefschrift te schrijven. Maar ook wil ik je complimenteren met je sociale inbreng tijdens mijn promotieonderzoek. De manier waarop jij de DiekA-groep leidt is verre van zakelijk en afstandelijk, je profileert je veel meer als een soort 'vaderfiguur' en ik heb dit als zeer prettig ervaren. Ook wil ik je bedanken voor de grote mate van vrijheid die je mij hebt geboden om onderzoek te verrichten en voor het in de gelegenheid stellen van het deelnemen aan talrijke conferenties.

Twee mensen die een aanzienlijke bijdrage hebben geleverd aan de begeleiding van dit onderzoek zijn Bart Carleer en Ton van den Boogaard. Tijdens mijn afstudeerperiode en het eerste jaar van mijn promotieonderzoek heeft Bart mij wegwijs gemaakt in de wondere wereld van de trekrillen. De manier waarop jij mensen met een kluitje in het riet kunt sturen is werkelijk fenomenaal. In de resterende jaren van mijn promotieonderzoek heb ik veel steun gehad van Ton. Jij hebt mij menigmaal uit de brand geholpen wanneer ik weer eens een wetenschappelijke vastloper had, waarvoor mijn dank.

De samenwerking tussen Corus Group PLC. en de Universiteit Twente heeft ook voor mij zijn vruchten afgeworpen. In het bijzonder wil ik Eisso Atzema, Bart Carleer, Nico Langerak en Henk Vegter bedanken voor de zinvolle discussies en ondersteuning omtrent dit onderzoek.

Thanks to all my colleagues of the Applied Mechanics group, who created a very nice working atmosphere during the years. In particular I want to thank Ton van den Boogaard, Bart Carleer, Hermen Pijlman, Bert Rietman and Sid Selman who carefully read (parts) of my manuscript and gave valuable comments.
Hans Brouwer en Maarten Pelgrim worden bedankt voor hun bijdrage aan dit proefschrift die ze geleverd hebben tijdens het uitvoeren van hun afstudeeropdracht.
Herman van Corbach en Nico van Vliet worden bedankt voor hun steun met betrekking tot het computergebeuren. Het is maar goed dat er mensen zijn die, in tegenstelling tot mijzelf, een computer niet als een black box zien.
Annemarie Teunissen en Debbie Zimmerman worden bedankt voor al hun secretaire taken maar vooral voor de gezelligheid tijdens het koffiedrinken.
Een speciaal dankwoord gaat uit naar Bert Rietman die het 3 jaar lang heeft volgehouden om mijn kamergenoot te zijn. Ik hoop dat de vriendschap die we hebben opgebouwd tijdens en buiten het werk (conferenties, de ettelijke dart- en biljartavonden etc.) nog lang stand zal houden, ook al ben ik geen familie van je.

Speciale dank gaat uit naar Katrina Emmett voor het corrigeren van dit proefschrift met betrekking tot de Engelse taal.

Promotieonderzoek is niet uit te voeren zonder de mentale steun van familie en vrienden. Allereerst wil ik mijn ouders bedanken voor alles wat ze in hun leven hebben gedaan om mij zo gelukkig mogelijk te maken. Ik hoop dat ik ooit deze rol voor mijn eigen kinderen kan spelen als jullie dat voor mij hebben gedaan. Mijn broer en zus plus de aangetrouwde wederhelften worden bedankt voor alles wat broers en zussen nu eenmaal doen voor de jongste telg in de familie.

Mijn vrienden Remco Gadella, Ronald Hof, Frank Landman en Sascha Meijer wil ik bedanken voor al hun steun en belangstelling die jullie al jarenlang voor mij tonen. De manier waarop jullie mij gesteund hebben in goede maar vooral ook in moeilijke tijden kan als voorbeeld dienen voor anderen. Ik hoop dat ik voor jullie dezelfde rol heb kunnen en kan spelen die jullie in mijn leven gespeeld hebben.

Last but not least wil ik Dinian bedanken. Jij hebt me pas leren kennen in het vierde en drukste jaar van mijn promotieonderzoek. In plaats van gillend weg te lopen heb jij mij het afgelopen jaar enorm gesteund, ook al was het soms moeilijk wanneer ik voor de zoveelste keer in het weekend ging werken (hm hm, ja, precies). Ik zal het ruimschoots met je goedmaken, liefje!

About the author

The author was born on may 10, 1973 in Hengelo, the Netherlands. In August 1985, he started his study at the secondary school VWO, at ‘Lyceum the Grundel’, in Hengelo and graduated in June 1991. From 1988 till 1996 he worked part-time as a greengrocer at the ‘C-1000 Jan Dekker’ supermarket. From September 1991 till January 1996 he studied at the University of Twente in Enschede and earned his Master of Science degree in Mechanical Engineering. The graduation work involved the finite element modeling of drawbeads in the deep drawing process. He started his doctoral study in February 1996 at the Applied Mechanics group of the University of Twente under supervision of Prof.dr.ir. J. Huétink, and hopefully graduates in February 2000 with the manuscript in hand, concerning the research on developments in the numerical simulation of the deep drawing process.

Samenvatting

‘Ontwikkelingen in numerieke simulaties van het industriële dieptrekproces’

Het dieptrekproces wordt toegepast om produkten met soms complexe vormen en krommingen te vervaardigen uit plaatmetaal. Het proces begint met het klemmen van de buitenrand van de plaat tussen een plooihouder en een matrijs. De plooihouder dient ter voorkoming van plooivorming en om de materiaalstroom tijdens het dieptrekproces te controleren. Vervolgens wordt een stempel omlaag bewogen, waarbij de specifieke vorm van het gereedschap in de plaat wordt gedrukt. De uiteindelijke vorm van het produkt wordt bepaald door het gereedschap, de plaat zelf en procesparameters zoals plooihouderkracht en smeermiddel. Zonder uitgebreide kennis omtrent de invloed van al deze variabelen op het dieptrekproces is het bijna niet mogelijk om een produkt te vervaardigen met de gewenste vorm en eigenschappen. Een belangrijk gereedschap om de invloed van deze variabelen op het vervormingsproces te bestuderen is de eindige elementen methode. Voor een nauwkeurige simulatie van het industriële dieptrekproces is een nauwkeurige numerieke beschrijving vereist van het gereedschap, materiaalgedrag, contactgedrag en andere procesvariabelen. Echter, vandaag de dag voldoen de nauwkeurigheid en betrouwbaarheid van een numerieke simulatie nog niet aan de industriële eisen. De beperkingen in een numerieke simulatie zijn nog steeds de hoge rekentijden voor complexe dieptrekprodukten en het gebrek aan gedetailleerde kennis omtrent materiaal- en contactgedrag. Het doel van het onderzoek beschreven in dit proefschrift is toegespitst op het reduceren van de rekentijd van een eindige elementen simulatie zonder verlies van robuustheid en nauwkeurigheid. Dit proefschrift beschrijft de ontwikkeling van een gemengd elastoplastisch / starplastisch materiaalmodel, een equivalent trekrilmodel en een elementennet aanpassingsprocedure voor plaatvervorming.

Twee veel gebruikte materiaalmodellen in numerieke plaatvervormingssimulaties zijn het elastoplastisch materiaalmodel en het starplastisch materiaalmodel. Het elastoplastisch materiaalmodel heeft als voordeel dat het materiaalgedrag nauwkeurig wordt beschreven. Een nadeel van dit elastoplastisch materiaalmodel is dat het kan leiden tot numerieke instabiliteit ten gevolg van de overgang van elastisch naar plastisch gedrag. Het starplastisch materiaalmodel heeft als voordeel dat het een snel en robuust algoritme is. Nadelen van het starplastisch materiaalmodel zijn dat elastisch gedrag zoals terugvering niet beschreven kan worden en dat het model onnauwkeurig wordt in delen van de plaat waar geen plastische vervorming optreedt. Een gemengd elastoplastisch / starplastisch materiaalmodel is ontwikkeld om de voordelen van beide materiaalmodellen te combineren, te weten nauwkeurigheid en snelle convergentie voor zowel kleine als grote plastische rekincrementen. Het gemengde materiaalmodel bestaat uit twee delen. Het gemengde materiaalmodel degenereert tot het Euler Forward elastoplastisch materiaalmodel voor kleine rekincrementen. Voor grote rekincrementen degenereert het gemende materiaalmodel tot het starplastisch materiaalmodel. De prestaties van het gemengde materiaalmodel zijn getoetst aan de hand van academische problemen en een praktisch probleem. Het gemengde materiaalmodel presteert goed in het geval van de academische problemen, maar werkt niet goed in het geval van het praktische probleem.

De kwaliteit van een diepgetrokken onderdeel wordt bepaald door de materiaalstroom tijdens het dieptrekken. Deze materiaalstroom kan lokaal worden beïnvloed door trekrillen. Trekrillen zijn kleine uitstulpingen die in de plooihouder of matrijs geplaatst worden. Een trekril bestaat uit twee onderdelen, de ril zelf en een bijpassende geul. De trekril veroorzaakt een weerstandskracht ten gevolge van een cyclisch buig- en terugbuigproces wanneer materiaal door de trekril wordt getrokken, waarbij de rektoestand in het materiaal verandert. Een equivalent trekrilmodel is ontwikkeld waarbij in een dieptreksimulatie de echte geometrie van een trekril wordt vervangen door een lijn op het gereedschapsoppervlak die de belangrijkste trekrileigenschappen bevat. De invoer van het equivalente trekrilmodel wordt verschaft door experimenten of door een 2D trekrilmodel (gebaseerd op de vlakke vervormingstoestand) waarin de echte geometrie van de trekril is gemodelleerd. Experimenten zijn uitgevoerd om het equivalente trekrilmodel te valideren. De goede overeenkomst tussen de experimenten en de simulaties laat zien dat het equivalente trekrilmodel een krachtig gereedschap is om de echte trekrilgeometrie in een simulatie te vervangen zonder een aanzienlijk verlies van nauwkeurigheid.

De numerieke simulatie van industriële dieptrekprocessen is in aanleg zeer kostbaar. Daarom is het gewenst om de rekenkosten van een simulatie te minimaliseren zonder verlies van de nauwkeurigheid. Dit doel kan bereikt worden door het aanpassen van het elemententnet tijdens de simulatie. Aanpassen van een elemententnet tijdens een simulatie heeft twee voordelen. Ten eerste kan de rekentijd beperkt worden en ten tweede kan een misvormd elemententnet worden voorkomen. De aanpassing van het elemententnet wordt uitgevoerd in drie fasen. Ten eerste wordt een criterium gedefinieerd gebaseerd op een foutafschatter die bepaalt welk deel van het elemententnet aangepast moet worden. Vervolgens wordt een nieuw elemententnet geconstrueerd dat voldoet aan gestelde eisen. Tot slot moet de data worden overgezet van het oude elemententnet naar het nieuwe elemententnet. In dit proefschrift worden twee foutafschatters gepresenteerd: een foutafschatter gebaseerd op een fout in de dikteverdeling en een foutafschatter gebaseerd op een fout in de geometriebeschrijving. Een verfijningsstrategie is ontwikkeld voor 3-knoops driehoekige plaatelementen, gebaseerd op een aanpassingsstrategie van het type *h*. Twee transformatie-algoritmes zijn geïmplementeerd om de data van het oude naar het nieuwe elemententnet over te zetten. De werking van de elemententnet aanpassingsprocedure is gedemonstreerd aan de hand van een aantal dieptreksimulaties. De resultaten van deze simulaties tonen aan dat de elemententnet aanpassingsprocedure succesvol kan worden toegepast in de simulatie van industriële dieptrekprocessen, waarbij de rekentijd voor een nauwkeurige simulatie drastisch wordt verlaagd. Tevens is een prille studie uitgevoerd naar de koppeling van een model dat plooivorming kan voorspellen en de elemententnet aanpassingsprocedure. De resultaten van deze studie laten zien dat deze koppeling zeer krachtig kan zijn om nauwkeurig plooivorming te beschrijven, waarbij een overbodige toename van de rekentijd kan worden voorkomen.